Alma Mater Studiorum – Università di Bologna

Alma Mater Studiorum – Università di Bologna

DOTTORATO DI RICERCA

in Scienze Chimiche

Ciclo XXI

Settore scientifico disciplinare di afferenza: CHIM/02

PhD Dissertation

Microfluidic device and interfacial transport: application to biomolecules and nanostructures

Presented by: Dr. Pierpaolo Greco

PhD Coordinator:

Prof. Giuliano Longoni

Supervisor:

Dr. Fabio Biscarini

Esame finale anno 2009

Keywords:

Microfluidics

Soft-lithography

Nanostructures

Platinum clusters

Carbon Nanotubes

Titanium Dioxide

Amyloid

Peptide aggregation

To my wife and my family

Abstract

The aim of my dissertation is to provide new knowledge and applications of microfluidics in a variety of problems, from materials science, devices, and biomedicine, where the control on the fluido-dynamics and the local concentration of the solutions containing the relevant molecules (either materials, precursors, or biomolecules) is crucial. The control of interfacial phenomena occurring in solutions at different length scales is compelling in nanotechnology for devising new sensors, molecular electronics devices, memories.

Microfluidic devices were fabricated and integrated with organic electronics devices. The transduction involves the species in the solution which infills the transistor channel and confined by the microfluidic device. This device measures what happens on the surface, at few nanometers from the semiconductor channel.

Soft-lithography was adopted to fabricate platinum electrodes, starting from platinum carbonyl precursor. I proposed a simple method to assemble these nanostructures in periodic arrays of μ-stripes, and form conductive electrodes with characteristic dimension of 600 nm. The conductivity of these sub-microwires is compared with the values reported in literature and bulk platinum. The process is suitable for fabricating thin conductive patterns for electronic devices or electrochemical cells, where the periodicity of the conductive pattern is comparable with the diffusion length of the molecules in solution.

The ordering induced among artificial nanostructures is of particular interest in science. I show that large building blocks, like carbon nanotubes or core-shell nanoparticles, can be ordered and self-organised on a surface in patterns due to capillary forces. The effective probability of inducing order with microfluidic flow is modeled with finite element calculation on the real geometry of the microcapillaries, in soft-lithographic process.

The oligomerization of Aβ40 peptide in microconfined environment represents a new investigation of the extensively studied peptide aggregation. The added value of the approach

I devised is the precise control on the local concentration of peptides together with the possibility to mimick cellular crowding. Four populations of oligomers where distinguished, with diameters ranging from 15 to 200 nm. These aggregates could not be addresses separately in fluorescence. The statistical analysis on the atomic force microscopy images together with a model of growth reveal new insights on the kinetics of amyloidogenesis as well as allows me to identify the minimum stable nucleus size. This is an important result owing to its implications in the understanding and early diagnosis and therapy of the Alzheimer's disease.

List of publications

- Pierpaolo Greco, Santiago David Quiroga, Pablo Stoliar, Soumya Dutta, Silvia Milita, Stefano Zacchini, Maria Carmela Iapalucci, Massimiliano Cavallini and Fabio Biscarini "Conductive Sub-micrometric Wires of Platinum-Carbonyl Clusters Fabricated by Soft-Lithography " *Journal of The American Chemical Society*, **2008**; 130(4); 1177-1182.

- Cristiano Albonetti, Javier Martinez, Nuria S. Losilla, Pierpaolo Greco, Massimiliano Cavallini, Francesco Borgatti, Monica Montecchi, Luca Pasquali, Ricardo Garcia, Fabio Biscarini "Parallel Local Anodic Oxidation of Silicon Surfaces by Soft Stamps", *Nanotechnology* 19 No 43 (**2008**) 435303

- Chiara Dionigi, Pierpaolo Greco, Giampiero Ruani, Massimiliano Cavallini, Francesco Borgatti and Fabio Biscarini "3D Hierarchical Porous TiO2 Films from Colloidal Composite Fluidic Deposition", *Chemistry of Materials*, **2008**, 20 (22), pp 7130–7135

- Dana Alina Serban, Pierpaolo Greco, Sorin Melinte, Alexandru Vlad, Stefano Zacchini, Maria Carmela Iapalucci, Massimiliano Cavallini and Fabio Biscarini, "Towards all-organic field effect transistors by additive soft-lithography", *Small*, **2009**, doi: 10.1002/smll.200801732

Manuscripts

- Adina Lazar, Pierpaolo Greco, Francesco Zerbetto and Fabio Biscarini, "Smallest stable oligomer of AB-40 amyloid peptide in confined environment", in preparation

- Ilaria Tonazzini, Eva Bystrenova, Adina Lazar, Pierpaolo Greco, Annalisa Calò, Pablo Stoliar, Claudia Martini and Fabio Biscarini, "Influence o Morophology of Organic

Semiconductor thin films on the viability of human astroglial cells", in preparation

- Chiara Dionigi, Michele Bianchi, Pasquale D'Angelo, Beatrice Chelli, Pierpaolo Greco, Arian Shehu, Ilaria Tonazzini, Adina Nicoletta Lazar, Fabio Biscarini, "Control of neuronal cell adhesion on single-wall carbon nanotube 3D patterns by electrical stimulation", in preparation

Contents

Chapter 1

Introduction

The aim of my Ph.D. dissertation is to provide new knowledge and applications of microfluidic devices in a variety of problems, from materials science, devices, and biomedicine, where the control on the fluid dynamics and the local concentration of the solutions containing relevant molecules (either materials, precursors, or biomolecules) is crucial. This is a very compelling problem in nanotechnology, viz. how to control interfacial phenomena occurring in solutions at different length scales. For this reasons, my activity ranged from modeling of the microfluidic device, to its fabrication and integration into organic electronics devices.

The doctoral work has been pursued at the Nanostructures of Multifunctional Materials Lab of the Institute for Nanostructured Materials Study (ISMN), belonging to the National Research Council (CNR), under the supervision of Dr. Fabio Biscarini. The activities and the training received can be briefly summarized:

- Study and optimization of the photolithographic parameters with mask-aligner facility with training on the use of the split field microscope Suss MikroTek. Activities involving soft-lithography. Hot embossing on polymeric substrates with a hot plate Weber press.

- Cleaning procedures of silicon wafers, native oxide or thermal oxide coated. Sur-

face treatment and defined geometric patterning with silanes and processable polymers. Plasma treatment and functionalization of polydimethylsiloxane (PDMS) by chemical route. Training and measurement with contact angle to verify the effect on the surface.

- Atomic Force Microscopy (AFM) of nanostructures and image analysis, training and measurement. Contact and Tapping mode techniques to analyze platinum μ-stripes and protein aggregates. Development of the algorithm for spatial correlation analysis between grains identified in the AFM image.

- Desing and finite element calculation of the microfluidic devices, by software package Comsol Multiphysics 3.3a. Solution of the mass and momentum balance. Rapid prototyping for surface patterning, employing micro molding in capillaries stamps.

The main results of the doctoral work are detailed in single chapters. An overview of each argument is provided in the following sections.

1.1 Microfluidic device fabrication

Up to the present perspectives, microfluidics has been considered a direct outcome of miniaturization, i.e. the possibility to handle efficiently nanoliters of solution, with analytical grade. The fluidic microdevices are able to sustain rapid switching in the flowing medium, and can be merged within parallel systems to enhance the velocity of recognition reactions, for example the sequentiation of DNA, in a direct process without amplification[1] .

Besides the fluid dynamic enabling aspect, microfluidic devices have been recognized as fundamental in investigation of protein binding through interferometry[2] , in capillary electrophoresis, in protein crystallization by interface regulation[3]

Within my thesis work, I attempted to fabricate a microfluidic cell, to couple with sensing device working in field effect modulation. The transducing effect of the transistor channel

extends to the solution which occupies the volume confined by the microfluidic device. This allows to measure what happens on the surface, at few nanometers from the semiconductor channel. This integration has raised the necessity to improve the design of the microfluidic cell to align with the sensing area of the organic field effect transistor. The geometry has to vary according to each test pattern configuration. I have fabricated several microfluidic cells with characteristic dimensions (width of the microchannel) ranging from 10 μm to 200 μm actuated with external microsyringe, which can be assembled on top of organic field effect transistor. The fabrication permitted to obtain a functional device with external elastomeric sealing constraint.

1.2 Platinum electrodes fabrication

Platinum carbonyl clusters have been extensively studied as solution active catalyst, with high performance in chemistry of hydrogenation , reduction of nitrites, integration within zeolites to form materials with enhanced electron donor capacity .

Recently it has been reported that they are also quantum dots, with double emitting properties . Since the discovering of the synthesis steps, there has been interest and analysis reported on the electronic properties of the self-assembled structures in solution[4–6] and in the conductor wires obtained with bottom-up approach.

In chapter 3 of the thesis I propose a simple method to assemble these nanostructures in periodic arrays of μ-stripes, to form conductive electrodes with characteristic dimension of 600 nm. The conductivity of this solution processed sub-microwires is compared with the other results reported in literature, and with bulk platinum. The process is amenable to fabricate thin conductive patterns for electronic devices or electrochemical cells, where the submicrometric conductive pattern periodicity is comparable with the diffusion length of the redox couple.

In collaboration with CNR Nanostructured Multifunctional Materials Lab, and the University Catholique Louvain La Neuve , I obtained the fabrication of interdigitated electrodes of field effect transistor device, completely made from solution processing, by means of soft-lithografic techniques. The surface properties of the platinum contacts achievable with this technique are directly comparable with roughness and textures obtained with vacuum deposition techniques.

1.3 Alignment and ordering induced by capillary flow

The ordering induced among artificial nanostructures is of particular interest in science. This knowledge can be applied to design new materials with different new properties and processability. The possibility to obtain ordered arrays of nanotubes is specifically interesting for the electronic transport[7] or the mechanical strength they confer to the polymer blend[8,9] . The ordered arrays may be obtained with direct growth starting from template seeds, or with directional orientation induced among nanotubes already formed (gas flow[10] , Langmuir Blodgett, pulsed magnetic fields, electrospinning, alignment of lyotropic nematic suspensions

In the present work I describe the alignment of carbon nanotubes with surface tension flow. The capillaries have a characteristic sub-micrometric dimension. The alignment is gathered with control on a few number of Single Wall Carbon Nanotubes (SWCNTs) or single bundles of Multi Wall Carbon Nanotubes (MWCNTs). The effective probability of inducing order with microfluidic flow is modeled with finite element calculation on the real geometry of the capillaries. Recent literature underline the physics at the base of fiber alignment in the electrospinning process within polymer matrices, using bundles of carbon nanotubes[11] . The microfluidic simulation reported in the present thesis targets the behavior of single nanotubes surrounded by surfactant shell, with a probability density approach. The electrical properties of nanowires assemblies has been measured in the CNR NMM laboratory and assessed in

comparison with the bucky paper sheet conductivity. Aligned Carbon Nanotubes, in submicrometric periodic arrays, exhibit a conductivity of $\sim 25\mu S/cm$ and a sheet conductivity of $16\mu S$ square at 10 V.

The assembly of colloidal particles with shaped monodispersity is influenced by capillary flow and repulsion due to electrostatic forces. The second part of chapter deals with fluidic alignment of spheroidal objects.

A 3D ordered structure of PS nanospheres served as molding template for calcination of titanium oxide precursor. The inverse oxide structure has a regular hexagonal close packing, with characteristic periodicity dependent on the dimension of the nanosphere and the calcination process. Thanks to characteristic bimodal porosity, and the semiconducting properties of TiO_2, these nanocrystals can be integrated into photocatalytic systems with high efficiency of conversion. The process described, rely on specific ratio between templating nanospheres on TiO_2 precursor, exploiting the surface interaction in the colloidal system.

1.4 Amyloid aggregation study in confined environment

Alzheimer disease is one of the most diffuse amyloid-related disease affecting elderly people. The biochemical path within neuronal cells has been object of several analysis. Lately, high throughput functional genomics was used to discover a G protein receptor, acting as a modulator for $A\beta$ peptide generation within human cells and mouse AD models.[12] Models can not prescind from concentration dynamics within the brain environment[13] . The atomistic resolution by which the 3D structures form must be clearly identified, whether in the aggregate form, or in the fibril forms[14,15] , as well as size, at the nanometric level, correlates with toxicity.

The $A\beta$ peptide in oligomeric forms has been found to be generated within the intracellular environment[16] , and consequently expelled. Atomic force microscopy was employed to

characterize amyloidogenic self-assembly for different protein aggregates[17,18]

The research aims recently at the comprehension of the effect of these small oligomeric forms of $A\beta$ peptide on the impairment of cognitive functions in Alzheimer brain[19] . Recent trials on the immunization effectively point out the effect of different aggregate morphologies on the pathogenesis of Alzheimer disease. The aggregates of β peptide are toxic to neurons at the synapse level[20] , whereas the fibrils and plaques induce inflammation response and astroglyosis. It is therefore important to comprehend fully the mechanism of nuclei induced polymerization at the initial stages, in environments where molecular crowding and interfaces are similar to the real biologic tissue.

Chapter 5 reports the thesis work on the oligomerization of $A\beta 40$ peptide in microconfined environment, and characterize the evolution of four populations of oligomers, with diameters ranging from 15 to 200 nm. These aggregates could not be addresses separately in fluorescence, as exposed in current literature. This characterization by atomic force microscopy may add a tassel to kinetics of amyloidogenesis, looking at the different evolution of each population density with concentration.

Chapter 2

Microfabrication

In this chapter there is a summary of the techniques involved in the process of microfabrication will be presented. The content is examined from an experimental point of view, leaving the modeling of the geometry (i.e. analytical study, alignment induced on the surface by capillary flow) to the following chapter.

The microfabrication process shares common aspects with MEMS (micro electro mechanical systems) device production, since the scope is still oriented towards the study and control of flow dynamics at the microscopic scales.

Besides control of the volume and boundaries, which is usually the target in fluidic analytical devices, the fluidic cell must be sealed on the sensing device, therefore non conformal geometry, roughness and chemistry of the interface are important.

The following sections describe the contact mode in thick film photolithography and the fabrication of easily affordable high contrast (non binary) masks for photolithography (sect.2.1.2), and replica molding, adopted to produce the microfluidic cell. Some detail is provided on the surface modification of polydimethylsiloxane and the characteristic deformation effects which will occurr when the sensor device is coupled directly to the microfluidic cell.

In fig. 2.1we report a simple scheme to summarize the salient steps adopted for the present work

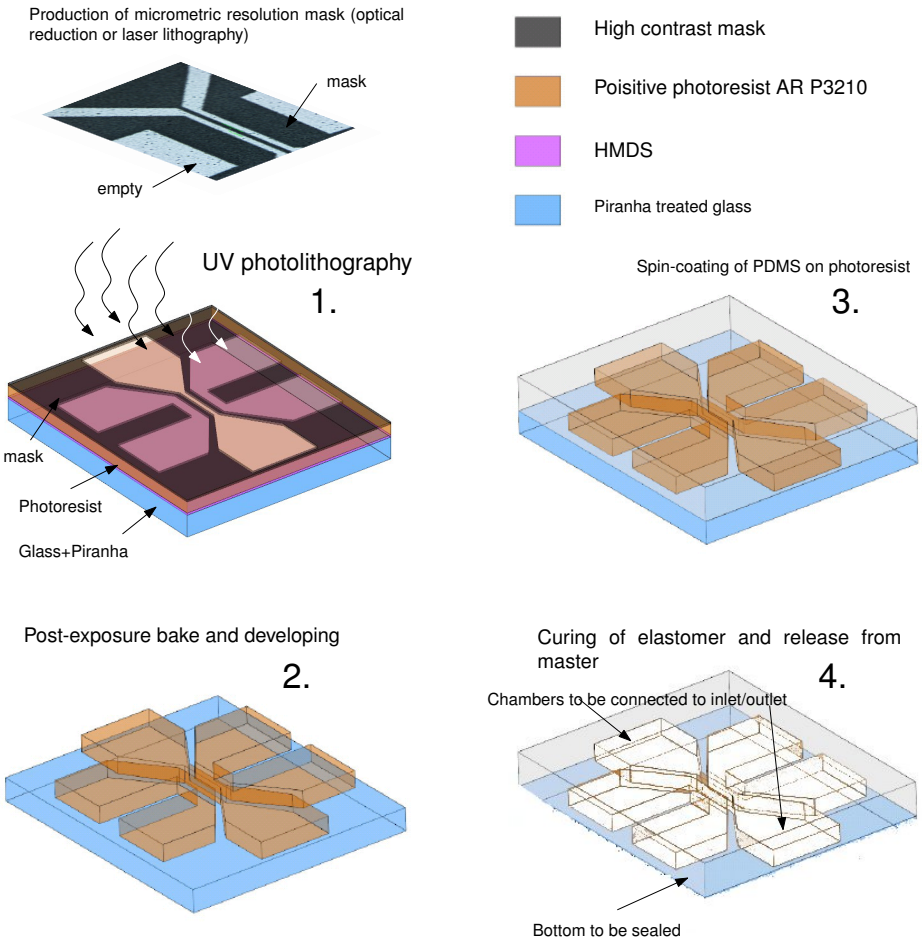

Figure 2.1: Steps in the photolithographic of a microfluidic cell made of PDMS

2.1 Photolithography

2.1.1 Mask aligner

Fig. 2.2 shows the mask aligner used for the experiment. Mask aligner is a split field optical microscope with high power UV used to expose a photosensitive film spin-coated on a sub-

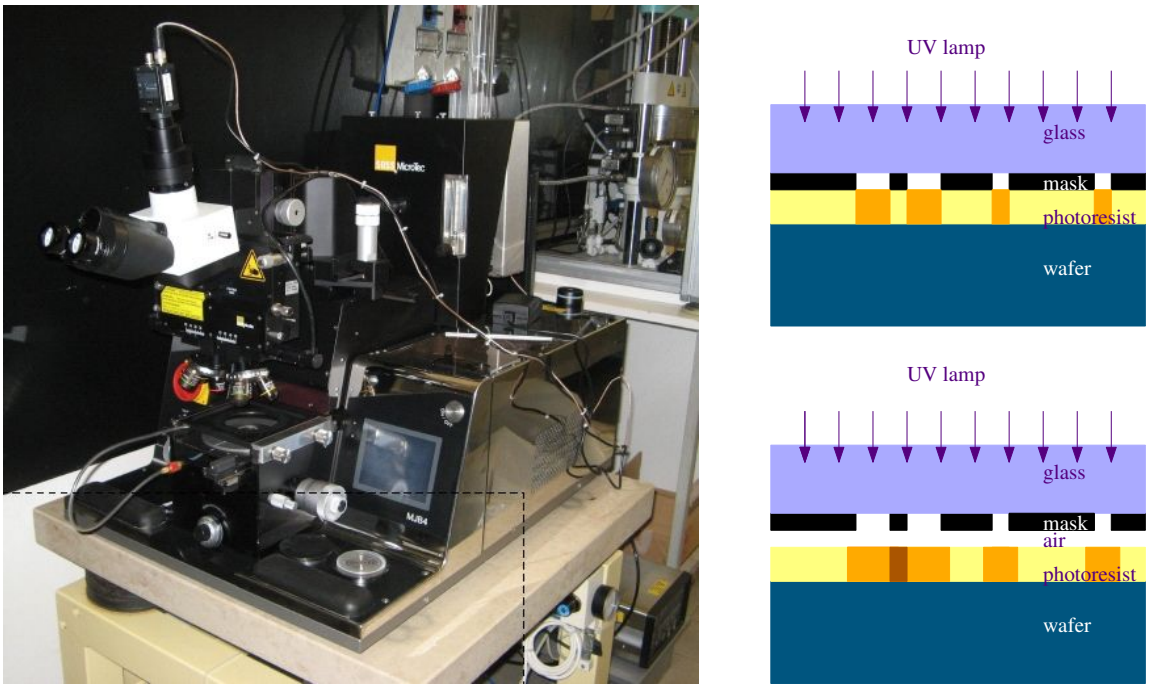

Figure 2.2: Suss Mikro-Tek Mask Aligner. Pictorial scheme of photolithography in contact (above) and in proximity (below). Contact mode guarantees the best resolution achievable for a scale 1:1 process, avoiding possible interference effects, due to the air gap present in proximity.

strate. An x, y micrometric stage allows one to align the mask with micrometric resolution. The lateral positioning can be down to 0.5 μm in accuracy.

The exposure can proceed in projection or in contact mode. In projection, the mask is held between the condenser and the objective lenses, while in contact mode the mask is brought in direct contact with the photoresist (shadow mask). With uniform exposure on the mask, several copies of the unit design can be obtained at once across a large area. The effective high throughput is the most important advantage, with respect to the step and repeat routine occurring in projection mode.

Contact mode photolithography has however some drawbacks. It does suffer from wearing during use. Some alignment systems, among which the Suss MikroTek mask aligner used here, provide the technology to move the substrate further apart from the mask (in proximity), so that it can be put on duty for longer times. Apart from proximity (or soft contact), the

mask aligner has also modes for hard contact and vacuum contact. In hard contact, the mask is fully pressed against the photoresist, so that the maximum resolution is achieved (standing the limit of 1:1 scaling allowed by contact photolithography); in vacuum contact, the gas present at the interface is removed through vacuum pumping.

The minimum feature size is determined by diffraction limit of the wavelength of the light adopted for exposure, giving the Rayleigh equation:

$$d \sim \lambda/(2NA) \tag{2.1}$$

. Experimentally the minimum feature size (w_M) can be expressed in terms of wavelength and distance between the mask and the substrate (s_c):

$$w_M = 1.4\sqrt{\lambda s_c} \tag{2.2}$$

In this expression s_c is taken to be equal to $\frac{1}{2}D$ (half of the photoresist thickness), otherwise is taken to be the proximity distance, in a range comprised between 20 μm and 200μm. For a thick photoresist layer of 10μm, this rule of thumb gives us a maximum resolution of approximately 2μm.

2.1.2 Mask fabrication

Particular attention has been put in obtaining high resolution mask with optical reduction, which improves the resolution achieved with standard ink-jet printing technology. The optically reduced mask was acquired employing high contrast and fine grained photographic film exposed through high numerical aperture objective, with exposure and developing times selected to increase the contrast of the etched film. The film grain limited the size of reproduced features to a dimension larger than 15μm.

Although highly contrasted these masks contain a certain level of gray tones, largely

Ch.	Width [μm]	(st. dev. On width) [μm]	Height [μm]	Volume [nL]
A	17.9	0.8	2.8	0.15
B	15.7	1.0	3	0.14
C	18.8	1.3	3.6	0.20
D	25.8	1.2	3.9	0.30
E	33.6	0.5	4.	0.40
F	41.7	0.8	4.2	0.53
G	45.8	1.4	4.2	0.57
H	54.5	1.2	4.3	0.70
I	63.1	2.5	4.3	0.81
L	66.8	2.2	4.3	0.86
M	70.7	2.5	4.2	0.89

Table 2.1: Experimental width, height and volume of microchannels obtained, after photolithography, on a thick film of photoresist (All Resist P3210). Immediately after spin coating, the thickness of the film was $\approx 10\mu$m

ascribed to exposure, so they need to be tested in order to ensure the functionality, as well as the best exposure time for the mask aligner. The presence of a background non completely transparent, reduces notably the minimum size of the feature repeated by the mask.

2.2 Soft lithography

Soft lithography is the principal technology to explore the self-organization of molecules at the interface. It uses polymer stamps to confine the solution. The geometry and the surface properties of the stamp (surface tension, chemical functionalization) allow to use a bottom-up approach to micro and nano lithography.[21]

Soft lithography includes different techniques (fig. 2.4). The most important are microcontact printing, micromolding in capillaries, solvent assisted micromolding, lithographically controlled wetting.

Microcontact printing uses the relief structures on the surface of a PDMS part as a stamp

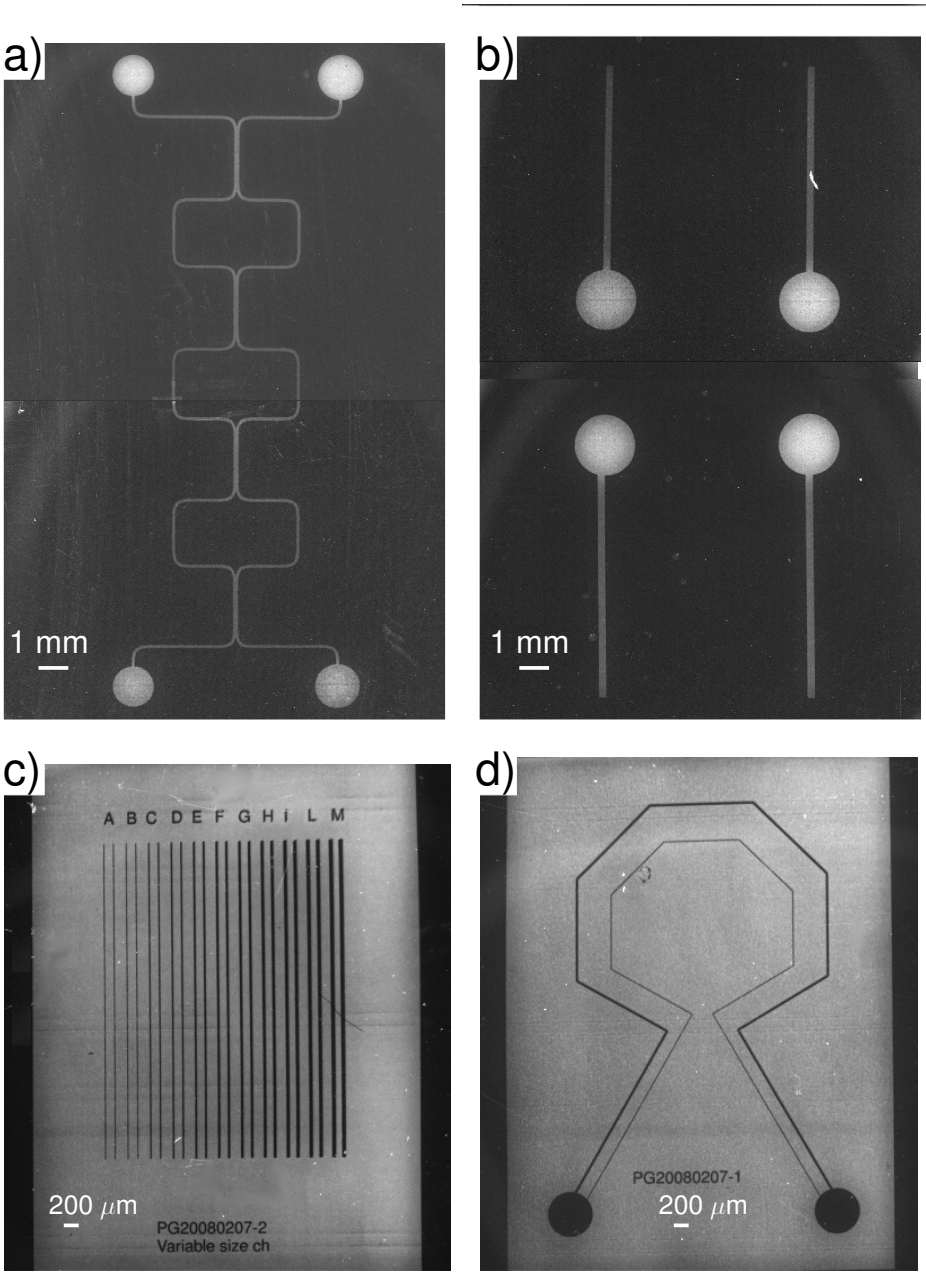

Figure 2.3: Images of masks obtained with optical reduction techniques. a) Microfluidic mixer (diffusion) on equispaced sections. 1st level mask. The resulting PDMS replica was in direct contact with the sensing device (organic field effect transistor, not shown) b) Microfluidic mixer. 2nd level mask. The PDMS replica (obtained after photolithography) will be sealed on top of the 1st level, after drilling holes in the round sections. c) Mask consist in microchannels with different width, equispaced. The PDMS replica was used in MIMIC of biomolecules. d) Microfluidic device designed to study the effect of the substrate surface orientation on the reaction assisted by the flow.

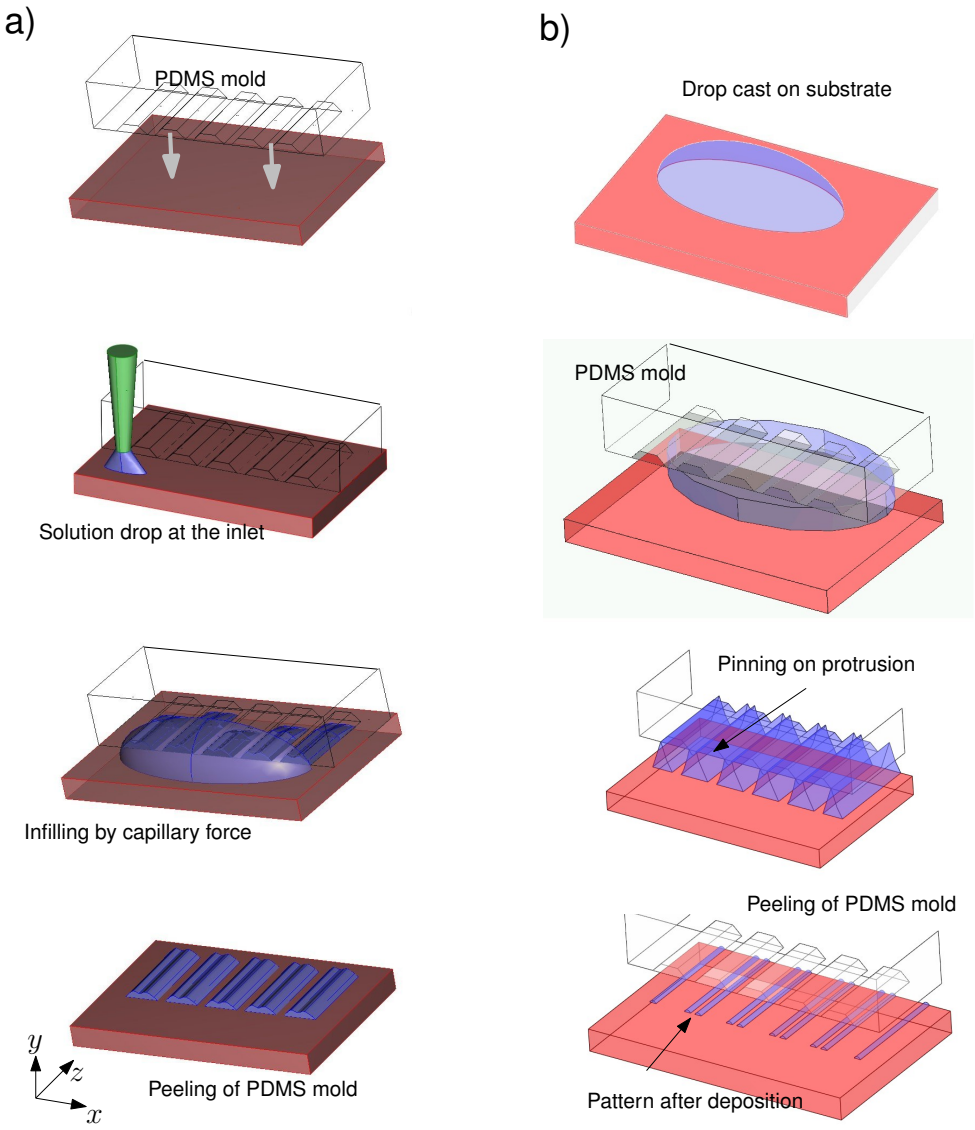

Figure 2.4: Process schemes of soft-lithographic techniques. Adapted from Xia and Whitesides (1998)[21] *(a,b,c)* and from Cavallini and Biscarini (2003)[22] *(d)*. a) Micromolding in capillaries (MIMIC); b) Solvent-assisted micromolding (SAMIM); c) Microcontact printing (MCP) d) Lithographically Controlled Wetting (LCW)

to transfer a pattern of self-assembled monolayers (SAMs) to the substrate by contact. SAMs can be created by immersion of the substrate in a solution containing a ligand with anchoring and head groups (i.e. octadecyl thiol $CH_3(CH_2)_7SH$). The head group determines the surface property of the monolayer. In microcontact printing, the stamp is wetted with the solution and pressed on the substrate surface.[21]

Micromolding in capillaries (MIMIC) uses capillary forces to fill the gaps between the substrate and the PDMS master. The PDMS is pressed against a planar substrate, sealing the walls and creating capillary channels. A drop of solution containing the desired molecules is placed at the ends of these channels and fills them automatically due to capillary forces. After evaporation of the solvent, or curing of prepolymers, the PDMS master is peeled, and the structures remain on the substrate surface.

Solvent assisted micromolding is similar to conventional embossing technique. Instead of using heat and compression, this technique uses a solvent to wet PDMS stamp and soften the structural polymer. The solvent only dissolves the structural polymer and not PDMS. The stamp is pressed on a polymer film, which dissolves in the solvent and fills the gaps between relief structures of the stamp.

In Lithographically Controlled Wetting, the stamp is gently placed in contact with a liquid thin film spread on a substrate. Capillary forces drive the solution to form menisci under the stamp protrusions. The solution remains pinned to the protrusions upon solvent evaporation. As the critical concentration is reached, the solute precipitates from solution onto the substrate, giving rise to a structured thin film replicating the pattern of the stamp. The process yields nanometer resolution and can be effectively used to promote self-organization in a confined space delimited by the stamp's feature.[22]

2.2.1 Chemical properties of PDMS

Several curable polymers may be used as structural material for elastomeric stamps. Polydimethylsiloxane (PDMS) has the advantages of being optically transparent and having a low surface energy, PDMS is one of the most used materials for fabricating microfluidic devices.

PDMS has inorganic siloxane backbone with methyl groups attached to silicon. (see fig.2.5)

Dimethyl siloxane (fig. 2.5b) are polymerized with an alkali catalyst. Small quantities of hexamethyl disiloxane are added to terminate the siloxane chains. To reduce mold shrinkage low MW siloxanes can be removed by solvent extraction or thermal treatment. In solvent extraction, volatile siloxane is removed by washing in methanol; in thermal treatment the polymer rubber is steamed or air stripped at 250°. These processes reduce the volatile fraction from around 10% to less than 2%. Silicon based elastomer is ten times more permeable to gases than other rubbers. The solubility of gases in polysiloxanes is similar to that for other polymers, but the diffusion coefficients are much higher. PDMS is soluble in chlorinated hydrocarbons, aromatic hydrocarbons, aliphatic hydrocarbons. It is moderately soluble in ketones, esters, ethers, but insoluble in alcohols and water. PDMS is commercially available in various forms and is produced by Dow Corning under the trademark Sylgard 184. The silicon oil is shipped separately from the initiator Both components are mixed in ratio 10:1 or 5:1 and cured either by temperature or UV exposure. After curing PDMS becomes durable elastomer, consequently it conforms to surface to which comes in contact; it is resistant against humidity and thermal gradients, but it can be swollen by its solvents.

Elastic deformation can limit the aspect ratio of the structures, because low aspect ratio may lead to sagging of non-contact regions, viceversa too high aspect ratios may turn out in collapsing free standing replicas.

Surface properties of PDMS can be manipulated with oxygen plasma treatment to increase the number of the hydroxyl groups on the surface and change the surface hydropho-

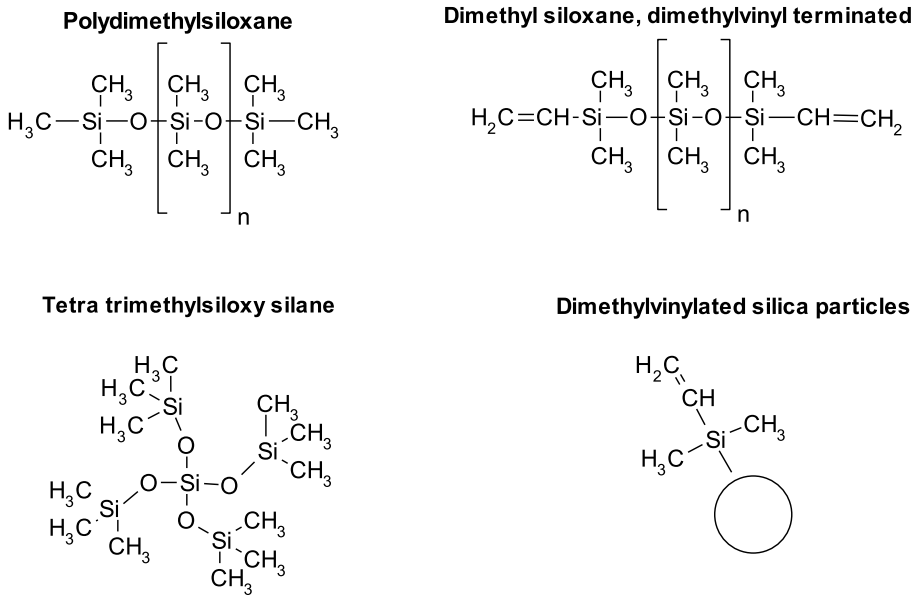

Figure 2.5: Polydimethylsiloxane and its components in commercial formulation Sylgard 184 provided by Dowcorning..

bicity into temporary hydrophylic.

Many patterning protocols have been evaluated starting from PDMS stamps,(i.e. microcontact printing), and most of them have been downscaled to nanopatterns. Microcontact printing uses the protrusions characteristic of the PDMS replica, to transfer a self-assembled monolayer to the substrate surface, by conformal contact, whereas micromolding in capillaries takes advantage of the PDMS stamp low surface energy, to infill a polymer or its precursors inside the nanometric channels.

2.2.2 Replica molding

The process of replica molding yields high resolution fidelity in the polymerization step of PDMS on the surface of master. The injection molding technique, applied to PDMS, profits similar results as replica molding from casting of the liquid prepolymers on the master. As the polymerization process starts immediately after the mixing of the two components, injection put in place after some time from the mixing, would result in a high occurrence of defects within the bulk polymer or near the surface, because the shrinking effect will enlarge microscopic defects, but there will be no relaxation of the polymer chains to partially mitigate it.

An example of the microfluidic device obtained by replica molding is shown in fig 2.6

. To enhance the releasing from the master, which is anyway favored by the low surface energy of cured PDMS, masters are often subject to silanization vapors. The silanization has been optimized to reduce any effect on the polymer replica. The presence of silane film, which undergoes reorganization during the thermal process of curing PDMS, may be irrelevant for micrometric sized structures, whereas when dealing with nanometric patterns, the silane layer account as additional 2D layer replicated by PDMS.

Large integration of multilayer structures is possible with a strategy of alignment and curing of superimposed PDMS replicas.[23] Spin coating PDMS precursors at 4000 rpm produces

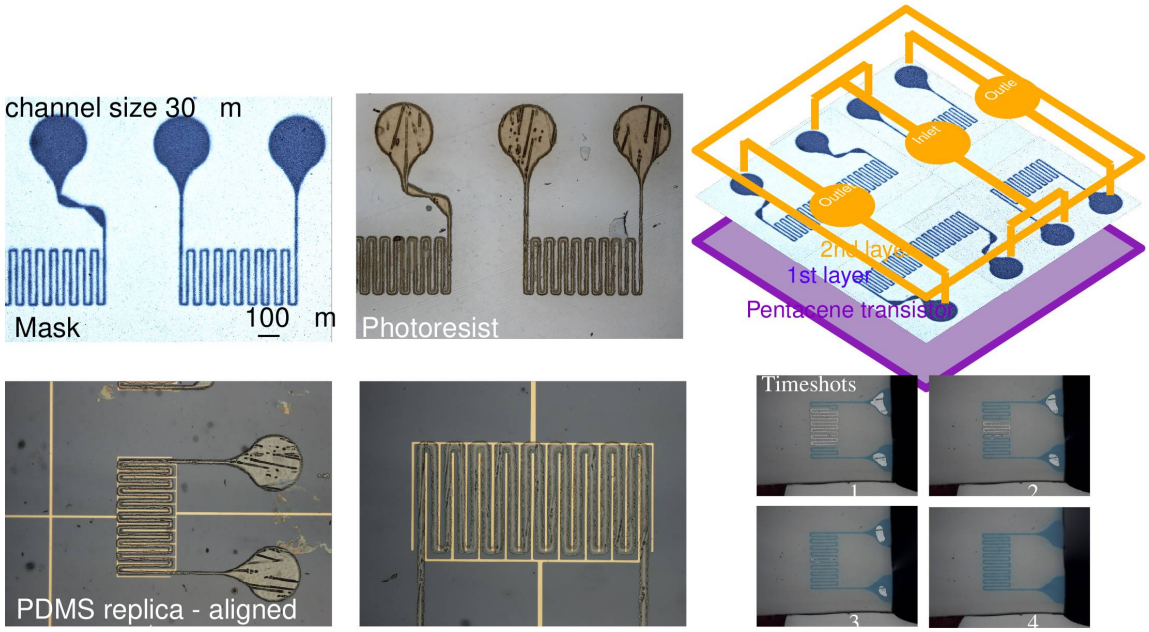

Figure 2.6: Consecutive steps in replica molding process. Starting from the mask obtained by optical reduction, we obtained the replica in PDMS after the photolithographic process. The replica is afterward aligned on the test pattern of FET device. Time shots of infilling by capillary forces is provided with blue dye.

a thick layer ($10\,\mu m$), which is partially cured, detached and aligned on top of another PDMS layer. A following curing step bonds the whole structure over the underlying silicon wafer.

Access holes are obtained by piercing PDMS with glass capillaries in such a way to preserve free channel inlet sections and dust free surface around the hole via. This avoids that dust prevents sealing of the microfluidic device and changes the flow lines between the vertical and horizontal channels.

The curing temperature has almost no influence on resolution of micrometer sized structures, although it accounts for the success of the process when replicating features with characteristic size of a few nanometers. In fig. 2.7 there is an example of replica of $30\,nm$ high periodic pattern ($270\,nm$ width $\times$ $30\,nm$ height) obtained at 100 ° C in 15 minutes.

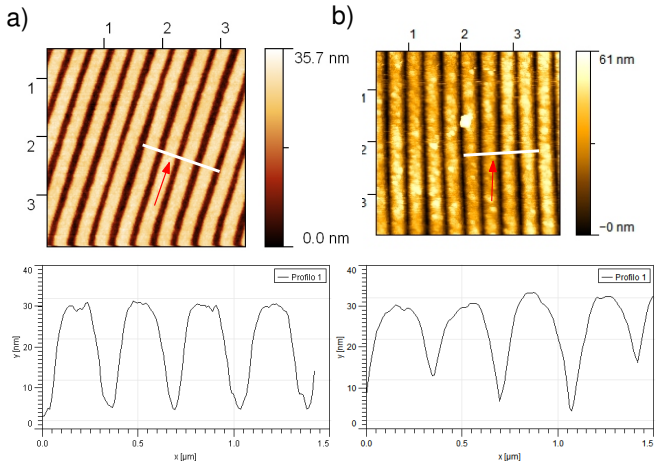

Figure 2.7: AFM images of submicrometric structures in PDMS. The replica is done on a master with periodicity of $350\,nm$, with curing temperature T = 100 °C. a) AFM tapping mode image of the polyethylene master, b) AFM tapping mode image of the PDMS replica.

2.2.3 Surface modification of PDMS

The most adopted precess in chemical modification of PDMS is oxygen plasma treatment. Low power plasma produces exposure of hydroxyl groups on the surface in contact with plasma, and therefore enhances its hydrophylicity. The surface forces of the modified plasma treated PDMS are comparable to those present on naturally high-energy interfaces, such as mica. However, water condensing on such hydroxylated interface determine the reconstitution of dioxygen bonds which recover the original material hydrophobicity. Surface oxidation by means of plasma treatment may be followed by silanol chemistry for attachment of 3-aminopropyl, or radical chemistry, for attachment of acrylic acids, acrylamide, dimethylacrylammide, 2-hydroxyethylacrylate, PEG-monomethoxyacrylate. Also non covalent modification of the surface has been reported by means of anionic coatings of sodium dodecyl sulfate.[24]

A peculiar approach in surface modification consists of using sol-gel process to form nanometric silica particles throughout polymerized PDMS. To form such particles a precursor soluble in the PDMS matrix, such as tetraorthoethylsilicate (TEOS), is hydrolyzed.

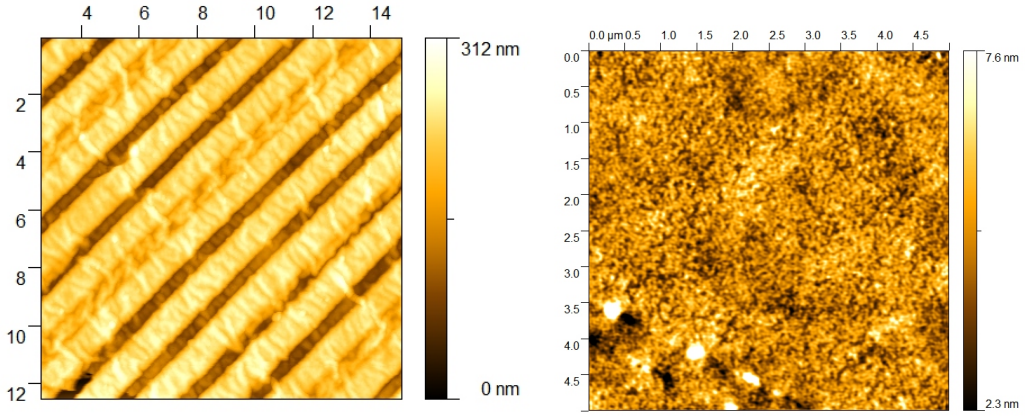

Figure 2.8: AFM images of submicrometric structures in PDMS after formation of silica nanoparticles on the surface.

Particles are formed through the condensation of hydrolyzed silanes, catalyzed in acidic or basic environments.

$$\mathrm{Si(OR)}{+}2\mathrm{H_2O} \rightarrow \mathrm{SiO_2} + 4\mathrm{ROH}$$

This approach proved to be effective in reducing the adsorption of peptides in few hours, and increasing the hydrophyilicty of the PDMS native which brings contact angle from 108° to 90°.

2.2.4 Conformal contacts and sealing

Technological aspects regarding the integration of a microfluidic device on top of the active area of the sensing devices (i.e. field effect transistors), concern the capability of the complete ensemble to sustain the pressure of the actuating flow, in special case when one or more surfaces are hydrophobic. The mechanism to ensure sealing of fabricated devices rely on two strategies:

1. evaluation of the maximum pressure sustained by the microfluidic device, by modeling the peeling force[25] between the PDMS surface and the underlying substrate;

2. adding external constraints which damp the deformation of the PDMS under fluid pressure, and maintain the fluid confinement. It is worth noticing that microfluidic fabrication, sealing is usually achieved with multilayer PDMS, with partial curing steps in the fabrication process.

Starting from the Hertzian contact under normal load P_0, the apparent Hertzian load P_1 is given by[26]

$$P_{1=}P_0 + 3\gamma\pi R + \sqrt{6\gamma\pi R P_0 + (3\pi R\gamma)^2}$$

where γ is the adhesion energy, and $R = R_1R_2/(R_1 + R_2)$ the radius of contact. From the above equation, it is possible to derive the pull-off force, given by (when the surfaces are separated):

$$P_{pull-off} = -3/2\gamma\pi R$$

The adhesion force generated by the Laplace pressure is given by:

$$F_w = 2\pi r\gamma(\cos(\theta_1) + \cos(\theta_2))$$

where r_m is the radius of meniscus.

2.2.5 Virtual prototyping

In order to evaluate the suitable geometry for a microfluidic device that confines liquids with volume ranging around 100 nL, we simulate the behavior of the material system with help of a finite element software (Comsol Multiphysics) that provides numerical solution to fluid dynamic and structural mechanics equations, relevant to our problem. The microfluidic part fabricated by photolithography and replica molding is coupled to the hydrophobic structure at the bottom. We choose to decouple the fluid dynamic from the stress-strain model, because

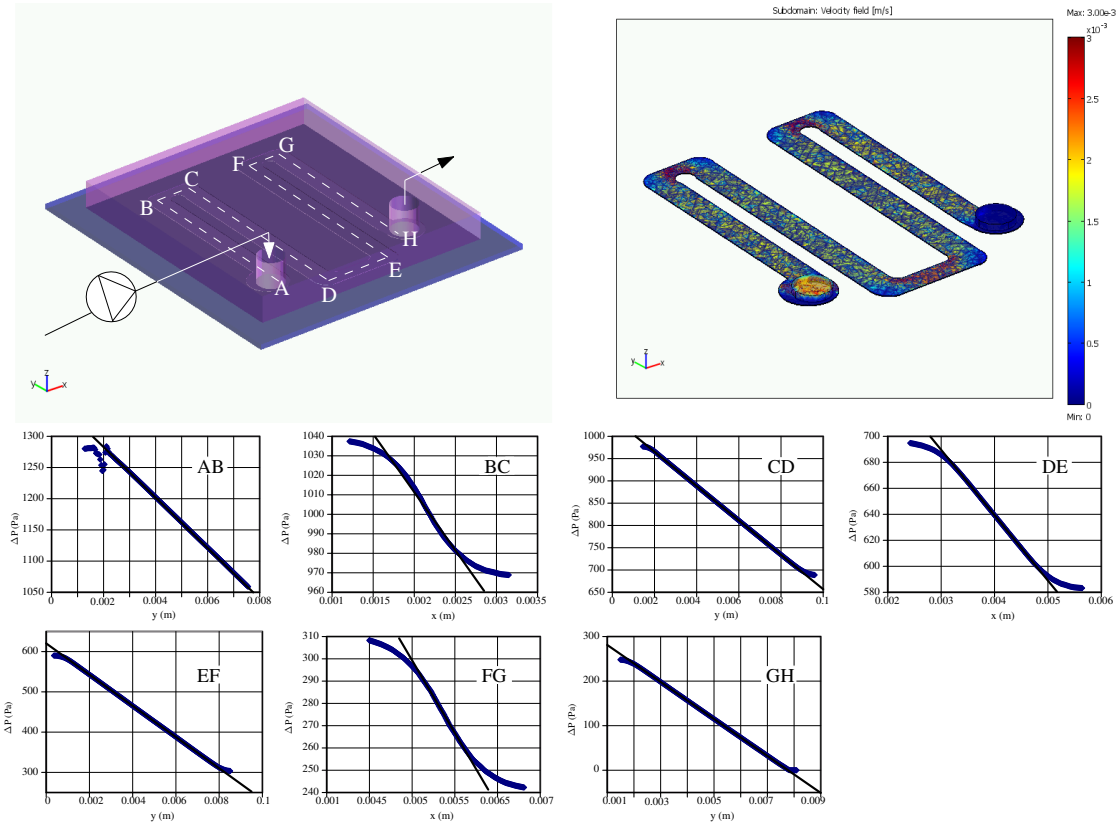

Figure 2.9: The geometry of the microfluidic device comprising the actuating mechanism is shown schematically on the left. The liquid enters a microchannel of 300μm width $\times$ 20μm height from inlet and leaves it in incompressible fashion from the outlet. On the right it is shown the result of calculation of the velocity field, the geometric grid is still visible in the result due to aspect ratio of structure and to transparency set on the image. Below the pressure trends resulting from calculation in characteristic middle sections.

of clarity, assuming that the pressure of the fluid within the microdevice is a monotonic characteristic without sharp discontinuities. The fluid velocity and pressure in the microcell is calculated solving the Navier Stokes equation, with boundary conditions determined by the external actuating syringe (see fig.2.9) The pressure difference is set to zero at the outlet of the microdevice, whereas at the inlet the condition is set on the velocity of the fluid. This corresponds to direct configuration because experimentally we set the velocity of the moving pistons of the syringe and the pressure within the microdevice may be variable due to resistance opposed by viscous forces.

The resulting profile of the pressure acted by the fluid is then applied to the structural PDMS elastomer. (see fig. 2.10). Besides this pressure, adhesion force due to hydrophobic interaction is set on the interface between the microdevice and the hydrophobic organic layer. If deformation due to pressure is higher than 10 nm, hydrophobic interaction forces stop to be dominant and the sealing of confinement within the microchannel is potentially lost. If the surface of PDMS is silanol activated (i.e. plasma treatment), the adhesion force is notably higher, forming bonds which undertake higher pressure, although these bonds can not be released.

2.3 Glass microchambers for cell cultures

Microfluidics can be useful to reduce the volume of *in silico* experiments to the space occupied by a single cell, in preconditioned environment. Moreover the same cell can be detached and escorted to specific areas, where chemical stimulus is provided by nanoliter volume delivery. The electrochemical response and membrane potential differential can be detected by organic electronic device nearby.

We fabricate glass microchamber to explore the possibility to control the cell positioning, with fluidic technology. The process is based on the following steps (see fig. 2.12):

1. A thick AR P 3210 photoresist film (10μm), spin-coated on pirañha treated glass, was UV exposed, through high resolution mask. After development, the resulting pattern was post-baked in oven at 130 °C in order to cross link the polymer matrix and ensure adhesion on glass.

2. The resulting glass+photoresist was etched in a small volume of HF acid solution (10% diluted in water), in sealed beaker for 30 minutes, paying careful attention on the neutralization of the waste with $Ca(OH)_2$.

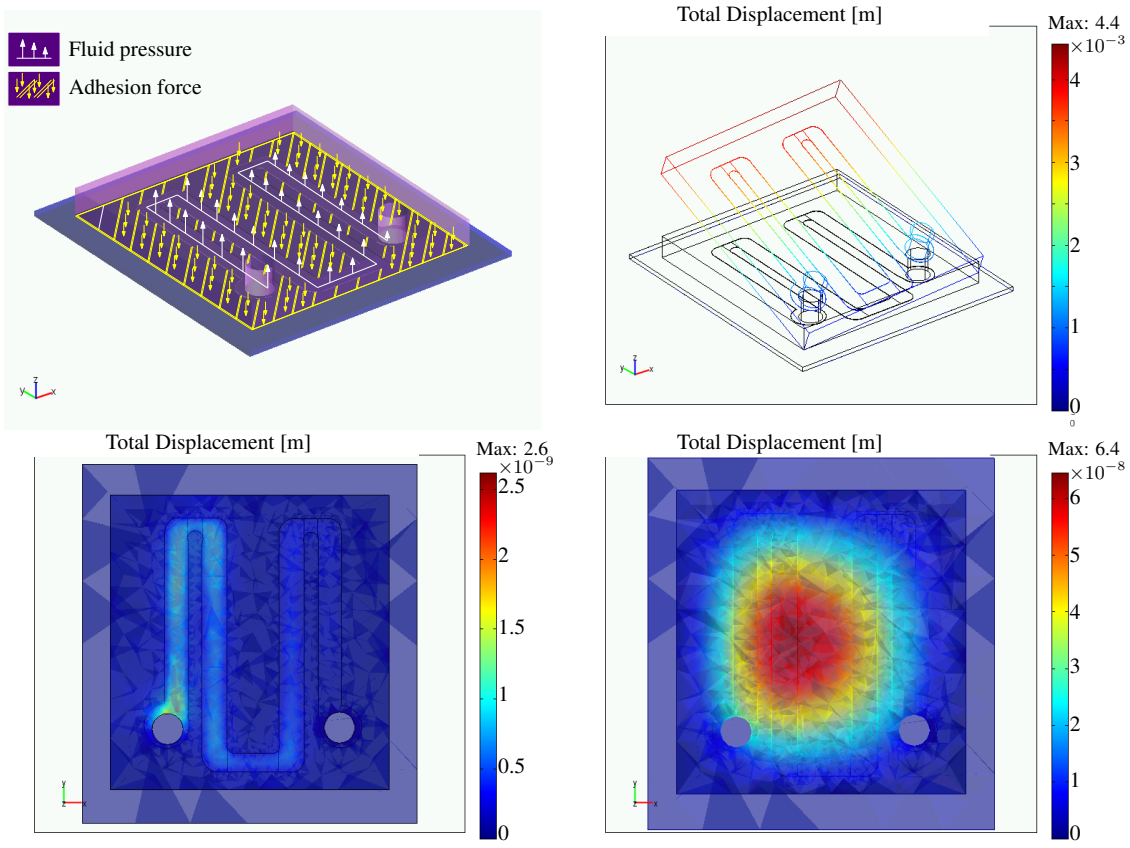

Figure 2.10: On the left the force layout on the boundaries of the microfluidic cell. On the microchannel walls the fluid exerts a pressure normal to the surface, in particular the upper part, on the lower surface of PDMS replica there is adhesion contact between two hydrophobic surfaces. The plot at right up represents the displacement (also due to deformation) of the chip if the device was constrained in just one physical point. In the lower left corner the displacement in case of strong adhesion between the PDMS and the substrate (for example after plasma treatment). At the lower right corner, there is the displacement in the case of additive external constraint along the PDMS border.

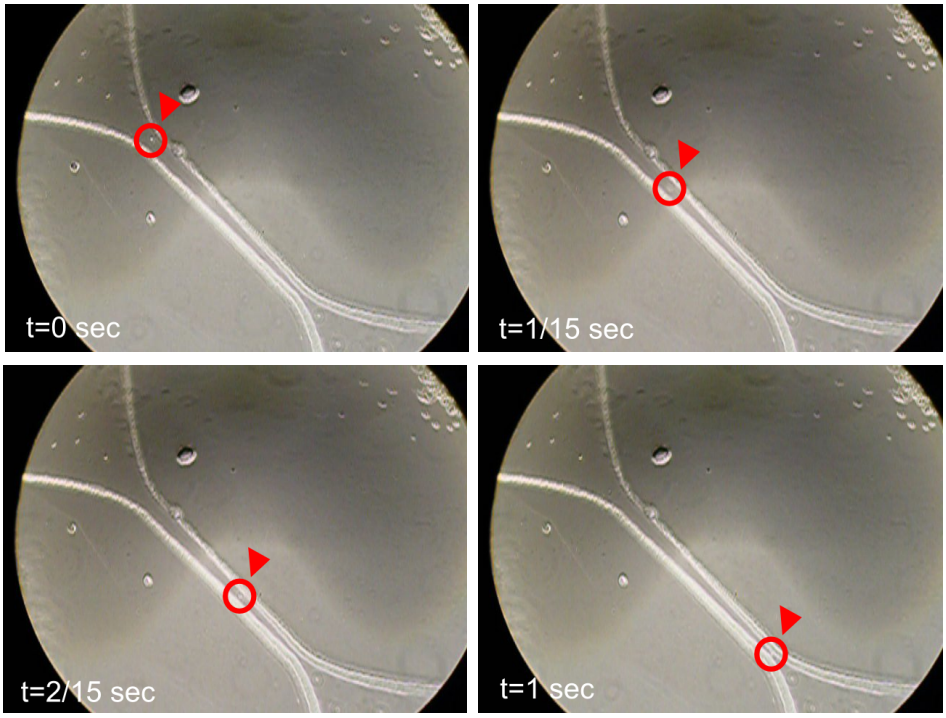

Figure 2.11: Video rate picture snapshots of a single cell moving through the channel of the glass microchamber. Video rate is fixed to 1/15 s.

HF etched glass isotropically, whereas the areas covered by the photoresist were preserved. In such a way, it was possible to etch a channel of variable size, up to the passage allowed for a single cell.

After obtaining the glass structure, a polymer cap was added to seal the chip. Differential scanning calorimetry were carried on to select the optimal condition for sealing without clogging the thin glass cavities. Infilling imaging of the microfluidics channels has been acquired with high resolution camera to verify that the volume occupied by the liquid was precisely confined.

Microfabrication of glass microchamber involving solution-process of platinum thin films and glass etching was set up for simple design of linear fluidic channel with parallel electrodes. See (fig.2.13 *bottom-left*) for result. The channel section obtained with etching

techniques has trapezium shape with resulting lateral dimension increased of ~40 % with respect to mask features. The process guarantees intrinsically the alignment of the electrodes to the microfluidic channel, and the low roughness of the metal electrodes over which an elastomeric cover is placed and treated thermally to enforce the sealing of the microdevice. In this case platinum thin film has thickness of ~60 nm (see Section 3.2), whereas glass microchannel has depth of ~1.5 μm. The microchannel can be observed with optical microscopy (reflection and transmission), being the PDMS cover transparent to light in the visible range. Three sets of samples with characteristic channel width of 20, 30 ,40 μm (see fig.2.12e)) has been produced for test on glioma cell cultures.

An initial build for external infilling actuator has been set up and checked for microfluidic seal against transistor active area. We tested the tightness of fluid compartment, varying the infilling pressure. In this case the infilling pressure is modulated to be less than the adhesive seal obtained between the PDMS cover and the underlying transistor.

The velocity field within the microenvironment will affect the result of cell attachment and viability assays. The flow, at which cells are seeded in first time on the substrate, is responsible for active positioning on the substrate. At the same time the velocity of medium, during feeding, has to be controlled to avoid detachment of biological samples with mixing.

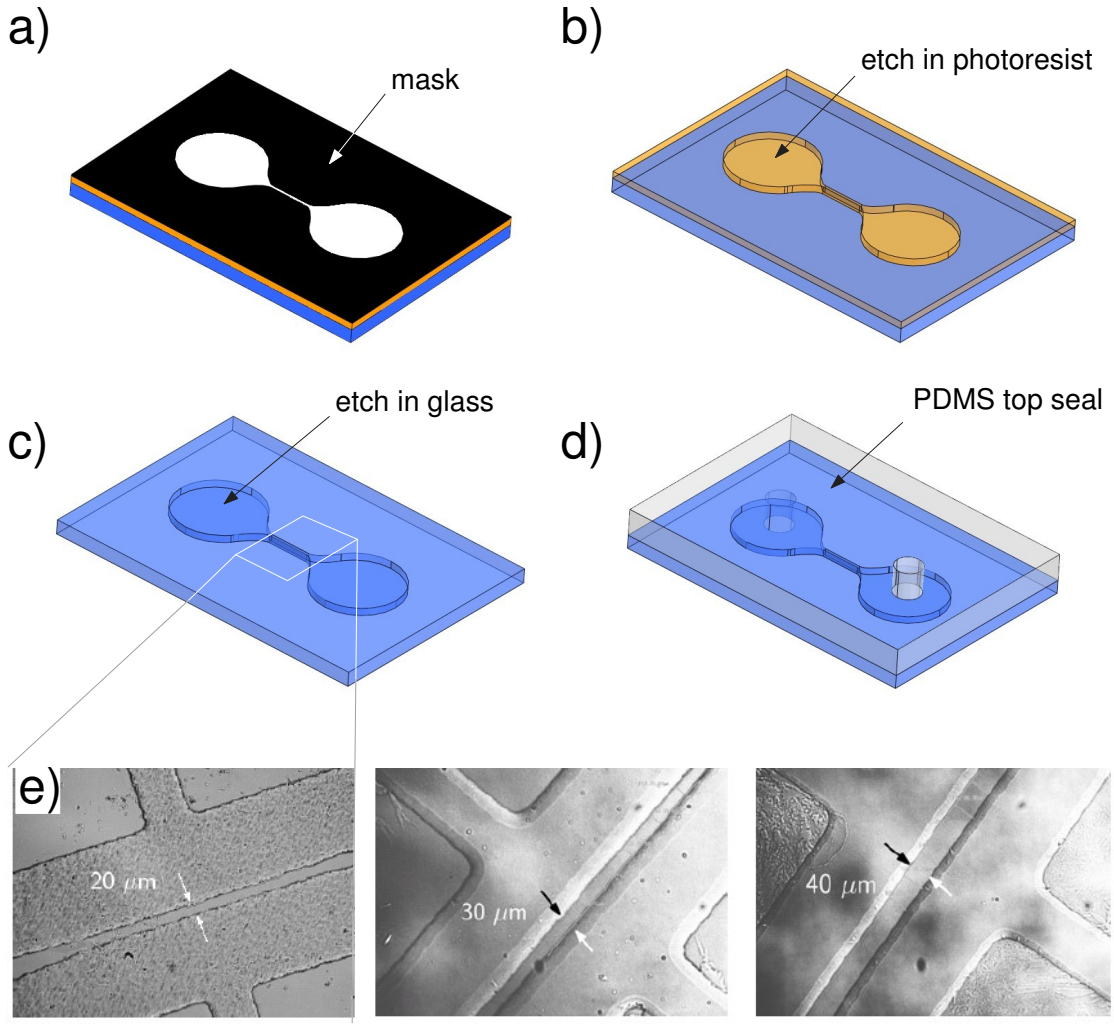

Figure 2.12: Fabrication of glass/PDMS microdevice for cell positioning. a) UV exposure of thick photoresist spin coated on glass, b) Development of photoresist and post-backing, c) Isotropic wet etching of glass, d) Top sealing with PDMS, e) Optical images of variable-width μ-channels obtained with different UV masks.

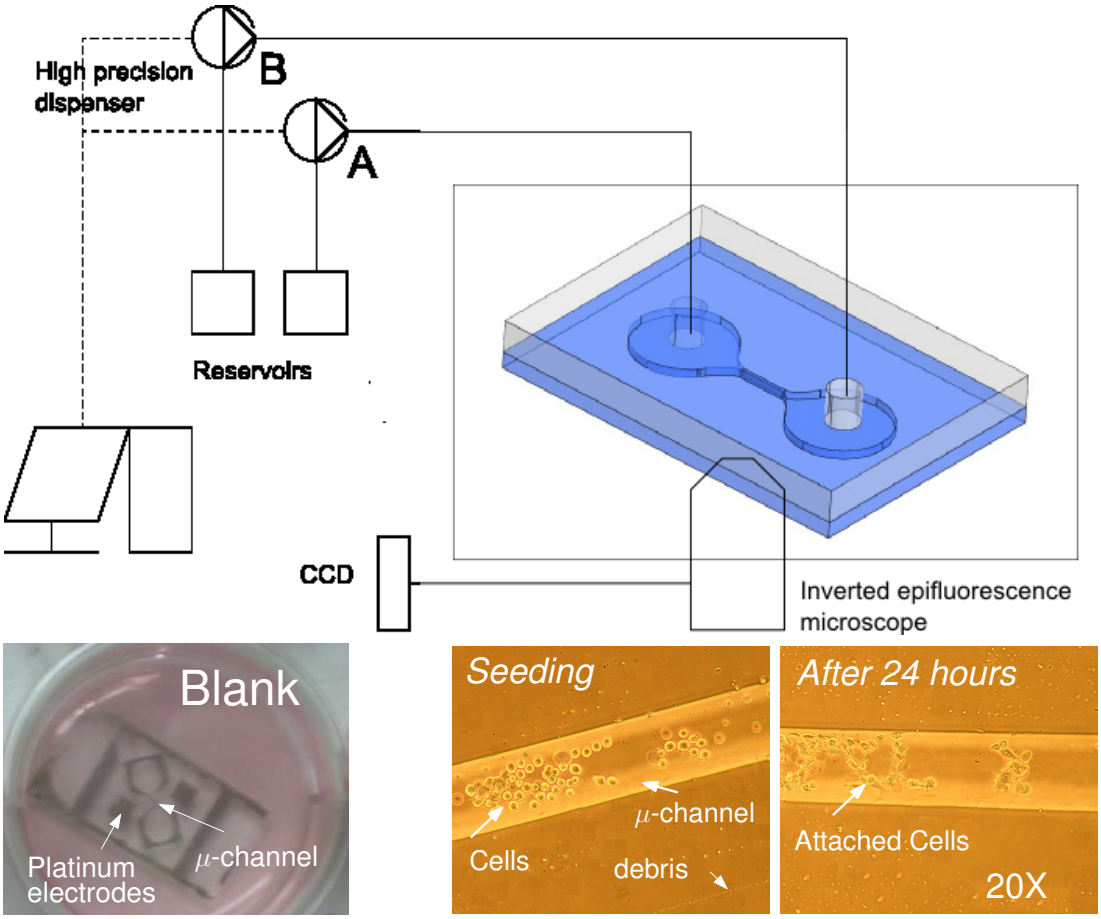

Figure 2.13: Diagram of the external infilling actuator setup on the inverted microscope. Optical micrograph of glial cells living within PDMS microchannel. Color enhancement is provided to distinguish change in morphology of the same cells after 24 hours. The number is reduced due to detachment occurring after medium replacement.

Chapter 3

Platinum electrodes fabrication

In the following chapter, I present experimental results concerning the fabrication of platinum electrodes, obtained from precursor in solution, platinum-carbonyl. The process is based on two soft-lithography techniques: micro-molding in capillaries and lithographically controlled wetting. The design of the elastomeric stamp has been optimized specifically to obtain submicrometric wires with conductance ~ 34 S/cm. The work done to achieve this result is reported in section 1.

This technique can be adapted to work on different length scales, envisaging the possibility to assemble a device completely fabricated with elastomeric stamps. In section 2, I report the work done in this direction, to prepare a field effect transistor, all organic, by additive soft lithography.

3.1 Conductive Sub-micrometric Wires of Platinum-Carbonyl Clusters Fabricated by Soft-Lithography

A major effort in nanotechnology has been devoted to the patterning of active materials into size and shape controlled structures, to achieve the ambitious goal of controlling physical

properties through the control of materials at different length scales.[27] However, the interconnection of active nanostructures with the macroscopic world is still an open problem that severely limits many applications. In order to connect systems across length scales, technology requires easily processable highly conductive wires that are stable under ambient conditions. Noble metals, such as Au and Pt, widely used in microelectronics, are ideal candidates for these purposes due to stability versus oxidation combined with a high conductivity. Several methods have been proposed for fabricating highly conductive micro- and nanowires. Among them, in situ controlled deposition of metal-organic precursors from vapor phase, followed by Focused Ion Beam (FIB) or Electron-Beam (EB)[28] decomposition, are quite effective, widely adopted in laboratory research. However the apparatus required are expensive and the technique is difficult to upscale, which limit their technological application. A breakthrough approach involves material precursors, which can be processed and patterned from solutions, viz. within the same technological platform as organic semiconductors.[29]Examples include Ag[30–32] or Au[33] nanorods, Cu and FeS[34,35] nanowires, and metal oxides semiconductors.[36] Here I describe the use of solution processable metal carbonyl clusters for conductive nanowires. They offer the possibility to process several metals or even combinations (alloys) of different metals from a variety of solvents and mild curing conditions. Evidence supporting this approach comes from solution casting of water/2-propanol solutions of $[Pt_{3n}(CO)_{6n}]^{2-}$ (n=4-6) on several substrates which yields the preferential formation of Pt nanowires over other morphologies.[37] Moreover, as inferred from TEM images, well-defined Pt morphologies, including Pt nanowires, have also been obtained by preparing $[Pt_{3n}(CO)_{6n}]^{2-}$ (n=4-6) dianions in the micropores of zeolites, followed by thermal decomposition. Nonetheless, both of these approaches do not yield the formation of ordered structures. The problem of promoting a controlled highly ordered assembly of metal clusters is overcome by confining the deposition of Pt carbonyl clusters with the use of stamps[21,22,38] therefore changing the degrees of freedom and the time scales of the deposition. Within soft-

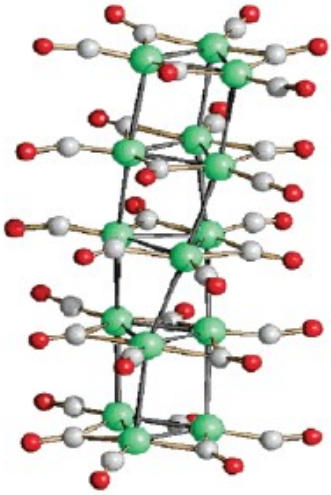

(1)

Figure 3.1: Diffraction pattern of the annealed film of 1 cast on glass. The Miller indexes, which correspond to the metallic Pt phase, have been reported.

lithography framework, I used Microinject Molding in Capillaries (MIMIC)[39,40] to obtain a pattern of sub-micrometric stripes of the Pt carbonyl clusters $[NBu_4]_2[Pt_{15}(CO)_{30}]$, and I compared its conductive properties with continuous thin solid films. Furthermore the Pt carbonyl μ-stripes are turned into metallic Pt nanowires after thermal decomposition. Decomposition of the platinum-carbonyl and precipitation of structured crystals from different solutions have been studied in sub-micrometric channels.

The molecular precursor employed for the fabrication of Pt wires is the $[NBu_4]^+$ salt of the $[Pt_{15}(CO)_{30}]^{2-}$ (**1**) cluster anion (Fig.3.1) for several reasons. First, it can be easily synthesized in water from commercial Pt salts, as recently reported.[6] Moreover, molecular species, depending on the cluster size and the nature of the counterion, self-assemble upon crystallization to yield molecular wires,[5] which are organized into 1-D, 2-D, or 3-D structures.

3.1.1 Films

Films of **1** were prepared by drop casting 20 μL of its solution (0.6 g/L) in dimethylformamide (DMF) or tetrahydrofuran (THF) on glass. The nature of the deposited materials largely depends on the experimental conditions. Micro-IR experiments on samples obtained by drop casting in air show that the deposited material retains its molecular carbonyl nature when volatile solvents such as THF or acetone are used. Conversely, when a less volatile solvent such as DMF is employed, the Pt-carbonyl clusters decompose during evaporation in air to give Pt colloids, which are contaminated by organic species, arising from the tetraalkyl ammonium cations. This solvent-dependent decomposition behavior is not observed when depositing the cluster solutions under a nitrogen flow; in this case, in fact, the deposited material always retains the carbonyl molecular nature of the precursor, independently of the solvent used. Moreover, the samples grown under a nitrogen atmosphere show rod-like crystals, which are more than 50 μm long with an aspect ratio of >10:1 (see Fig.3.2a).

The observation under crossed polars (Fig.3.2b) shows the typical behavior of optically anisotropic materials; i.e., the crystals appear colored under crossed polars, where the colors range from green to yellow depending on the local thickness. Evidence of light extinction in regions of the crystals indicates that each crystal is formed by several domains, whose length ranges between 2 μm and 15 μm. No evidence of preferential orientation of these domains is observed. On the other hand, the samples grown in air appear inhomogeneous and very rough; no sign of birifringence has been observed by optical microscope. The different appearance of the samples deposited under nitrogen compared to the ones obtained in air is consistent with the fact that these compounds are air-sensitive in solution. The decomposition of **1** is confirmed by the spectroscopic evidence that **1** loses its molecular carbonyl nature when deposited in air. In all cases, thermal treatment in air at temperatures higher than 100 °C decomposes the carbonyl clusters removing completely the organic components.

Thermogravimetric Analysis (TGA), shown in Fig.3.3, clearly indicates that already at

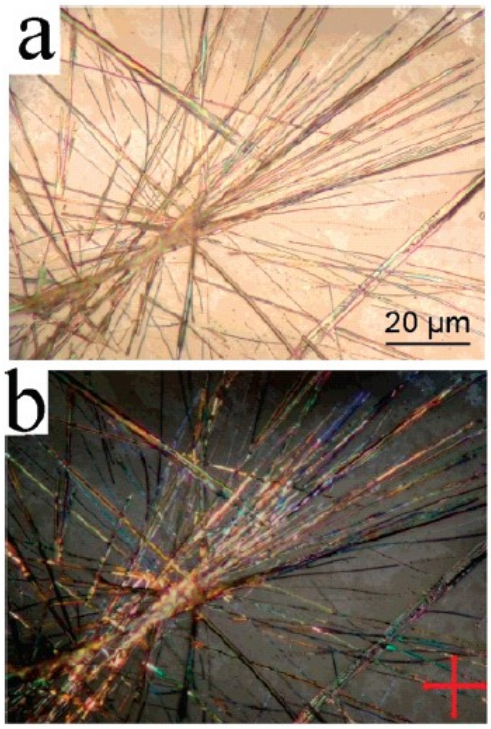

Figure 3.2: Optical micrographs (magnification 50x) of **1** on glass after deposition under nitrogen. (a) Micrographs taken under unpolarized light. (b) Micrographs taken with crossed polars oriented along the axes of the image.

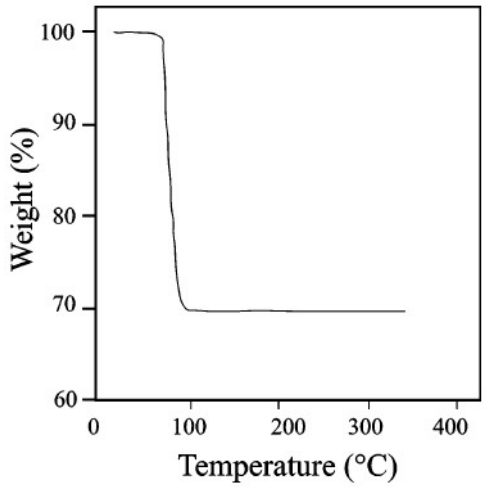

Figure 3.3: TGA of **1**. The weight becomes constant at ca. 70% of the original above 100 °C (theoretical Pt content for $[NBu_4]_2[Pt_{15}(CO)_{30}]$ is 68.8%).

ca. 100 °C all the carbonyl ligands and the $[NBu_4]^+$cations are removed from **1** leaving only metallic Pt.

3.1.2 Patterning of Sub-micrometric Stripes.

The sub-micrometric stripes of **1** have been fabricated by Microinject Molding In Capillaries (MIMIC). A stamp made of polydimethylsiloxane (PDMS), whose motif consists of parallel protruding lines (125 nm thick, 300 nm width and 740 nm pitch), is placed in contact with the surface. The grooves between the protrusions in contact with the surface form the micro-cavities, which once in contact with the silicon oxide substrate delimit the sub-micrometric channels. When the solution is poured at the open end of the stamp, the liquid spontaneously fills the channels under the effect of capillary pressure. After the complete evaporation of the solvent (using DMF, 24 h at room temperature) the stamp is gently removed. The self-organization of the solute enters into play at the later stages of shrinking, when the solution reaches supersaturation. Spatially organized nanodots or crystallites are fabricated by exploiting dewetting, ripening, and crystallite growth.

3.1.3 Finite Elements Simulation of the Microchannel Infilling.

The infilling of PDMS-confined μ-channels is due to the capillary force and depends on surface tension and friction between the solvent and the channel walls. Equating these contributions to pressure differences arising in the channel, it is possible to determine the local rate of flow, thus the time necessary to fill the microchannel. In this manner, it is possible to control the distance flown by the solution inside the channel

$$Re \cdot f \cdot (\eta \cdot w)/(2 \cdot D_p^2) \cdot z = 2\sigma \cos(\theta)/D_p \tag{3.1}$$

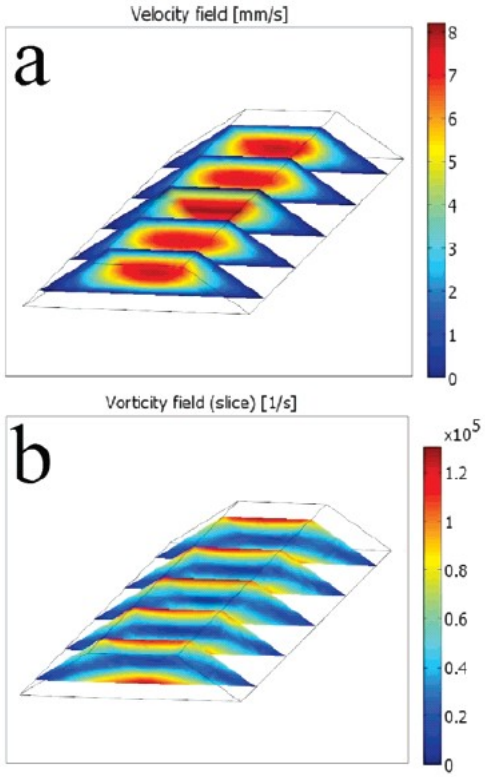

Figure 3.4: Finite elements simulation of the μ-channel infilling. (a) Velocity distribution for the main section of the μ-channels (mean value of 8 mm/ s). (b) Vorticity distribution for the main section of the μ-channel.

where Re is the Reynolds number, f, a geometrical factor, η, the viscosity of the solution, w, the velocity of the fluid along the main stream, σ, the surface tension, θ, the contact angle of the meniscus, and D_p, the wet perimeter of cross-section. Applying (eq 3.1) on a finite elements grid over the system domain we obtain a velocity field, which depends on the presence of the PDMS mold.

The mean velocity calculated for our system is 8 mm/s which, using a stamp 6 mm length, corresponds to a time of infilling of 0.75 s. As depicted in Fig.3.14, the rate of the solution inside the microchannels is not constant but it tends to be faster in the center of the í-channel with respect the border of the í-channel. Furthermore, the simulation shows a high vorticity during the infilling (the vorticity defined as $[(w_y - v_z)^2 + (u_z - w_x)^2 + (v_x - u_y)^2]^{1/2}$ where x, y, z are the spatial coordinates, u, v, w the corresponding velocities, and u_y the derivative of

u with respect to y), which indicate the laminar flux is distorted by geometry of the channel. Although these effects are not intense enough to induce turbulence in the flux, they cause inhomogeneous distribution of the solute along the μ-channels when the solvent shrinks.

As shown in Fig.3.5 μ-stripes of **1** exhibit birefringence under a polarized optical microscope, with domains exceeding 20 ím. The observation under crossed polars shows that the μ-stripes appear homogeneously colored. This indicates that their thickness is almost constant over the entire stripe. By rotating the microscope stage (viz. the crystal orientation vs the polarized light) the μ-stripes extinguished (became dark) in four positions at intervals of 90° when the crossed polars were oriented parallel (perpendicular) to them while they are brightest when the crossed polars were oriented at 45°. The occurrence of light extinction at the same orientations for all the domains indicates that the μ-stripes were grown with the same orientation. This means that the confined deposition has induced a coherent, long-range order along the direction of the stripes. As expected the stripes deposited in air do not exhibit birefringence.

3.1.4 Electrical Characterization.

The electrical properties of the μ-stripes were studied using a two-probe configuration. Two gold pads to be used as electrodes were thermally evaporated on top of the pattern of μ-stripes through a square TEM grid (50 mesh) (Fig.3.5). The length of the í-stripes was measured using optical microscopy and the width and the thickness of the μ-stripes were measured analyzing the topography of the sample by AFM. It was observed by AFM and optical microscopy that not all the stripes are connected. It is thus relevant to consider the average number of stripes, which are connected, contributing to the current. The conductance of a single μ-stripe was calculated using the relationship $\kappa_{tot} = n \cdot \kappa_{single}$, where κ_{tot}, n, and κ_{single} are the conductance measured, average number of continuous stripes, and the conductance of each stripe, respectively. Although a small percentage of the devices (15%) exhibit an irre-

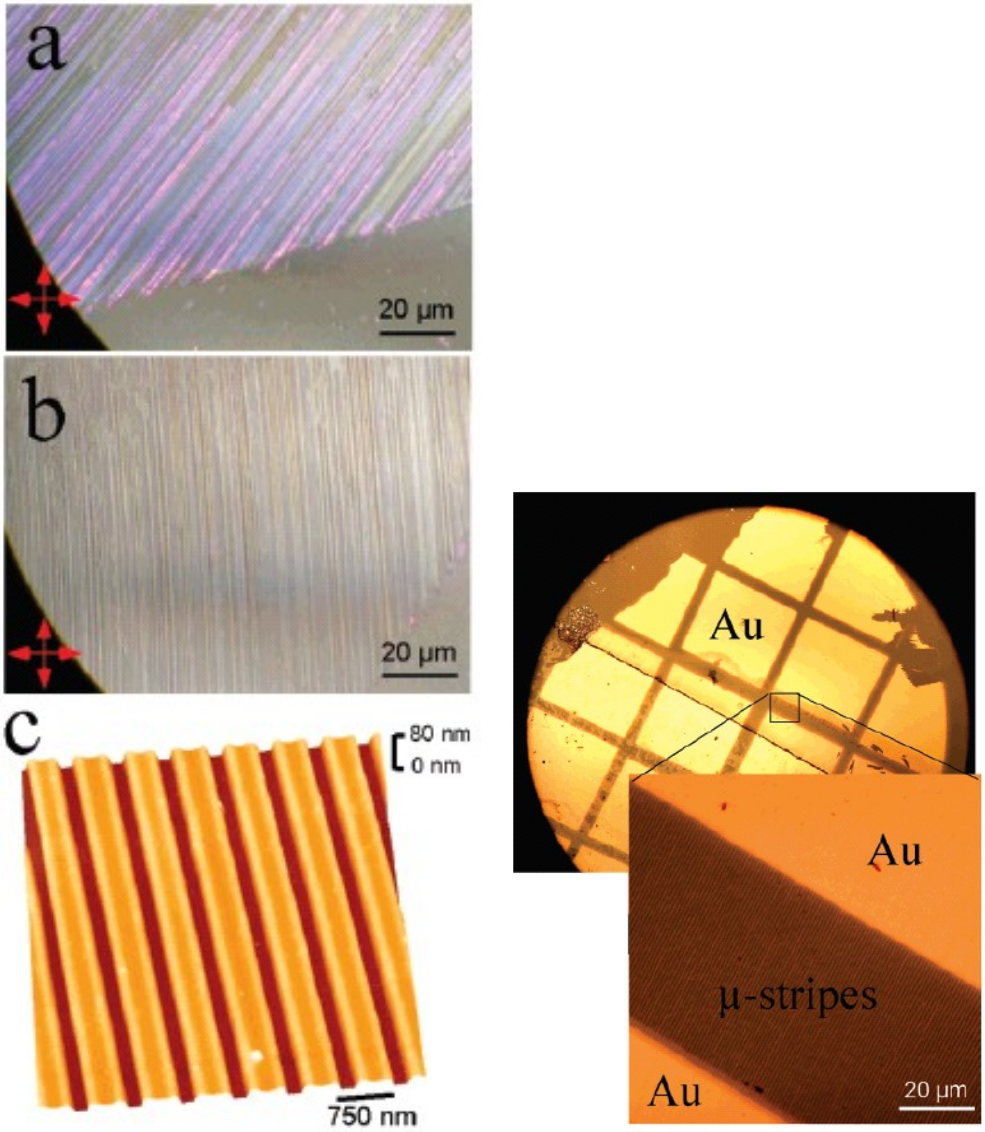

Figure 3.5: Optical micrographs of micrometric stripes fabricated on glass by MIMIC using $[NBu_4]_2[Pt_{15}(CO)_{30}]$ solutions under nitrogen, with crossed polars. (a) Rotated 30° with respect the polars and (b) parallel (perpendicular) to the polars. (c) Corresponding AFM images.On the right, the optical micrographs of gold pads evaporated on μ-stripes.

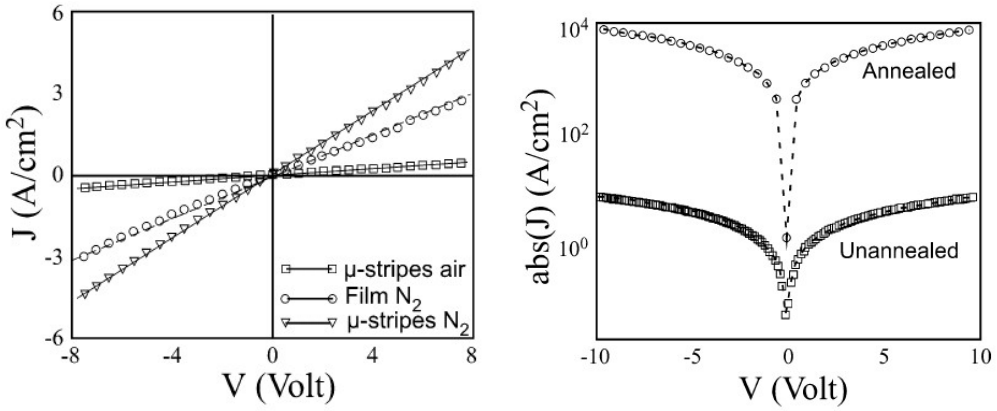

Figure 3.6: *Left*. Current density-voltage characteristic of 1: μ-stripes fabricated in air (□), drop cast film (◯), and μ-stripes fabricated under nitrogen (△). *Right.* Comparison of current density-voltage characteristic of annealed and unannealed μ-stripes of $[NBu_4]_2[Pt_{15}(CO)_{30}]$ fabricated under nitrogen (current density is plotted on log scale).

producible non-ohmic I/V curve, all kinds of samples (i.e., prepared in air or under nitrogen and the annealed and as fabricated samples) show an ohmic behavior in the voltage range -8 V to +8 V but with a different electrical conductivity.

Fig.3.6 shows the J/V curve of the μ-stripes fabricated in air and under nitrogen and the film prepared under nitrogen (the film prepared in air exhibit irreproducible behavior due to the higher number of defects).

Both the μ-stripes (fabricated in air protected by the stamp or fabricated under nitrogen) and the film drop cast under nitrogen exhibit an ohmic behavior in the voltage range -8 V to +8 V. It is remarkable that the μ-stripes fabricated under nitrogen exhibit an electrical conductivity of (2.1 ± 1.5) 10^{-2} S/cm, which is 1 order of magnitude larger than that of the corresponding thin film ($\approx$1.0 $\times 10^{-3}$ S/cm) grown by drop casting. On the other hand, the μ-stripes fabricated in air (thus with a partial decomposition of the 1 during the process) exhibit a conductivity of (7.1 ± 1.5) 10^{-4} S/cm, thus more than 1 order of magnitude lower with respect to the stripes fabricated under nitrogen. The reason of lower electrical conductivity in the μ-stripes fabricated in air can be attributed to the high numbers of the defects (grains boundaries, cracks, etc.) generated during the partial decomposition of 1. Furthermore, since

the decomposition is not complete, it gives rise to the formation of an ill-defined amorphous Pt-colloidal material highly contaminated by the organic products from the $[NBu_4]^+$ cations which are removed only upon thermal treatment. Conversely, the electrical conductivity is enhanced in the μ-stripes fabricated under nitrogen because they have a limited number of defects, resulting in a perfectly ordered crystalline material oriented along the direction of the channel. The deposition of the solute in a confined environment enhances long-range molecular order because the rate of deposition is slower (close to the quasi-equilibrium conditions) and the confinement depletes the number of stable nuclei that can be formed. As the lateral size of the channel is shorter than the characteristic length scales of nucleation and diffusion, ripening, and the lateral diffusivity of molecules are restricted, the stripes grow as a one-dimensional system, with a limited number of grain boundaries and defects, as already observed in other molecular systems such as organic semiconductors.

3.1.5 Effect of Thermal Annealing on μ-Stripes.

In the present case, a solution of platinum precursor in DMF was used. After preparation, the patterns were annealed in air at 150 °C for 2 h in order to achieve the complete decomposition of the carbonyl groups. Upon thermal annealing, the μ-stripes still exhibit an ohmic behavior (Fig.3.6) with an increase of the electrical conductivity to 34.6 ± 2.0 S/cm due to the decomposition of **1** to metallic platinum. Occasionally, after the annealing, small deviation from the ohmic behavior has been observed due to changes in the contact resistance between the gold pad and the Pt μ-stripes during annealing. On the other hand, the μ-stripes fabricated in air (i.e., partially decomposed during the process) limit its increase of the electrical conductivity upon thermal annealing to 2.15 ± 1.0 S/cm, due to the presence of defects originated during the fabrication process. Although the electrical conductivity of Pt wires obtained by our process is comparable to the electrical conductivity obtained in literature (80 S/cm at 20 °C), this value is still far from the electrical conductivity of the bulk platinum (10^5 S/cm). In order to

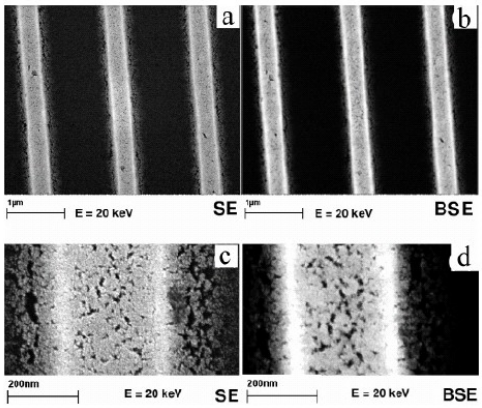

Figure 3.7: SEM images of Pt μ-stripes fabricated on Si: (a) a conventional secondary electron image; (b) obtained with a backscattered electrons detector, sensitive mainly to the sample composition; (c) zoom of a; (d) zoom of c.

understand this difference, an accurate XRD and scanning Electron microscopy investigation of microannealed μ-stripes was done.

3.1.6 Scanning Electron Microscopy and X-ray diffraction.

In Fig are reported two SEM images of the same portion of μ-stripes fabricated on Si, obtained with two different detectors.

Fig.3.7 are Secondary Electron (SE) images obtained with an In-Lens detector, sensitive mainly to the topography of the stripes. They show the rough surface of the stripes and the presence of holes and grains of different size that form during the thermal treatment. Fig.3.7b,d are obtained with a BSE detector and shows mainly compositional information. The μ-stripes show a bright contrast, as expected for a material with a high atomic number (Pt) on a substrate of low atomic number (Si). The roughness of the surface is still visible, but the uniform contrast along the stripe boundaries and inside the grains confirms the uniform composition of the stripes. These considerations are clearly confirmed by the results of the EDX measurements.

In Fig.3.8 are reported a low-magnification secondary electron image and the correspond-

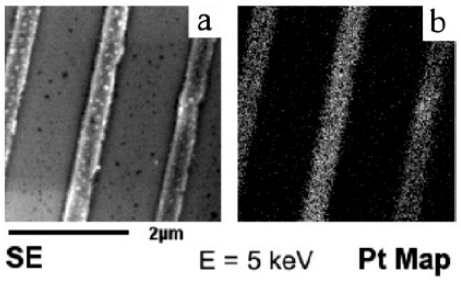

Figure 3.8: (a) Secondary electron image and (b) the corresponding X-ray map for Pt.

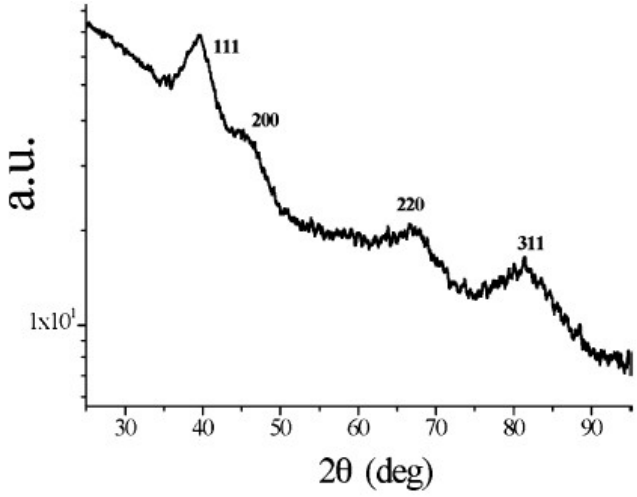

Figure 3.9: Diffraction pattern of the annealed film of **1** cast on glass. The Miller indexes, which correspond to the metallic Pt phase, have been reported.

ing X-ray map for Pt, i.e., an image obtained collecting only the characteristic X-ray of the Pt emitted from the sample during the observation. As expected the Pt is localized inside the μ-stripes.

The structure of annealed films of 1 has been studied by X-ray diffraction measurements. The diffraction pattern has been recorded by using the grazing geometry, i.e., by keeping the incident beam at grazing angle on the sample surface, to enhance the scattering contribution from the surface.

Fig shows the pattern obtained on glass substrate, but the same results have been obtained on silicon covered by native oxide. The films resulted formed by randomly oriented crystallites of cubic close-packed phase of the metallic Pt. The average coherent domain size,

estimated from the FWHM (full width at half-maximum) of the peaks, is lower than 4 nm.

3.1.7 Conclusions

Here we showed the possibility to pattern ordered arrays of sub-micrometric stripes made from platinum-carbonyl clusters. This example illustrates the concept and application of a singlestep bottom-up process that allows us to deposit size-defined stripes of a soluble molecular conductor. In this case long-range molecular order is achieved by solute deposition in a confined environment, because of slow deposition rate, hence quasiequilibrium conditions, and lateral confinement that depletes the number of stable nuclei. In such a pattern electrical conductivity is enhanced and tuned by the control of size, shape, and order of the molecular domains: $[NBu_4]_2[Pt_{15}(CO)_{30}]$ μ-stripes exhibit an electrical conductivity of 2.1 $\times 10^{-2}$ S/cm, thus 4 orders of magnitude higher than that of the corresponding raw material (7.7 $\times 10^{-6}$ S/cm). Furthermore we showed that polycristaline Pt sub-micrometric wires can be obtained by thermal annealing. Although this annealing process introduces morphological defects (grains and holes), electrical conductivity (35 S/cm) is found comparable to that of existing Pt or Pt/C composites nanowires (80 S/cm at 20 °C). Furthermore, in order to fabricate functional devices, this technique could lead to the integration of Pt carbonyl clusters with other functional materials such as molecular magnets or organic semiconductors[41,42] and combined with electrochemical systems.[43]

3.2 Towards All-Organic Field-Effect Transistors by Additive Soft Lithography

Unconventional nanofabrication is attractive for organic electronics because of its potential impact in manufacturing low-cost electronics starting from soluble precursors that can be

processed and patterned via sustainable technology.[44] So far, the major endeavor aimed at the development of organicbased devices has been through the design of new materials,[45–47] novel synthetic procedures and purification methods,[48–50] optimized conditions for thin film growth,[51,52] and original methods for nanofabrication.[53,54] In particular, a strong effort was devoted to the technological control of organic semiconductors in transistors.Yet, only a limited number of studies have focused on new approaches for low cost fabrication of electrodes and their integration with the organic materials.[55] Successful examples of unconventional electrode manufacturing include stencil printing of Au nanoparticles,[56] inkjet printing,[57–60] Ag electroless plating followed by microcontact patterning,[61] lamination,[62] microtransfer printing of Ag nanoparticles, metal transfer printing,[63] and soft lithography.[64] Although inkjet printing is probably the most straightforward example of an additive process where both the electrodes and the active layers can be realized on the same platform, the fabrication of the electrodes and the active layers often relies on different processes, specifications, and platforms. Precisely, standard microfabrication approaches consisting of photolithography and/or electron-beam lithography followed by vacuum metallization are generally used for the source and drain definition, while wet methods (spin-coating, layer-bylayer deposition, etc.) are employed for the deposition of the active layer. Clearly, there is a gap in material processing as these major device components are manufactured on different footings and often with severe compatibility limitations. It is therefore important to bridge this technological gap. Towards this direction, this contribution concerns the development of additive manufacturing processes on large areas, which are suitable for patterning both inorganic and organic materials at the micro- and nanoscale. Our methodology also lowers the processing costs by simplifying the fabrication steps.I report here on a simple and versatile way to fabricate micro- and nanoengineered organic field-effect transistors (OFETs) from solution processable materials by additive lithographic techniques. Remarkably, the electrical characteristics reveal that our soft-engineered field-effect transistors perform better than their counterparts

produced with standard microfabrication approaches.[27,65] The OFETs were built in a bottom-gate, bottom-contact architecture. Heavily-doped Si wafers were used both as substrates and gate terminals. The gate dielectrics consisted of thermally grown SiO_2 layers.

As shown in Figure 3.10, the electrodes were fabricated by micromolding-in-capillaries (MIMIC)[39,40] and, for comparison purposes, by drop-casting combined with photolithography. Similarly, the active layers were integrated by drop-casting and by lithographically controlled wetting (LCW),[22] which ensures easy transfer of micro- and nanometric motifs from stamps to solution processable materials. For MIMIC-based fabrication of metallic electrodes (Figure 3.10), a stamp made of poly(dimethylsiloxane) (PDMS) was placed on the dielectric's surface to effectively form microchannels. When the dimethylformamide (DMF) solution of the metal precursor was poured at the open end of the stamp, the liquid filled in the microchannels by capillary action. As a metal precursor we employed the $[NBu_4]^+$ salt of $[Pt_{15}(CO)_{30}]^{2-}$[Pt15(CO)30]2" (**1**). I chose **1** for several reasons: i) it has already been used for the fabrication of submicrometric conductive wires;[66] ii) it can be easily synthesized in water from commercial Pt salts;[67,68] iii) it self-assembles upon crystallization to yield wires organized into 1D, 2D, or 3D structures.[4]

After the complete evaporation of the solvent (typically 24 h in air at room temperature), the stamp was removed and the sample annealed 10 min in air at 250 8C. The annealing process allowed the complete decomposition of the carbonyl groups and thus the formation of 20-nm-thick Pt electrodes. The bottom inset in Figure 3.11 shows typical electrodes obtained by MIMIC. On the other hand, for the fabrication of Pt electrodes by combined photolithography and drop-casting (Figure 3.11), a uniform film of **1** was first cast on Si/SiO2 substrates. The samples were kept 24 h in ambient conditions to allow for complete solvent evaporation and were subsequently annealed at 250 °C in air for 10 min. At this stage, the decomposition of the carbonyl groups took place, resulting in a 90-nm-thick Pt layer. The final steps of electrode patterning involved photolithography with a soft mask and wet-etching by immersion in

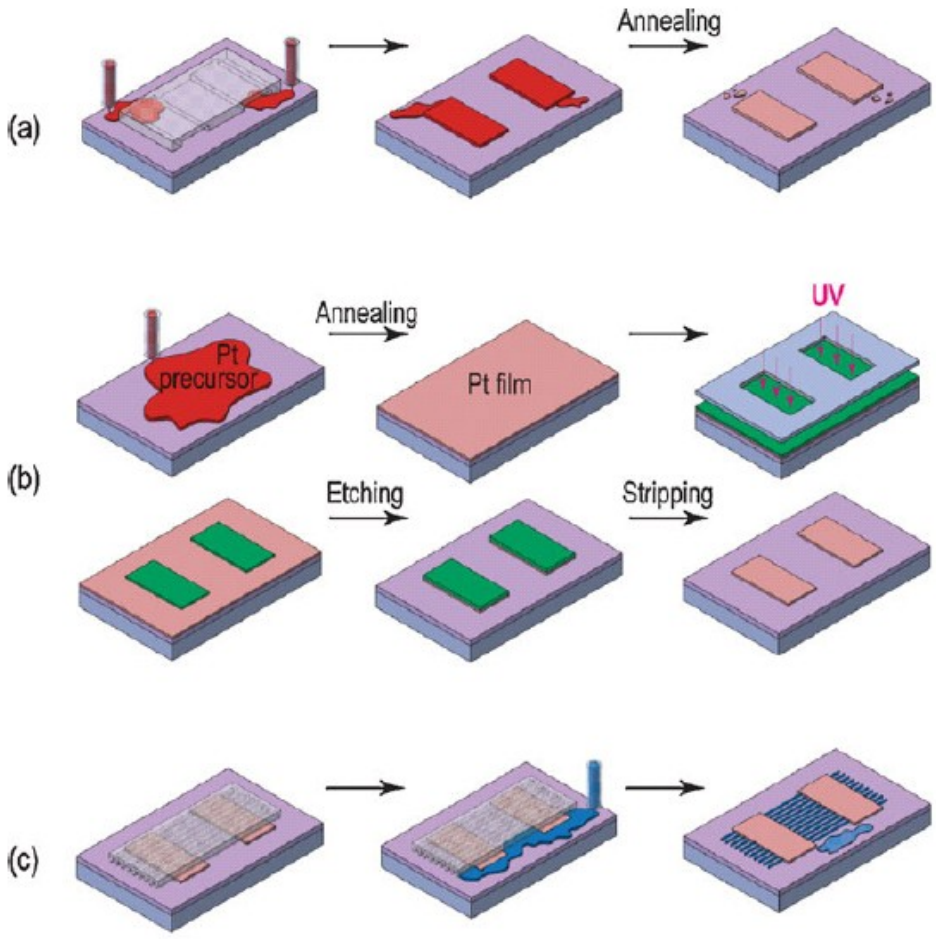

Figure 3.10: Schematic representation of the lithographic techniques used in the present chapter for soft-processed FETs. Here, a solution processable metal precursor is patterned in source and drain electrodes at micrometric scale by MIMIC (a) and by drop-casting combined with softmask photolithography (b). Micro- and nanostructured stripes of the organic semiconductor are defined by LCW (c).

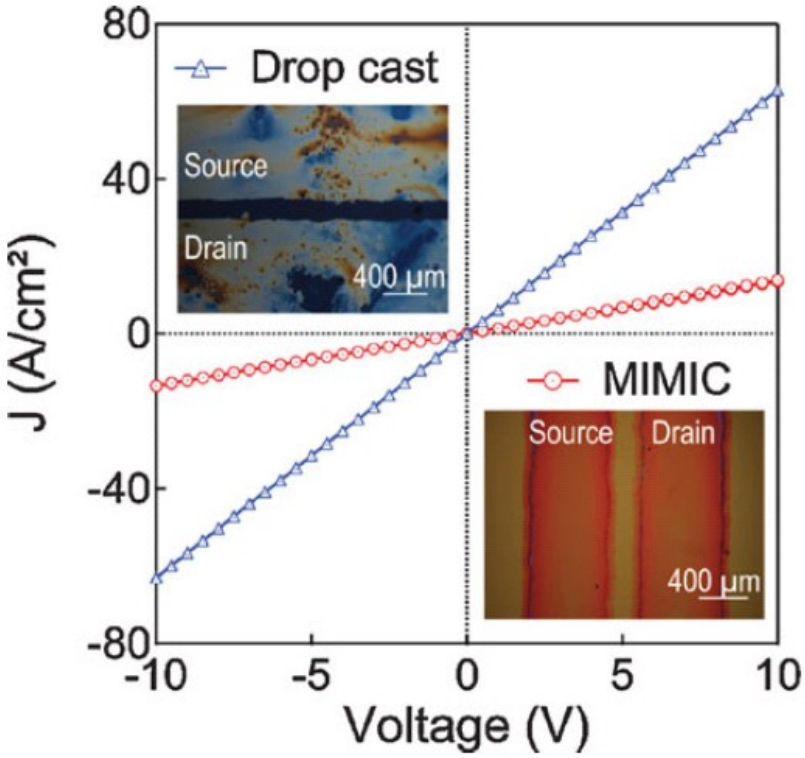

Figure 3.11: Soft lithography provides source and drain electrodes for OFETs. The Pt electrodes are fabricated either by drop-casting (upper inset) or MIMIC (lower inset) from a Pt-carbonyl cluster precursor. Comparison of current density–voltage characteristics for annealed Pt electrodes deposited by drop-casting (blue) and MIMIC (red) routes.

a 10% hydrofluoric acid solution for 3 s. The electrical characterization of the softpatterned Pt electrodes revealed an Ohmic behavior that has been consistently reproduced upon several voltage-sweep cycles. Indeed, the data points of twelve consecutive sweeps fall on top of each other, showing no sign of hysteresis or other electrical deterioration. We found that the electrical 2D resistivity[69] of drop-cast electrodes (blue triangles, ρ =0.05 MΩ per square) is one order of magnitude lower than the resistivity of Pt electrodes fabricated by MIMIC (red circles, ρ =1 MΩ per square). The absolute values of the electrical resistivity are somewhat higher than the ones usually achieved using submicrometric Pt stripes,[66] however small enough[70] when compared to the electrical resistivity of the organic semiconducting layers to enable further employment of these electrodes in electrical devices. The higher electrical resistivity of these OFET electrodes with respect to submicrometric wires stems from the fact that the size of the MIMIC channels used here is a few orders of magnitude larger compared to the characteristic length scales of nucleation. Hence, the lateral diffusivity of molecules is not restricted as in the case of submicrometric channels.[66] In this regime, several domains are generated during the process whose presence reduces the homogeneity of the film after the annealing and causes the rise of the electrical resistivity. This effect is less relevant for dropcast electrodes because their thickness allows electrical conduction through 3D percolation paths, which are significantly less numerous in the thinner electrodes fabricated by MIMIC. Next, I illustrate that OFETs built with MIMIC processed Pt electrodes display better performance compared to those obtained by standard techniques[71] (i.e., transistors with Pd source–drain electrodes processed by hard-mask lithography and electron-beam evaporation). I used thermally grown SiO2 dielectrics as presented in Table 3.1, where also the width (W) and length (L) of the fabricated OFETs are given.

Electrodes	Channel dimensions	Oxide thickness	$R_{sd}[M\Omega cm]$	$\mu_{sat}\,[cm^2V^{-1}s^{-1}]$
Pd standard	$W = 1000\mu m$, $L = 10\mu m$	100 nm	3	1×10^{-4}
Pt drop cast	$W = 1500\mu m$, $L = 200\mu m$	100 nm	21	7×10^{-4}
Pt MIMIC	$W = 5000\mu m$, $L = 200\mu m$	200 nm	5	2×10^{-3}

Table 3.1: Structural (W, L, SiO2 thickness) and electrical (R_{sd}, μ_{sat}) parameters of various drop-cast DH4T FETs.

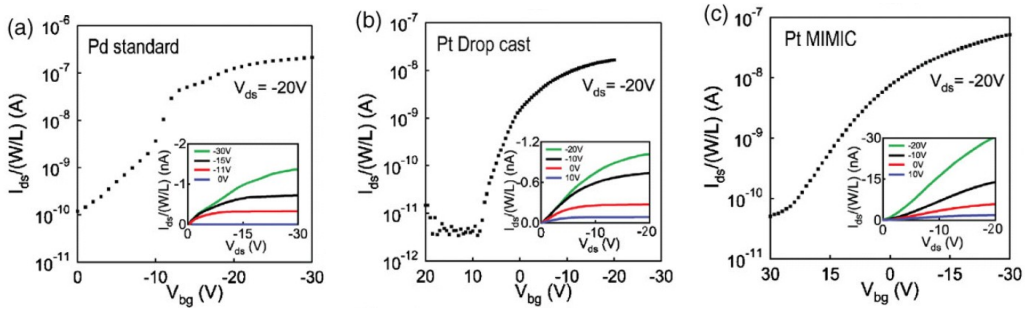

Figure 3.12: Typical transfer characteristics for drop-cast DH4T FETs. a) Standard electrodes manufactured by hard-mask photolithography and electron-beam evaporation of Pd. b) Pt electrodes manufactured by drop-casting and soft-mask photolithography. c) Pt electrodes fabricated by MIMIC. The insets display output curves at various gate voltages.

3.2.1 Additive lithography of semiconductor

To complete the devices, a well-known oligomer, namely dihexylquaterthiophene (DH4T),[72,73] was drop-cast from a 0.4 wt% toluene solution.

The electrical characterization of the p-type DH4T-based FETs is displayed in Figure 3.12 . To simplify the reading of the electrical data, I normalized the transfer current–voltage curves to their respective transistor dimensions. The insets in Figure 3.12 depict output curves collected at various gate biases. Note that whereas our SiO_2 dielectric is rather thick, the devices exhibit well-behaved current saturation. I obtained on-to-off current ratios around 10^3 and saturated mobility, μ_{sat}, in the $10^{-4}cm^2V^{-1}s^{-1}$ range for the drop-cast Pt electrodes (Figure 3.12b), and $\geq 2\cdot10^{-3}cm^2V^{-1}s^{-1}$ for the MIMIC electrodes (Figure 3.12c). Devices with Pt MIMIC source and drain outperform standard devices (Figure 3.12a), which only attained $\mu_{sat}\approx10^{-4}cm^2V^{-1}s^{-1}$, revealing that **1** is effectively useful for electrode fabrication

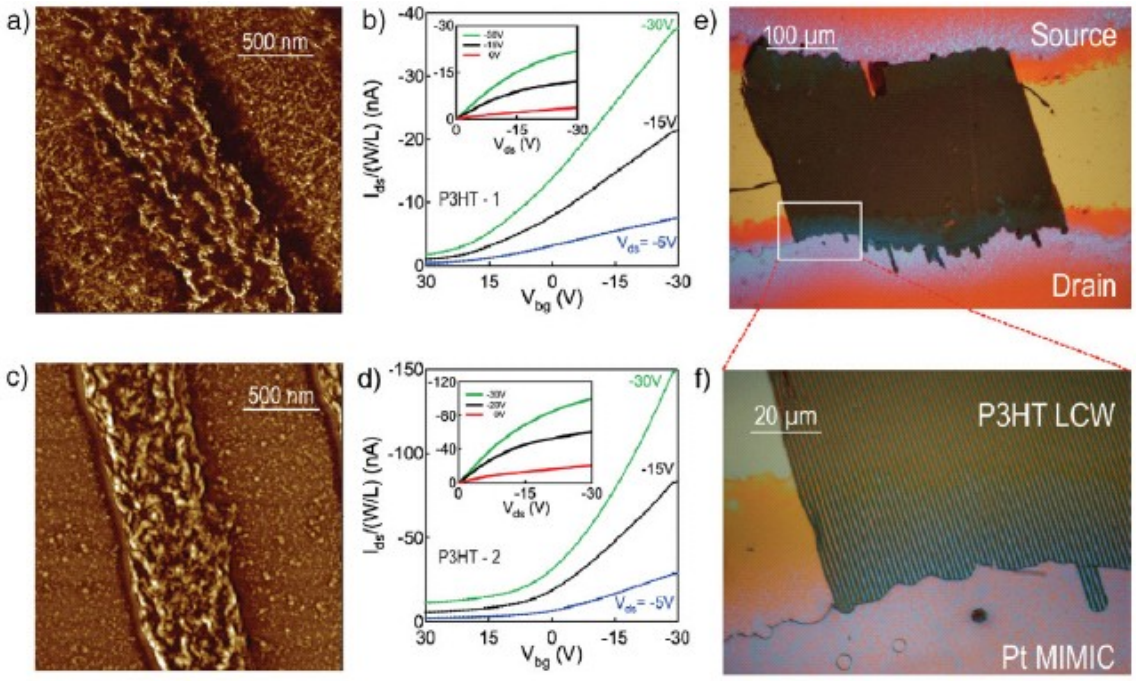

Figure 3.13: AFM phase images and corresponding current–voltage characteristics for standard transistors with P3HT stripes deposited from 0.06 wt% (a, b) and 0.03 wt% (c, d) chloroform solutions by LCW. The insets display the corresponding output curves at various gate voltages. e) Optical picture of an additively soft-patterned transistor, with Pt electrodes defined by MIMIC and P3HT stripes obtained by LCW. We employed a PDMS stamp with 800-nm pitch. f) Detail of the P3HT–Pt interface.

and that MIMIC based patterning ensures relevant improvement in device quality. Two other electrical parameters, presented in Table 3.1together with μ_{sat}, the source–drain resistance (R_{sd}), and the maximum transconductance (g_{m-max}), further corroborate the better performance achieved with the MIMIC Pt electrodes. These results are encouraging to build upon this approach and further focus on the fabrication of OFET channels by additive manufacturing. Thus, I apply the lithographically controlled wetting (LCW) technique (Figure 3.10c) to regio-regular poly(3-hexylthiophene) (P3HT)[74] by using PDMS stamps with 800-nm and 2-mm relief. To assess the quality of the fabrication process, I examined the micro- and nanostructured OFET channels by atomic force microscopy (AFM).

Figure 3.13 shows the AFM phase image inside a typical transistor channel processed by

LCW from a 0.06 wt% chloroform solution. It reveals the presence of both P3HT stripes having 600 nm width and 90 nm height and a 14 nm thick continuous layer under the stripes. The electrical characterization (Figure 3.13b) of such OFETs, fabricated using standard Pd electrodes, revealed a modest saturated mobility of $3 \cdot 10^{-4} cm^2 V^{-1} s^{-1}$, lower than that ($7 \cdot 10^{-4} cm^2 V^{-1} s^{-1}$) measured for drop-cast P3HT transistors. I have subsequently reduced the solution concentration to 0.03wt% with the goal of obtaining isolated P3HT stripes. Although in this second series of experiments a 2-nm-thick P3HT film remains underneath the stripes, as shown in Figure 3.13c, the surface morphology is different (smooth and untextured) compared to the previous case. An illustrative example of current–voltage characteristics of transistors built with diluted chloroform solutions is given in Figure 3.13d. Interestingly, while the dimensions of the P3HT stripes are essentially unchanged, the devices attain $\mu_{sat} \approx 2 \cdot 10^{-3} cm^2 V^{-1} s^{-1}$, one order of magnitude higher than that observed for OFETs processed from concentrated solutions. Finally, in order to make more quantitative results, I employed PDMS molds with 2-μm-width relief. The LCW process applied for 0.03wt% P3HT solutions in chloroform resulted in stripes of 1.6 μm width and 1 μm height (Figure).

In this case, it has been successfully verified that LCW-processed P3HT outperforms drop-cast P3HT in standard FETs. Figure 3.14 summarizes these results. A saturation field-effect mobility $6.5 \cdot 10^{-3} cm^2 V^{-1} s^{-1}$ has been calculated for the multiple-wire devices (top panels), slightly enhanced with respect to msat obtained for FETs processed with the 800-nm-pitch mold. Aligning the P3HT stripes perpendicular to the electric field direction, μ_{sat} falls by several orders of magnitude. Altogether, these results recommend LCW as a suitable technique for high performance P3HT-based FETs in comparison with drop-casting or inkjet methods. The relationship between morphology and charge transport in P3HT-based FETs has been addressed by Surin et al.[75] These authors reported that highly ordered structures offer the best electrical responses. There is no evident sign of cristallinity within the samples made with LCW or MIMIC, this could explain the lower mobilities observed in our transistors

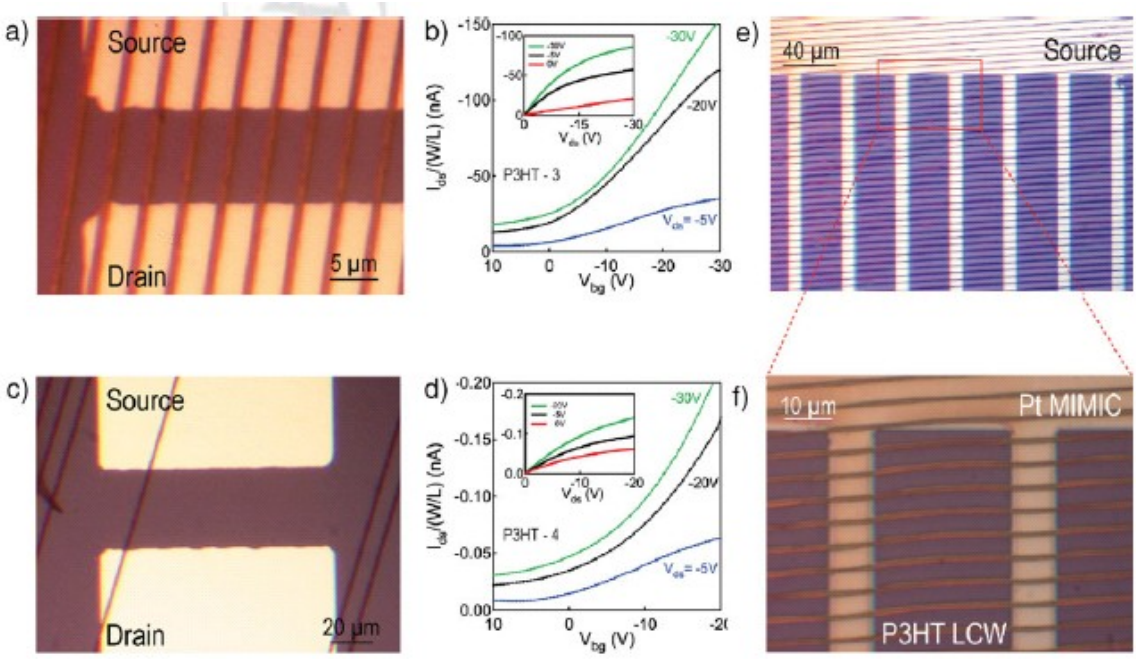

Figure 3.14: Optical images and corresponding current–voltage characteristics for standard transistors with multiple (a, b) and single (c, d) P3HT stripes deposited from 0.03 wt% chloroform solutions by LCW. The insets display the corresponding output curves at various gate voltages. e) Optical picture of an additively soft-patterned transistor, with Pt electrodes defined by MIMIC and P3HT stripes obtained by LCW. We employed a PDMS stamp with 2-mm pitch. f) Detail of the transistor channel close to one of the Pt MIMIC electrodes.

with respect to state-of-the-art performance. Nevertheless, our findings show that homogeneous P3HT films render a poorer mobility with respect to the patterned ones. Given the more than ten-fold increase in mobility and the reduction of R_{sd} upon extinguishing the underlying film, it's possible to infer that the increased internal order of P3HT stripes with respect to that of the homogeneous films is highly beneficial for the charge transport. Besides being efficient, soft lithography is most importantly compatible with both the definition of electrodes and the patterning of organic semiconductors. Fig.3.13e,f and fig 3.14e,f illustrate optical pictures of P3HT-based FETs with a structured channel fabricated by LCW and Pt electrodes obtained by MIMIC. In summary, we have demonstrated the concept and application of an additive soft lithography process that allows OFET fabrication within the same platform using solutionprocessable materials. This route can greatly reduce the processing cost and complexity, therefore opening a promising path towards large-area circuitry. While DH4T-based devices fabricated with Pt source and drain electrodes obtained by MIMIC outperform those having standard Pd contacts, electrical measurements also revealed the enhanced performance of P3HT transistors with LCW-designed channels. Whereas we used well-known organic semiconductors such as DH4T and P3HT that we consider representative p-type materials, this process can be extended to many other soluble molecular materials.

Chapter 4

Self-organization induced by capillary flow

In this chapter a study on the self-organization of nanostructures subjected to capillary forces from a water solution or suspension will be presented. In section 4.1, the alignment of carbon nanotubes (CNTs) from water suspensions under the effect of capillary forces, to form continuous lines of interconnected nanotubes will be discussed. The model, based on the solution of the Fokker Planck partial differential equation, supports the experimental results by MIMIC and LCW patterning of CNT/SDS suspensions. The dynamics of the flow can be accounted by means of capillary forces dominant at the microscale. The probability of alignment of carbon nanotubes vs flow is discussed. In section 4.2, a colloidal system made of polystyrene nanospheres will be exploited to fabricate ordered 3D titanium oxide structures with hierarchical porosity. A novel route to obtain close packed arrays, by means of a co-deposition with titanium oxide precursor, will be presented. The evolution of the correlation function across the consecutive steps of the process, i.e. the nanospheres assemblies and the inverse structures after calcination, is evaluated.

4.1 Fluidic Deposition of Aligned Carbon Nanotubes Conductive Lines

Single Walled Carbon Nanotubes (SWCNTs) have been widely studied for their unique electronic properties. Their high charge mobility together with the capability to sustain a large current density make them attractive as charge transport material in nanoscale and quantum devices, electronic emitters, and as building blocks for circuit interconnections.[76,77] Field-effect transistors, made of individual,[78] or random network[79] of SWCNTs have been demonstrated. Further devices include light-emitting transistors,[80] sensors[81] and transducers for biomolecules.[82] One of the major technological barriers is the lack of a scalable technology for the fabrication of SWCNTs functional structures with a spatial control. Different approaches have been proposed to grow nanotubes by Chemical Vapour Deposition (CVD) directly on surfaces previously seeded or patterned with the metal catalyst. Preferential direction of growth between the electrodes of a device, e.g. vertically (so called forests),[83] or horizontal alignment on the surface, can be induced by gas flow,[84,85] by an electric field,[86] or by careful drawing webs from vertical forests.[87] To increase the unidirectional order of CNTs, as grown, on silicon surface, new methods have been suggested involving selective laser ablation, burning single-walled nanotubes along the light polarization plane.[88] All these approaches yield good results, however they require complex instrumentation or pre-patterning of the catalyst on the substrates,[89] moreover they are restricted to a limited number of substrates. Other systems, involving liquid suspensions of CNTs, are based on pre-patterned surfaces by standard lithographic process and exploit hydrophobic/hydrophilic interaction to control CNT adsorption,[90–92] or localized electrophoretic deposition.[93] Recently, soft-lithography and dip-coating[94] have been applied for patterning CNTs. In particular dry microcontact printing[95] or electrical grid assisted deposition[96] have been used to fabricate stripes of nanotubes with micrometer width. Inside the printed stripes, however, the CNTs

are randomly oriented. Quasi-3D networks of CNTs have been patterned using a template approach with water-dispersed colloidal beads carrying CNTs at their surface.[97] These CNTs membranes exhibit a conductivity on the order of a few hundreds S/cm, viz. comparable to that of bucky paper. This implies that transport anisotropy is absent across large lengthscales and the system behaves effectively as a 3D conductor. In this work we present the fabrication of sub-micrometer stripes and lines made of bundles or anisotropically aligned individual CNTs. The deposition methods used are Lithographically Controlled Wetting (LCW) and Micro Inject Molding In Capillaries (MIMIC) directly applied to a water suspension of single walled CNTs. A detailed description of these techniques is reported in A purified CNTs material, whose purity was assessed by Raman[98] and Scanning Electron Microscopy, was suspended at different concentrations (typically 0.1 g/l for LCW and 1 g/l for MIMIC) in water solutions of Sodium Dodecyl Sulphate (SDS) (0.1% w/w for LCW and 1% w/w for MIMIC).

Lithographically Controlled Wetting

Here I used a stamp made of polycarbonate, featuring parallel lines with 1.45 μm periodicity and 200 nm height. It was placed on the liquid thin film obtained by drop casting 10 μl suspension of CNTs in SDS on a freshly cleaved mica surface. Capillary forces pin the solution under the protrusions giving rise to menisci. The positive replica of the stamp is obtained as the solvent completely evaporates. The capillary forces act also on the nanotubes, keeping them under the protrusion during the solution shrinking. When the solvent is completely shrunk (at room temperature about 24h), the stamp is removed and the sample investigated by intermittent-contact Atomic Force Microscopy (AFM).

In the water suspension a negatively charged shell of SDS molecules surrounds the CNTs.[79] Thus, when the solution is cast on to the negatively charged mica surface, the electrostatic repulsion between SDS shell around the CNT and the substrate depletes the aggregation as

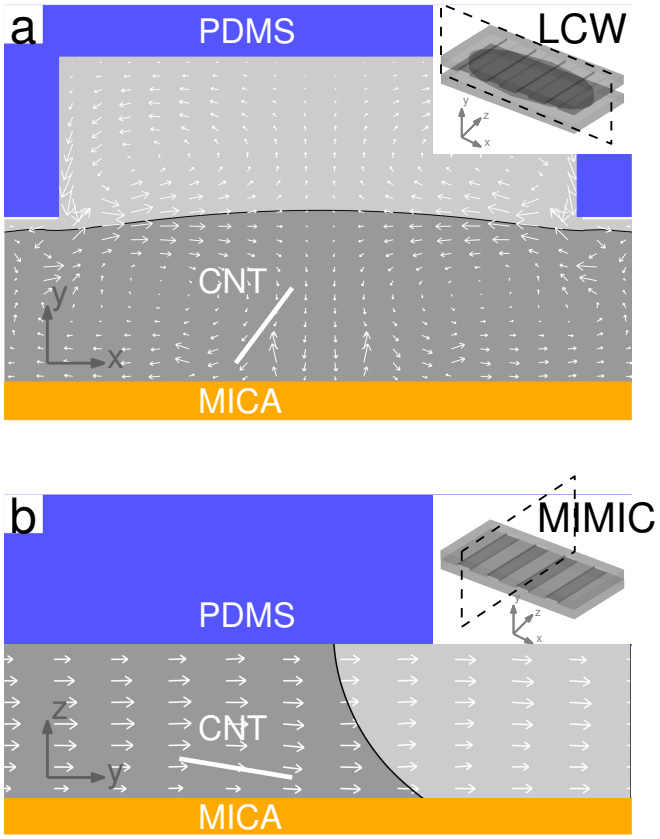

Figure 4.1: White arrows represent the velocity in surface tension flow. In the insets the configuration with the periodic PDMS replica (a) on top of the fluid (LCW); (b) in conformal contact with mica substrates for later infilling (MIMIC).

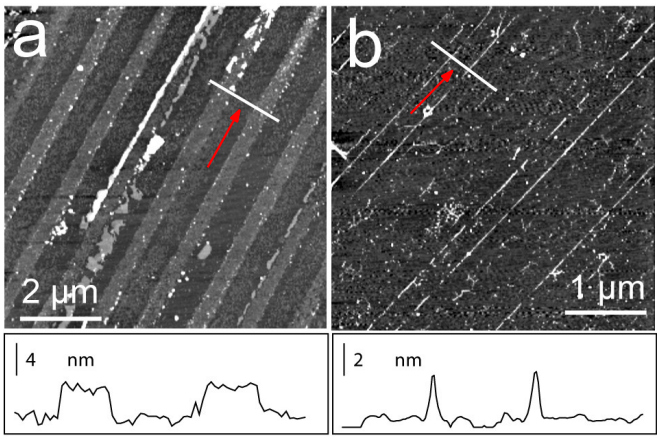

Figure 4.2: AFM image of LCW aligned SWCNTs on mica surface: a) immediately after lithographic stamp removal, b)after washing the stripes with ethanol. Below, the profiles along the lines normal to the patterned SWCNTs are shown.

well as the adsorption of CNT/SDS, which occurs only at the last step of shrinkage. Once this pattern is obtained the surfactant is washed in pure ethanol and individual –or small bundles- of CNTs remain on the surface preserving the charachteristic periodicity of the master. Best experimental conditions were found to be a 0.1 g/l on CNT and 0.1% w/w on SDS. The use of so dilute solution prevents SDS and CNT segregation, furthermore it allows us to use small volumes of solvent for washing. The resulting pattern of individual CNTs, before and after surfactant removal, is shown in Fig.4.2 .

Micro inject molding in capillaries

The second approach that we used is MIMIC, which is a soft-lithographic method suitable for patterning a variety of materials with sub-micrometric resolution. MIMIC allowed us to fabricate patterns of CNTs bundles preferentially aligned and with an enhanced anisotropic conductivity. In MIMIC a polydimethylsiloxane (PDMS) stamp with parallel protrusions is placed in conformal contact with the surface substrate forming closed microchannels. When the suspension containing both CNTs and a suitable surfactant is placed at an open end of the channel, the liquid flows inside driven by capillary forces. After the end of the deposition

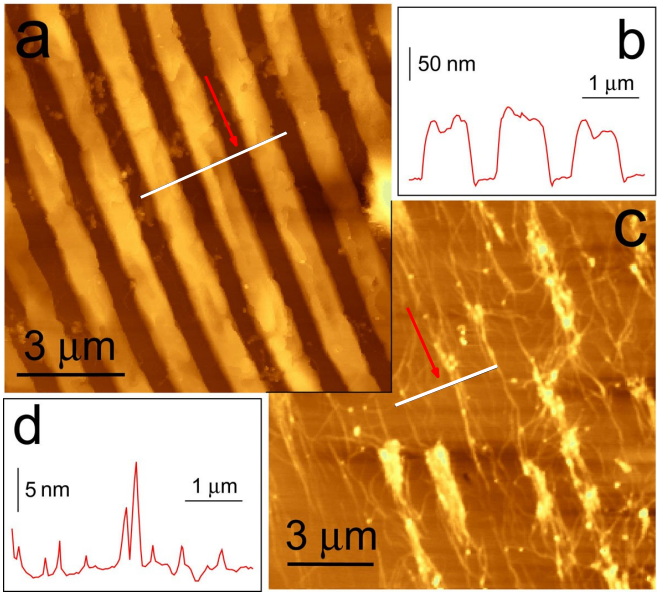

Figure 4.3: a) AFM image of patterned CNT/SDS suspension by MIMIC with b) the corresponding line profile; c) AFM image of aligned bundles of CNTs after washing in ethanol and d) the line profile.

process (typically 48h at room temperature) the stamp is removed and the sample studied by Atomic Force Microscopy (AFM). We used PDMS stamps with parallel protrusions with a pitch of 1.45 µm, height 230 nm and width 400 nm. When the stamp is placed in contact with the glass surface it creates channels about 1 µm wide. To avoid partial filling of the channel, due to the internal hydrodynamic resistance against capillary flow, the hydrophilicity of substrate and stamp was increased by prior oxygen plasma treatment.

An AFM image of pattern obtained by MIMIC is shown in fig 4.3a. The film consists of parallel stripes (thickness 100 nm, width 1µm, spacing 400nm) of CNTs embedded in a SDS matrix. The coverage of the patterned surface is consistent with the 66.7% nominal coverage of the master from which the PDMS replica was obtained.

The nanotubes bundles on the surface remain aligned along the flow direction, although part of the order imposed by the stamp-assisted deposition was lost during rinsing.

The preferential alignment of the CNTs in microfluidics conditions can be ascribed to laminar flow that orients the individual nanotubes along the flux lines throughout the whole

section and length of the channels.[99] Laminar flow is studied by means of Reynolds number in a model with boundary conditions consistent with our experimental setup.. Reynolds number relates the energy of moving liquid to the energy dissipated by the interaction with the channel walls: $\mathrm{Re} = \rho U^2 V/\mu US = \rho UL/\mu$, where μ is the viscosity, ρ the density and U average flux speed. The ratio between volume V and the surface S of the channel wall defines a characteristics length scale ξ, viz. the thickness of the fluid lamina. In our case, for a rectangular channel 1 mm length, 1μm width and 200nm height, ξ turns out to be ≈140 nm[100] We approximate the density and viscosity of the patterned solution (SWNT/SDS) to 0.998 g/cm^3 (as a weighted mean on volume of suspension) and 0.01g/cm·s respectively. The calculated velocity in the centre of the channel, in our experimental layout turns out to be 5m/s, leading to Re≤1.[101,102] As a comparison, the measured fluid velocity in micro-channels filled with more viscous fluids, like polyurethane or silicon oil, is on the order of 0.1 cm/s, corresponding to Re <<13,4. As ξ is few times smaller than the length of the nanotube, but larger than its diameter, the nanotubes will tumble and deform in the laminar flow until they are aligned. Our finite element modeling of the velocity profile along the channel connected to the reservoir suggests that the laminar flow extends from the reservoir to inside the channel during the infilling driven by capillary pressure. Due to the high aspect ratio of the CNTs and the geometrical dimension of the channel only the CNTs that are oriented by flow along the channels, else whose length is much shorter than 800nm, can flow inside the MIMIC channels. The probability of alignment of CNTs along the velocity field u, P(u), is calculated from fem discretization of the Fokker-Planck equation (quadratic closure approximation)[11] and is summarized in fig. 4.4.

The evolution of the alignment in our experimental layout is calculated from continuum equations using a commercial finite element solver (COMSOL MULTIPHYSICS, Lund Sweden). First, we obtained the fluid velocity and local concentration by solving coupled Navier-Stokes and Hamilton-Jacobi equations, which describe momentum balance and liquid-gas

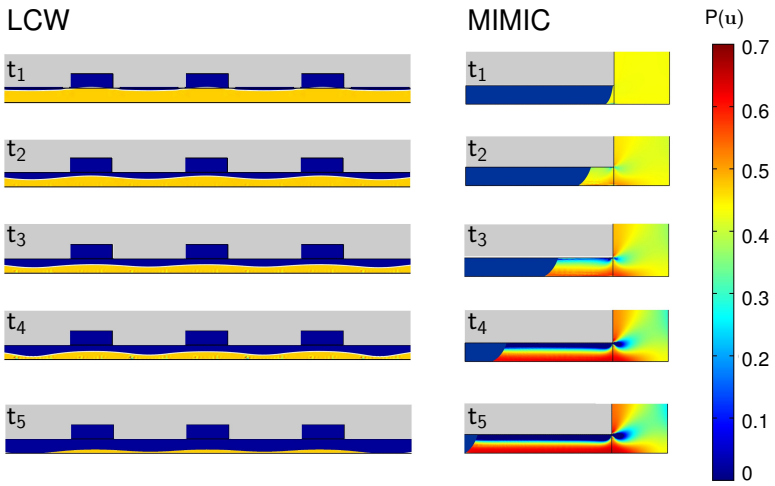

Figure 4.4: Evolution of the probability density function P(u) during the deposition of carbon nanotubes suspension in a) LCW, b) MIMIC. In gray the PDMS replica. The characteristic geometry and velocity field are reported in Fig. 4.1. The probability of aligning the carbon nanotubes along the mentioned flow vectors is then calculated from initial isotropic orientation and appears to vary at the initial stages more effectively for the MIMIC process. In LCW the liquid flows laterally on the hydrophilic mica, during evaporation of the solvent. The PDMS displacement in LCW and deformation is not considered in the present calculation. Time values (s): a) $t_{1...5}$ (s) [5e-6, 3e-5, 6e-5, 1.2e-4, 2.5e-4], b) $t_{1...5}$ (s) [5e-9, 5e-8, 1.5e-7, 4e-7, 5.7e-7]

interface propagation respectively[103] (∂_x indicate partial derivatives with respect to index variable x).

$$\rho\partial_t\mathbf{u} + \rho\mathbf{u}\cdot\nabla\mathbf{u} - \nabla\cdot(\mu(\nabla\mathbf{u} + \nabla\mathbf{u}^{\mathrm{T}})) + \nabla p = \sigma(\mathbf{I} - (\mathbf{nn}^{\mathbf{T}}))\delta + \rho\mathbf{g} \tag{4.1}$$

$$\partial_t\phi + \nabla\cdot(\phi\mathbf{u}) = 0 \tag{4.2}$$

where $\mathbf{u}$ is the velocity field of the fluid, $\mathbf{n}$ the vector normal to the interface, $\mathbf{I}$ the identity tensor, σ the surface tension coefficient of liquid phase, ρ the fluid density, p the pressure, η the fluid viscosity, δ a Kroneker delta function to identify the interface. The tranpose operator is written with superscript $^{\mathbf{T}}$. ϕ is a continuous higher-dimension function whose iso-levels provide the coordinates of interface. This function gives higher resolution for topological changes in the evolving front. The evolution of the air-liquid interface during infilling of the hydrophilic (plasma-treated) PDMS microchannel is calculated solving simultaneously equations 4.1 and 4.2. We did not consider the disjoining pressure in Navier Stokes equation, although may be a dominant effect in short distances close to the PDMS walls.[104,105] Convection-diffusion equation[106]

$$\partial_t c + \nabla\cdot(-D\nabla c + c\mathbf{u}) = 0 \tag{4.3}$$

allows us to calculate the sodium-dodecyl-sulfate (SDS) local concentration c, moving along with the fluid, having velocity $\mathbf{u}$ and diffusion coefficient D. Surface tension is related to the SDS surfactant concentration by means of the empirical relationship fit on literature data

$$\sigma = 0.0364/\{\exp[-(1.74\cdot(\log(c) - 6.0526)] + 1\} \tag{4.4}$$

where σ is the surface tension coefficient (N/m) and c is the SDS molar concentration. The 2D numerical simulations to obtain the velocity field have been repeated for the in-plane and

longitudinal sections of the microchannels. Since surface tension is the driving force of the process, it is correct to take a realistic approximation of the infilling time deduced from finite element calculation of velocity, where the boundaries are formed by the mica and PDMS interfaces . The simulation suggests a change in the flow streamlines at the liquid-gas interface, during infilling and final solvent evaporation. This behaviour can influence the quality of the pattern by changing the probability of alignining the tube along the channel main axis, although we expect a smaller contribution with respect to the disorder introduced by washing with ethanol. Upon the laminar flow, the carbon nanotubes tend to align along the flow streamlines, with probability dependent on the tube length.[107] This result is consistent with the molecular mechanics picture of the interaction between carbon nanotubes and water[108] We describe the alignment of CNTs as the probability density P(u) of finding the nanotubes oriented along the main direction of velocity in the hydrodynamic force field. P(u) is given by the solution of Fokker-Plank equation with the proper boundary conditions[109]and quadratic closure approximation.[110]

The Fokker Planck equation for the model describing the behaviour of carbon nanotubes can be derived from the full form, given by Doi[111] for long polymer rods:

$$\partial_t P = -\partial_{\mathbf{u}} \{(\mathbf{\Omega} \cdot \mathbf{u} + \mathbf{E} \cdot \mathbf{u})P\} + \partial_{\mathbf{u}} \{D_r [\partial_{\mathbf{u}} P + \partial_{\mathbf{u}} (U_{MF}/kT)]\} \tag{4.5}$$

where P is the probability density function of CNT aligned along direction $\mathbf{u}$, Ω vorticity tensor, $\mathbf{E}$ is the symmetrical part of the velocity gradient,D_r is the rotational diffusivity, U_{MF} is the uniaxial mean-field potential. The rotational diffusivity for carbon nanotubes can be written according to[112]

$$D_r = k_B T(\log(L/d) - 0.8)/(3\pi\eta L^3) \tag{4.6}$$

k_B Boltzmann constant, T temperature, L and d length and diameter of nanotubes, η viscosity of suspension).D_r is significantly dependent on the nanotubes aspect ratio. In the calculation

(eq.4.5) the rotational diffusivity (eq.4.6) is taken to be in the interval between 0.5 and 35 s^{-1}. The resulting simplified FP equation can be written as a conservation law:

$$\partial_t P + \nabla \cdot (\Omega \cdot \mathbf{u} + (\mathbf{E} \cdot \mathbf{u} - \mathbf{u}(\mathbf{u} \cdot \mathbf{E} \cdot \mathbf{u}))P + \nabla \cdot \nabla D_r P = 0 \tag{4.7}$$

$$\Omega \cdot \mathbf{u} = 1/||\mathbf{u}||[-(\partial_x v)u\hat{i} - (\partial_y u)v\hat{j}] \tag{4.8}$$

where u, v, i, j represent velocity components along x and y axis, and their respective unit vectors. The ratio of magnitudes of convective and diffusive terms (rotational Péclet number $= (u^2 + v^2)^{1/2}/D_r$) is the most important parameter to define the orientation distribution, with respect to a referring system oriented along the velocity-streamlines direction. The vorticity terms (($\partial_x v$),($\partial_y u$)) are rescaled by the velocity field modulus ($||\mathbf{u}||$) for numerical stability.

The time evolution of P(u) was evaluated for unit cross section in LCW and unit capillary in MIMIC device. Both techniques experience different probabilities of alignment (fig.4.4b) but the capillary forces are advantaging long range alignment only in the MIMIC process. The calculated probability density of orienting the nanotubes is larger near the hydrophilic mica substrate (Fig. 4b), P(u) spans about 100 nm from the fluidics cell walls, and decays towards the PDMS channel wall. The rotational Péclet number, reaches high values in the advancing meniscus front and near the inlet of the MIMIC device ($Pe_r > 10^5$), whereas in LCW it is significantly lower ($Pe_r \sim 10^3$).

Electrical properties

As peculiar property of oriented CNTs, we investigated the electrical behavior of the patterned CNTs lines. After washing, we evaporated gold electrodes through a contact mask consisting of a TEM square grid with 50 mesh onto the patterned film . The contacts pads are separated by channels 62 μm long and 438 μm wide. The grid was aligned with one side parallel to the alignment direction of the CNTs. The electrical measurements were performed

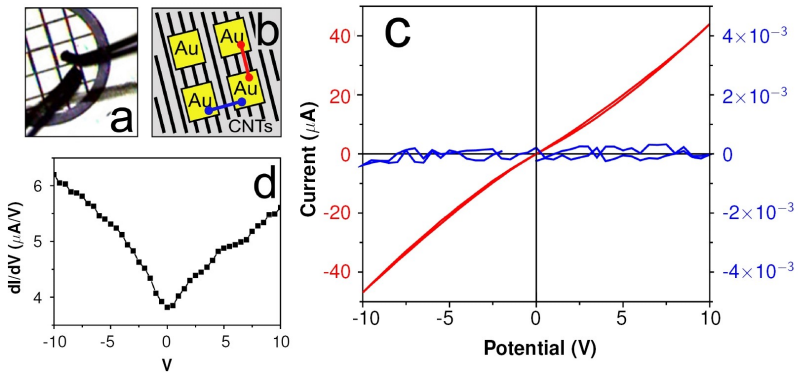

Figure 4.5: Electrical conductivity of the CNT stripes was measured at room temperature with a two-probe method on top gold electrodes, as shown in picture a). The orientation of electrodes with respect to the pattern is depicted in scheme b); c) current vs voltage characteristics measured along the stripes of CNT bundles (red) and perpendicular to tshe patterned lines (blue), by contacting two adjacent electrodes. d) dI/dV curve obtained by numerical differentiation of the I/V curves1 Solid line is a guide to the eye.

measuring I/V curves with voltage/current source meter (Keithley 6430).

The first noticeable evidence is the strong anisotropy of electrical behavior along the aligned patterned stripes of CNT bundles with respect to perpendicular direction. In the latter case, the conductivity was comparable or below the noise level of our instrumental setup. The curves registered along the patterned stripes exhibit non linear response of current vs voltage. The same behavior has been reported in both isolated bundles[113] and thin networks of SWCNTs.[114] In these systems the transport is dominated by the metallic nanotubes, whereas the contribution for semiconductor is negligible at room temperature, even if their contribution at high bias voltage should not be completely ignored. The non linear response of current-voltage is attributed either to a Luttinger liquid behavior[115] or to the presence of interfacial barriers.[116] From I/V measurements the patterned CNTs reveals a conductivity comparable to the literature data. The sheet conductivity is measured to be 16 μS square at 10 V, taking into account the CNT coverage (ϑ=0.38±0.10) obtained from threshold analysis on AFM images. The thickness of the conducting layer is determined by the diameter of the nanotubes laying

on the surface, approximately 5 nm. The residual surfactant captured within the nanotube bundles is less than 10% of the starting suspending material. Considering a perfect pattern with all the lines connected, each line having a width of 50 nm (corresponding to 5 bundles of 10 nm diameter), the value of conductivity found for the single bundle is (26.7±2.5) S/cm at +10V. This is a minimum bound value for the conductivity in two-probe configuration. The main error is introduced by our estimate of the number and diameter of bundles. Another source of error may come from the fact that the charge carriers are injected more effectively in the metallic tubes in contact with the gold electrodes. Both factors contribute to underestimate the experimental conductivity with respect to the real vaslue. In our experimental setup, the contact resistance is high ($\sim$1MΩ).

A last comment relates to the transport perpendicular to the alignment direction. In some AFM images it has been possible to observe the presence of bundles connecting two adjacent parallel lines. It has been reported that crossed CNTs exhibit a resistance four orders of magnitude larger, which will make lateral charge transport limited.[117] Both factors contribute to maintain the one-dimensional character of the current percolation pathways.

Conclusions

Stamp-assisted deposition of CNTs from a water dispersion can be used as an effective approach to fabricate ultra-narrow lines of CNTs with a sizable conductivity. Stamp-assisted deposition takes advantage from the interplay between capillary, surface and intermolecular forces. The methods explored in this work are parallel and can be scaled to large area, they do not require either complex tools or chemical pre-patterning of the surface. Lines of CNTs bundles, a few tens nm wide, can be fabricated by MIMIC as in-plane inter-connectors of electrical contacts. Our measurements confirmed that is possible to align CNTs from a liquid phase along pre-defined directions, preserving the unidirectional electrical contacts. Their conductivity is comparable to that of bucky paper, although the amount of CNTs required

and the coverage is orders of magnitude smaller.

4.2 3D Hierarchical Porous TiO_2 Films from Colloidal Composite Fluidic Deposition

The hierarchical organization of a material into a multimodal architecture of pores with controlled size is attractive because it imparts "smart" properties on the structure, in terms of exposed surface, active sites, rheology, and size selection. This aspect is required for several applications like chromatography, catalysis sensors, photonics, and photovoltaics.[118,119]Interest in the multimodal porosity of titanium oxide, TiO2, has emerged in the last 10 years because of its optical and electronic properties, which have made it one of the most studied materials in photonic and photovoltaic applications. The control of the porosity in films consisting of TiO2 inverse opals represents a crucial advance in the field of photonic band gap materials because it leads to a periodic modulation of the refractive index generating a photonic stop band that does not allow the propagation of light with definite frequencies.[120–122] The substitution of disordered mesoporous TiO2 films with inverse titania opals, in photovoltaic dye-sensitized solar cells (DSSC)[122–125] represented a breakthrough to improve the conversion efficiency of all solid state DSSC up to the highest limit of 11% obtained by Gratzel et al. in liquid electrolyte based devices.[120,121,125–130] As electron transport strictly depends on the network morphology and interconnection of TiO_2 nanoparticles,[126] attention has been focused on the TiO_2 particle network in order to improve its electron transport and, consequently, to increase the efficiency of DSSCs. Geometric confinement controls the diffusive movement and forces the electron transport to take a specific direction. A one-dimensional network has been considered an excellent compromise to achieve the optimum amount of nanoparticle contacts, generating a direct electron transport. In any case, an inverse opal structure combines the regular spatial arrangement of nanoparticles and an extended spe-

cific surface. Templates made of colloidal crystals of polymeric monodisperse beads have been used to generate TiO_2 inverse opals having differently sized (meso and macro) interconnected pores.[126,131] During template removal by thermal treatment, random mesoporosity is produced by the partial sintering of oxide nanoparticles in the shells of the macropores.[132] Controlling mesoporosity in three dimensions represents an innovation for standard templating methods. Specifically for film fabrication, codeposition of ultrafine metal oxide nanoparticles and polymeric templating beads on a substrate was applied to obtain controlled trimodal porosity in SiO_2 films using differently sized templating beads during codeposition.[121,133,134] Up to now, it has only been possible to achieve controlled mesoporosity in TiO2 films by a templating method based on embossing of the titania sol-gel precursor by a poly-(methyl methacrylate) mold.[135] In both previous examples, the size and shape of the resulting structures are univocally correlated to the size and shape of the template and can not be tuned by varying the process parameters. In the recent review articles on templating methods,[119,136] the concept of "structure director" was introduced to describe a situation in which the relationship between template morphology and the resulting porous structure is not univocally established but determined by molecule (mainly surfactants) self-assembling. In this section, I present a colloidal composite acting as a "structure director" for the fabrication of TiO2 films having controlled and geometrically ordered porosity at different length scales. The composite consists of monodisperse polystyrene beads (PS) coated with a titanium oxide precursor named bis(ammonium lactate)titanium dihydroxide (TALH).[123,129,130,137] The multilayered films of ordered TALH/PS composite[127] were deposited in a single step by a fluidic technique called "vertical deposition".[134,138,139] Specifically in these films, annealing[97,129,140] produces an additional controlled porosity at the mesoscale (pore diameter $\sim$ 30 nm), resulting in a chain morphology that we term "mesochain". Mesochains are confined regions regularly placed in the TiO_2 macropore shells and connected only by poorly accessible porosity caused by the partial sintering of the TiO_2 nanocrystals. We show that

a fundamental "structure director" requirement for controlling mesopore distribution in the macropore shells is the absence of reciprocal solubility between the composite components. Highly hydrophilic TALH is orthogonal soluble, at any temperature, to highly hydrophobic polystyrene. By taking advantage of the viscoelastic and relaxation properties of both the polystyrene and the TiO_2 precursor, we developed a process of fabrication leading to a hierarchical pore architecture of the TiO_2 oxide skeleton. In particular, the increase in the Poisson ratio of the TALH coating during the thermal treatment and the critical mass ratio between the PS nanobeads and TALH, which extensively regulates the compliance of the TiO_2 precursor walls, allowed to select the presence and the characteristic thickness of the mesochains in the metal oxide skeleton. We present results about the fabrication of interpenetrated 3D periodic arrays of differently sized pore shells where 12 mesopores are embedded in the macropore shells. The novelty of this process is the demonstration that wellknown materials like polystyrene and bis(ammonium lactate) titanium dihydroxide can be properly combined to form a "structure directing" composite that, under annealing, generates periodic and hierarchically ordered meso-macro pore shells in the TiO_2 structure

4.2.1 Experimental Procedures Colloidal

Bis(ammonium lactate)titanium dihydroxide 50% in water (Aldrich) was used without any further purification (Fig. 4.6). Monodisperse PS, with an average bead size of 340 (5 nm, were prepared by surfactant free emulsion polymerization of 3.5 mL of styrene using 0.47 g of ammonium persulfate as radical initiator in 200 mL of deionized water.29 TALH/PS composite suspension was obtained by mixing 1-20 mg of TALH in 40 mL of deionized water with 17 mg of PS (R) TALH /PS, 0.3 < R < 20) Vertical depositions on microscope glass slides were performed in closed ambient at 55 °C for 12 h (Fig. 4.6). In ordered composite films, the deposition results extended up to ~0.5 cm.

Dry samples were thermally processed in air up to 450 °C with a thermal ramp of 3

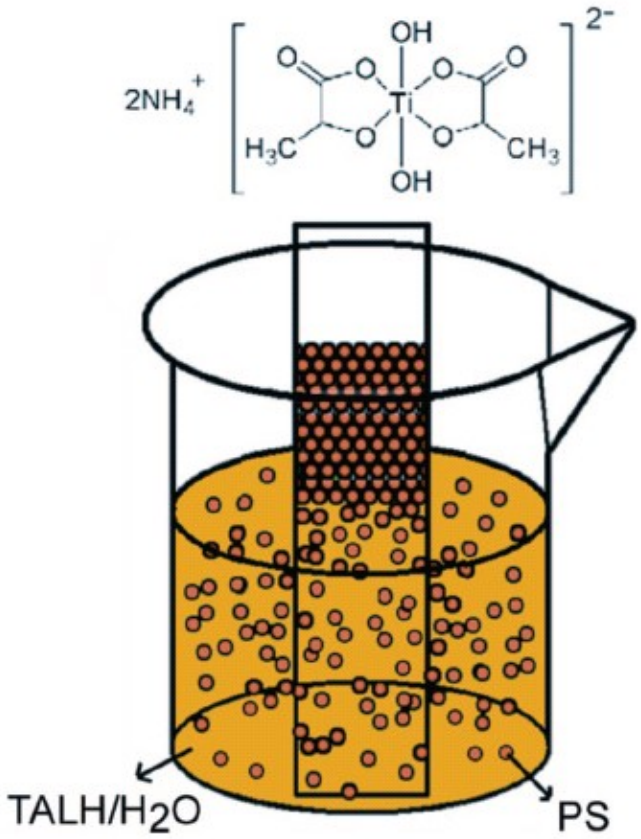

Figure 4.6: Bis(ammonium lactate)titanium dihydroxide (TALH); at the bottom, a scheme of vertical deposition process.

°C/min followed by a 2 h stationary step at 450 °C. Differential scanning calorimetry analysis (DSC) was performed with a STA1500 System (Simultaneous Thermal Analyzer) in an air atmosphere. A temperature ramp of 5 °C/min was used. Raman spectra were collected in back scattering geometry using a Renishaw 1000 micro-Raman instrument equipped with charge coupled device CCD cameras and microscope lense with 50× magnification. The excitation was provided by the 632.8 nm line of a HeNe laser. Because the cutoff edge of the holographic filter does not allow sharp detection of the Eg Raman mode of TiO2 around 145 cm-1, Raman spectra were also collected using a FT-Raman RFS100 Bruker system equipped with a liquid nitrogen cooled Ge detector, an Nd:YAG laser line at 1064 nm was used as an excitation source. In both cases the resolution was 1.0 cm-1 and the accuracy better than 0.5 cm-1. The morphology of the inverse structures of the titanium oxide samples were detected by scanning electron microscopy (SEM). SEM analyses of bead and titanium oxide structures were performed using a Philips XL30 electron microscope operating at 30 kV accelerating voltage. The samples were metallized by sputtering a 3-5 nm thick layer of gold on the surface. Atomic force microscopy (AFM) images were recorded with a stand alone AFM (SMENA NT-MDT Moscow) operating in air, in intermittent contact mode (25 °C with relative humidity 55%). Silicon cantilever (NT-MDT NSG10, with a typical curvature radius of 10 nm tip and a typical resonant frequency 255 KHz) were used. All images are unfiltered. The topographic images were corrected line-by-line for background trend effects by removal of the second-order polynomial fitting.

4.2.2 Concentration ratio leading to ordered 3D structures

A crucial point in the mesochain formation is the thermal treatment of TALH/PS films. We characterized thermally the TALH/PS composites and followed TiO_2 skeleton formation by Raman spectroscopy. Scanning electron microscopy (SEM) and atomic force microscopy (AFM) were used to measure pore size and to detect morphology transformation caused by

TALH/PS composition and by annealing temperature. The thermal behavior of the composite during annealing was followed by differential scanning calorimetric analysis (DSC). The resulting DSC curve is reported in Fig 4.7. Polystyrene thermal processes in air include glass transition (~93 °C), melting (240 °C) and combustion (400-450 °C).[132] From DSC in air of TALH/PS composite it turns out that polystyrene burns at 412 °C. On the other hand, TALH undergoes several endothermic processes in the range 148-240 °C eliminating NH_3 and CO_2 groups, as emphasized in Fig4.7a, and exothermic reactions in the range 280-320 °C, maybe due to the combustion of organic ligands. The effects on sample morphology after TALH endothermic reactions was demonstrated by annealing a set of composite samples at 240 °C and, in turn, rinsing them in tetrahydrofuran (THF) to remove PS. TALH that has been thermally modified at T ≈ 240 °C will be called MTALH. SEM micrograph of a MTALH sample after the solvent washing is shown in Fig. 4.7b. It is evident that thermal treatment at 240 °C is sufficient to modify TALH into a periodic skeleton that remain self-standing after PS removal by solvent. MTALH samples rinsed in THF were analyzed by Raman spectroscopy at λ = 632.8 and 1064 nm. We found that crystalline TiO_2 nanoparticles (anatase phase), smaller than 3 nm, had already formed at 240 °C in air (Fig.4.8, red line)[132,141] The organic TALH residuals in MTALH samples caused an intense luminescence background, exciting at λ =632.8 nm. Exciting at λ = 1064 nm, it was not possible to detect any Raman signal because of the excessive luminescence. The luminescence background almost disappeared at both excitations only after a thermal ramp to 450 °C in air that removed all organics and transformed TALH into the TiO_2 anatase phase (Fig.4.8, black line). Moreover, nanocrystals size increased up to 7 nm because of TiO_2 nanocrystal sintering.[132]

The production of nanostructured TiO_2 film via TALH/ PS composite deposition is based on the coating capability of TALH on PS.[129] We followed the dependence of the final TiO_2 nanostructures on PS coating by TALH that increased until PS surface saturation by varying in the suspension used for the vertical deposition the mass ratio TALH/PS (R) and keeping PS

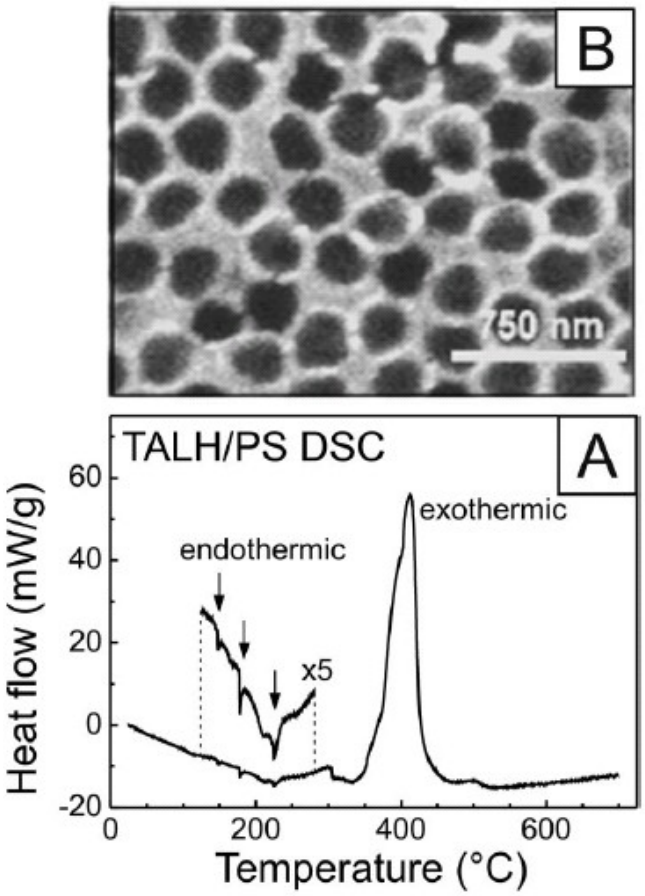

Figure 4.7: (a) Differential scanning calorimetric analysis of a TALH/PS composite: endothermic reactions are reported in a 5× scale; (b) SEM micrograph of R = 2.4 sample after annealing at 240 °C (MTALH) followed by PS removal by tetrahydrofuran.

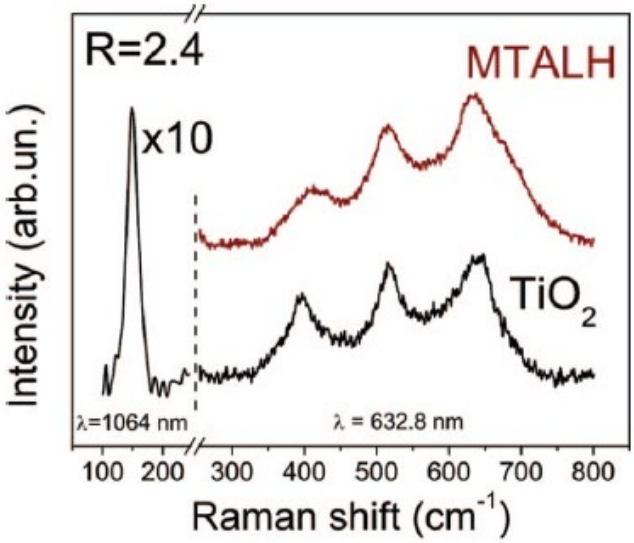

Figure 4.8: RAMAN spectra of R = 2.4 samples. The red line refers to the MTALH sample after PS removal by THF; the black line refers to the TiO_2 sample after 450 °C thermal treatments.

mass, PS diameter, deposition temperature, and water volume constant.[134,138] During the vertical deposition procedure the component concentrations are not constant during film growth, we considered only films deposited at 12 h, assuming that, in these hours, the concentrations are only slightly modified. The progressive close-packing of the nanospheres during vertical deposition is shown in Fig 4.9, where the dynamics of the film's growth was captured by the SEM image.

The polystyrene nanospheres arrangement starts from disordered assemblies and goes through fractal formation toward the maximum hexagonal close packing. The appearance of this configuration is related to the fact that a correct ratio between PS nanospheres and titanium dioxide precursor is reached by liquid phase evaporation. The ordered part of the film was easily recognized by sight since TALH/PS film gave opal-like red reflections. Confirmation of the importance of the TALH concentration for ordering is given in Fig 4.9b where the pair correlation function (PCF) is given for samples with a different ratio R. Using the description given for hard sphere processes,, we saw ordered clustering of PS spheres only

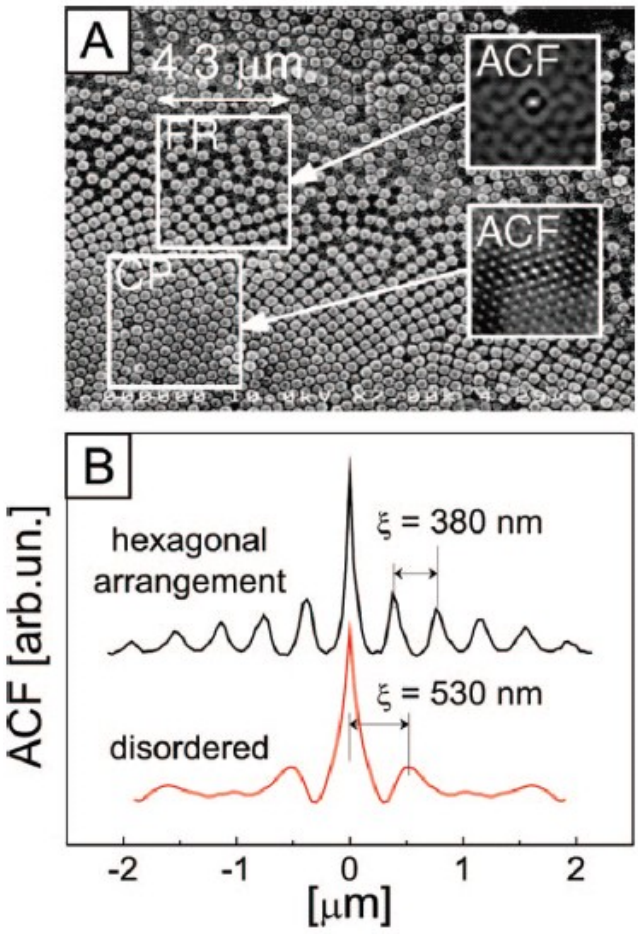

Figure 4.9: (a) SEM image of close packing dynamics, as revealed by nanosphere arrangement during the vertical deposition of TALH/PS, (b) Profiles extracted from 2D autocorrelation maps (ACF) plotted in the inset of two details representing the disordered (FR) and hexagonal close packed (CP) configurations of the sphere array. The positions of the nanospheres in FR are slightly correlated

within small windows of analysis, whereas there was no sound evidence of a long correlation length in the full SEM image, because of various patches present in the outer layer.

TALH/PS films transformed into TiO_2 anatase films after annealing at 450 °C showed well-ordered arrays of macropores whose size was estimated to bee <30% of the PS size by SEM microphotograph. We observed that R strongly influenced macropore array and macropore size. The optimum macropore array was achieved at R=3.5 as confirmed by PCF calculated from the corresponding SEM images as shown in Fig.4.10, where a comparison with a sample obtained from R ≈ 12 is given. This value of R is almost at the limit for ordered macropore array generation. The correlation on sample R = 3.5 reveals a characteristic frequency in ordered arrays at ~350 nm. However, the distance between cavities, also at higher R, can not be less than 300 nm, giving more evidence of the fact that adsorption of TALH is confined on the sphere surface. The order conveyed in the 3D structure can be studied for two superimposed layers directly from the sem image (see Fig.4.10b). The holes resulting from macropore interconnections were not visible for all the samples in the SEM micrographs. Anyway, it was possible to pursue this specific analysis for the optimal ratio between PS and TALH. The coordinates of the characteristic holes left by spheres interconnections have been analyzed with the same algorithm opal, and a characteristic frequency of ~380 nm can be established from PCF peak analysis, both for the first and second layer of the oxide structure.

The pore size trend was collected by varying R (Fig.4.11). The minimum pore size was observed at R=2.4. This value corresponded to an evident discontinuity of the trend. In this case, hexagonal macropore array was conserved and resulted in being regularly bordered by "large mesopores" (~30 nm). These mesopores seem to be regularly concatenated into each single shell. They have a chain appearance that we call "mesochain" morphology.

An explanation of the mesochain morphology is proposed in Fig.4.12. As TALH/PS samples achieved 240 °C, TALH coating, decomposed into TiO_2 nanocrystals, mainly expelling the most hydrophilic groups (NH_3, CO_2) of TALH. We assume that in the range

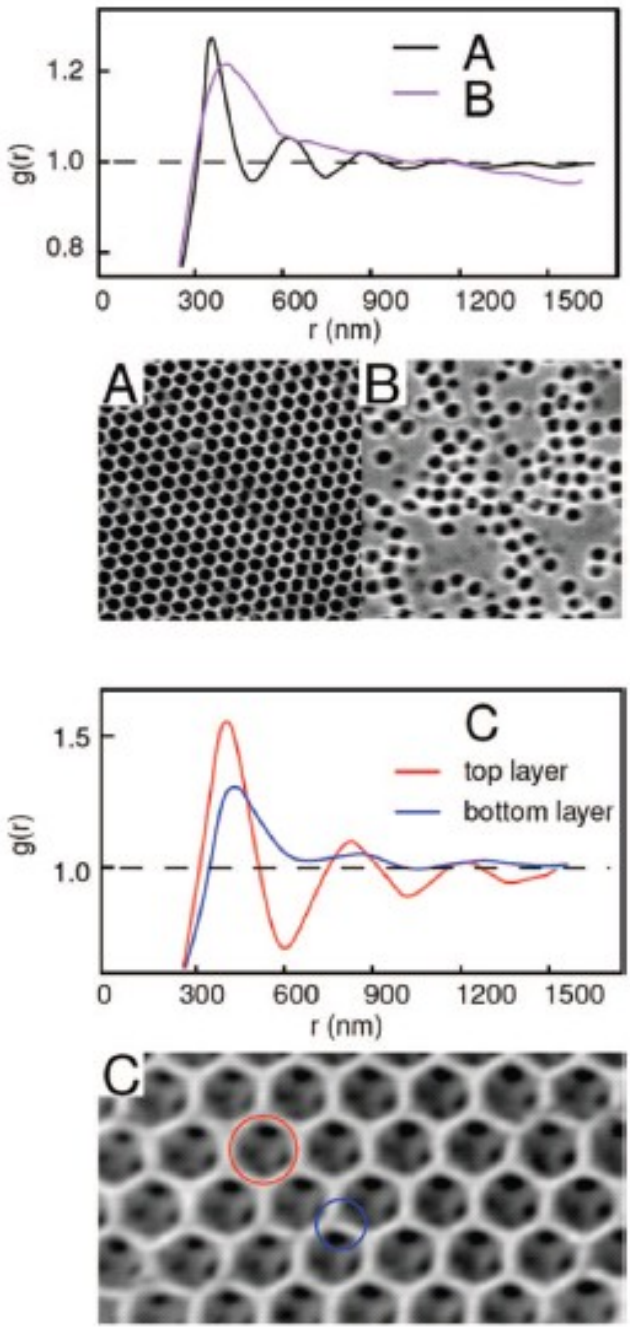

Figure 4.10: Pair correlation function ($g(r)$) for pattern obtained in condition of optimal ratio (R=3.5) between nanospheres and titanium dioxide precursor (A), and at higher concentration of precursor (R=12). In (C), the pair correlation function is calculated among the positions of resulting macropores in the inverse structure. The persisting correlation in the 3D structure is evaluated for two superimposed layers directly from the SEM image, by means of a pattern recognition algorithm. This algorithm recognize the position of the holes in the scaffolds, within the first two layers from the top.

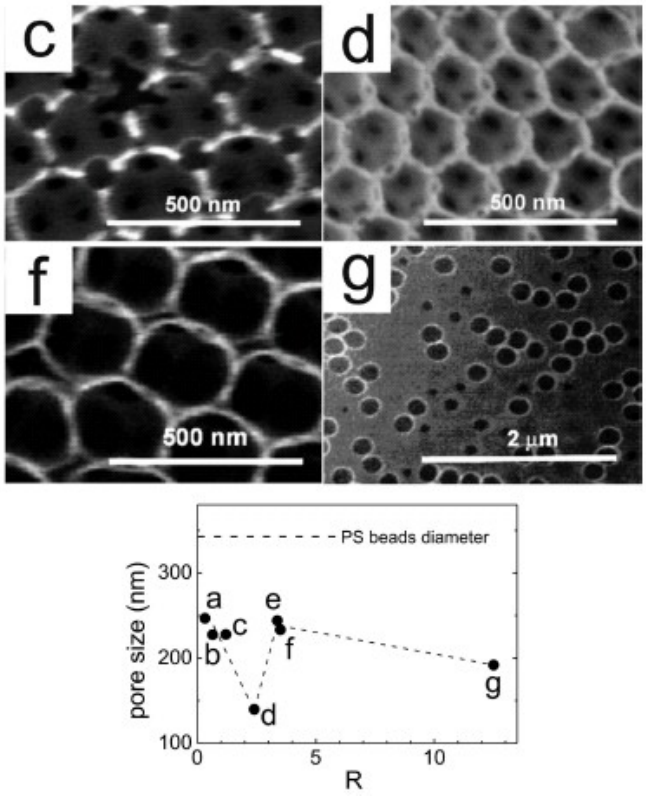

Figure 4.11: Pore size of TiO_2 samples after annealing at 450 °C, coming from different TALH/PS ratios (R). The dotted line represents the diameter of the original PS. The dotted red line highlights the "discontinuity" point in pore diameter. SEM micrographs of the most significant samples are marked with the corresponding letters of the graph.

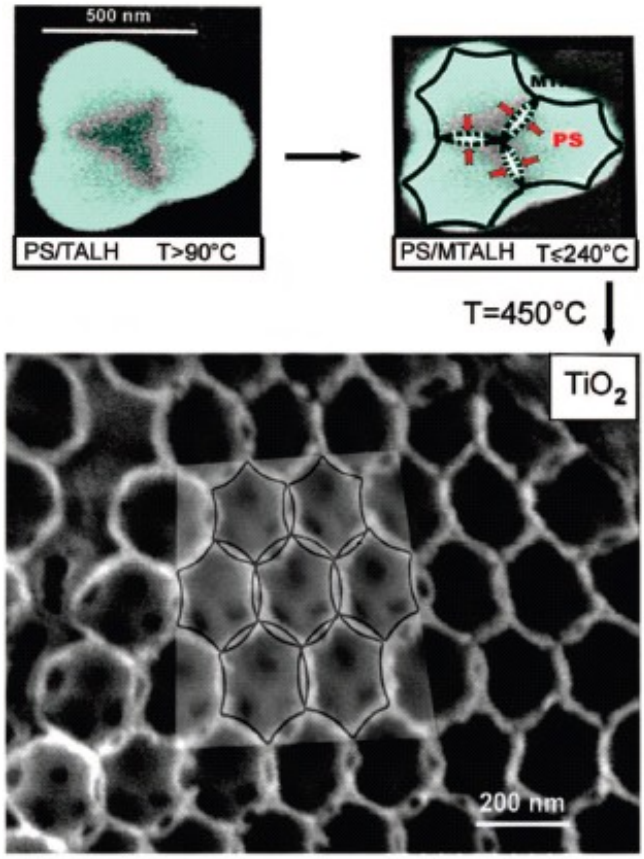

Figure 4.12: Mechanism for the nanochain morphology of $R = 2.4$ samples. It is presented as a SEM micrograph of PS/TALH composite self-assembled on glass substrate at T > 90 °C; a model of polystyrene infiltration trough the MTALH coating at 240 °C and consequent meso-reservoir formations; (3) the resulting mesochain morphology after annealing at 450 °C.

240-400 °C (after polystyrene MP and before polystyrene combustion), liquid polystyrene infilled in the hydrophobic MTALH coating consisting of TiO_2 nanocrystals, amorphous TiO_2, and organic residuals. In particular, liquid polystyrene flowed trough the MTALH and was forced to deposit at the original PS junctions by lateral capillary forces.[142] We assume that polystyrene streams were regulated by TiO_2 nanocrystal sintering and their concentration in the MTALH coatings. MTALH coating by R=2.4 was able to trap liquid polystyrene in sorts of "mesoreservoirs", immersed in the MTALH coating, and regularly placed at the original PS junctions. Because the mesoreservoirs subtract polystyrene from melted PS, the TiO_2 inverse structure, reproduced smaller templating beads, thus determining the decrease in the macropore size. It is significant that some peculiarities also appeared in samples obtained from R=3.5 as shown in the micrograph reported in Fig4.11f. In these samples, the regular macropore shells are transformed into TiO_2 bundles bordering the macropores. The surfaces of THF-treated MTALH and thermal treated TiO_2 samples were compared by AFM operating in non contact mode. We specifically investigated samples obtained from R=2.4. Well-ordered shells made of MTALH are shown. MTALH shells, even after THF washing, seem to be highly dense, maybe because of residual polystyrene.

The morphology of THF-treated MTALH is described by a regular distribution of macro pores spatially organized but non-well-ordered. Thermally treated samples appear more ordered and regular with respect to the MTALH sample, as shown in Fig.4.13a. Macropore shrinkage after the combustion of organic residuals in MTALH is evident when MTALH is compared with TiO_2 films (Fig.4.13b).

On the other hand, after thermal treatment at 450 °C in an air atmosphere, in the AFM images, the resulting TiO_2 sample results perfectly organized in a close packing structure with a macropore size of about 125±7 nm (Fig.4.13b), according to the SEM measurements. Furthermore the TiO_2 nanostructures which form in the places of the original PS junctions form an ordered distribution of nanoclusters whose apparent diameter is ~25 nm (because of

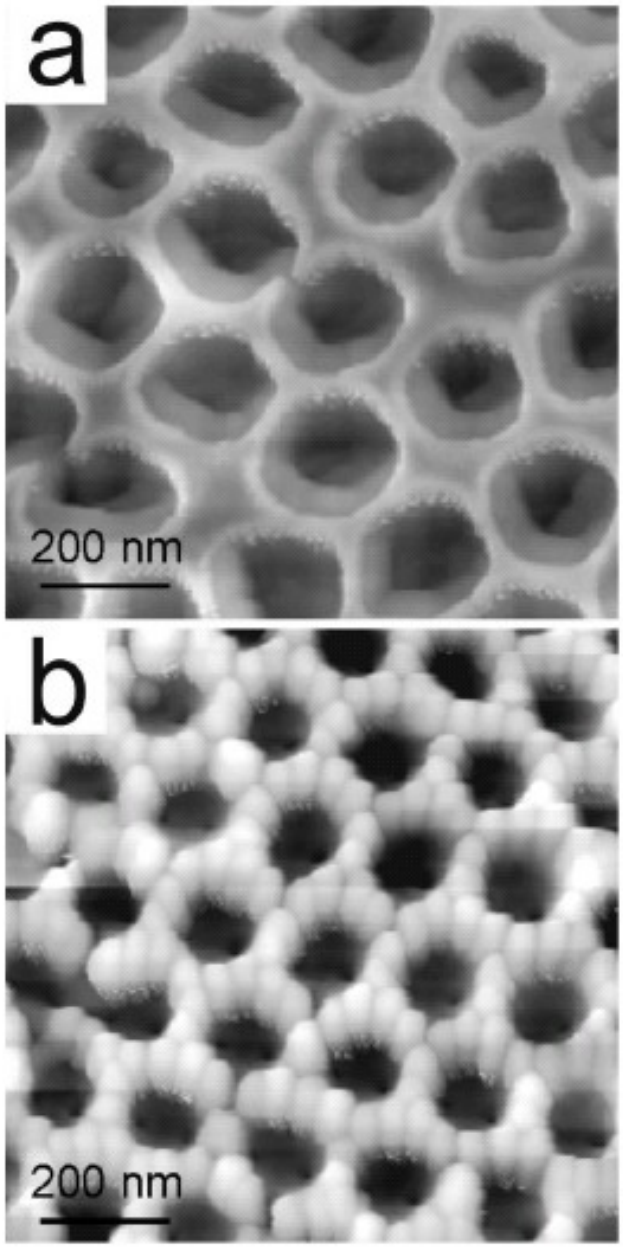

Figure 4.13: AFM operating in non contact mode of the surfaces of a R=2.4 sample in (a) the MTALH form after THF washing and (b) thermal-treated TiO_2 sample.

the tip deconvolution, all the smaller structures always appear to have 20 nm width)

4.2.3 Conclusions

We have shown that PS/TALH colloidal composite can be deposited by a simple fluidic method on a glass substrate. The composite acts as a "structure director" to fabricate 3D nanostructured films of anatase TiO_2 with hierarchical pore distribution and an unusual mesochain morphology. We found that the regular distribution of "large mesopores" strictly depends on a specific composition (TALH/PS ratio = 2.4) of the starting colloidal composite in water. Ordered mesopores are obtained with high reproducibility and they depend on physical characteristics (MP, burning temperature) of both the monodisperse beads (PS) and the TiO_2 precursor (TALH). Under annealing, the resulting nanostructured TALH/PS composite undergoes several transformations until the TiO_2 skeleton "freezes" the morphology induced by thermal treatments. Bimodal porous architecture can be potentially transformed into a bimodal periodic distribution of active materials (i.e., dyes, conductive polymers, nanoparticles, drugs) incrorporated into the TiO_2 skeleton for applications in sensing,[143] photocatalysis,[144,145] and photovoltaic technology.[122,125]

Chapter 5

Amyloid aggregation

In this chapter the investigation of the aggregation of amyloid peptide Aβ40 in microconfined environment will be presented. Confinement is created by means of a microfluidics connected to mesoscopic channels and sealed to a freshly-cleaved mica substrate. The microfluidics mimics the effect of cellular crowding, which delimits the extracellular environment where aggregation takes place in vivo. We focus on the role of the concentration of Aβ40 in the solution. In section 5.1 the role of the Aβ peptide in the pathogenesis of Alzheimer disease is reviewed. . In section 5.2 the experimental results of the microconfined experiment are reported. AFM images are recorded for different peptide initial concentration in the supplied fluid, and a statistical analysis on the aggregate size vs concentration is carried out. In section the experimental value for the diffusion coefficient of the Aβ40 peptide is extracted from the experimental data.

5.1 Alzheimer disease and Aβ peptide

Alzheimer disease (AD) is defined as a neurodegenerative and age related, with increasing impact due to exceeded life expectancy. Histological investigations on the brain tissue of patients affected by AD, reveal the presence of large amounts of neurofibrillary tangles and

neuritic plaques. Plaques consist of extracellular aggregates of amyloid beta peptides (Aβ), derived from the cleavage of the amyloid precursor protein (APP), an extracellular membrane protein. These plaques are linked to inflammation and astrogliosis. Tangles arise from intra-neuronal accumulation of hyperphosphorilated Tau protein, which is involved in binding the microtubules within the cell[146]

Generic risk factors, whose susceptibility accounts for 5% of cases, include mutation of the APP gene on chromosome 21, or in genes encoding for presenilin 1, on chromosome 14. Presenilin leads to the most aggressive forms of AD, with onset below 30 years old.

Apolipoprotein ϵ4 (APOe4), mainly studied in lipid metabolism, is also involved as a risk factor for sporadic AD, at early age. APOe4 is associated with increased total serum cholesterol and probability of arteriosclerosis and coronary disease. Further research is on-going on the inter-relationship between APOe4 allele and the effect of hypertension, cardiac dysfunction and diabetes.

The major constituent of the amyloid is the β peptide which varies in length between 39 and 42 aminoacid units. Other proteins are subject to amyloid insoluble product formation (fibrils and aggregates), among which there are transthyretin, prions and insulin. Apart from forming these self-assembled secondary structures, all these proteins apparently do not have similarities in the primary aminoacidic sequence. Amyloidosys involves peptides binding together by means of electrostatic interactions, leading to aggregates and fibrils.

The β (1-28) peptide is responsible for the α helix soluble parts and the β sheet present in the insoluble aggregate, whereas the 29-40 residues enhance the hydrophobic interactions between monomers in the purely aqueous solution.

The β (1-28) peptide in specific trifluoroethanol is 58% and 47% α helix, with the rest remaining random-coil. The secondary structure of the 29-40 peptide is not significantly altered by pH. Within the pH 4-7, mixtures of β sheet, α helix and random coil coexist in solution and are found to be dependent on time and concentration.

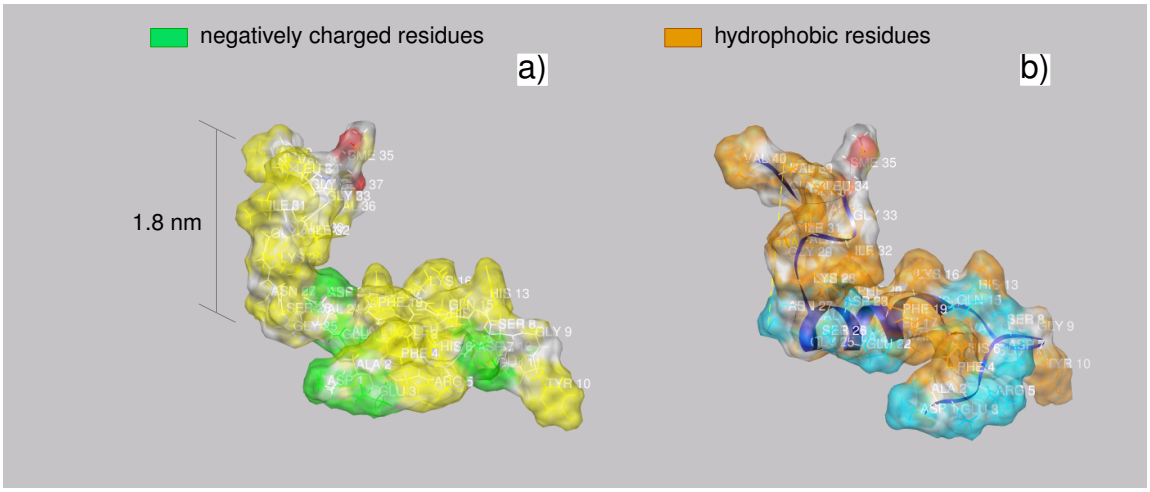

Figure 5.1: The 1BA6 structure of β amyloid peptide reported in the international protein database PDB, a) the negatively charged residues are localized in three regions at the "base" of the peptide (Asp1 and Glu3; Asp7 and Glu11, Glu22 and Asp 23). On the left the vertical dimension of the monomer, if adsorbed flat on mica; b) the hydrophobic domains of the β peptide standing on the upper side of the molecule. Justification for this adsorption model is given by the hydrophobic circular patches, visible at very low concentration (fig.5.11) . These patches achieve the lowest interfacial energy configurations, with respect to water solvent molecules.

Extensive detail on the molecular structures and change in conformation is provided by NMR spectroscopy. However the water dissolved solution comprise a mixture of structures, changing with time, which can not be resolved due to time integration during acquisition.

NMR studies report that the peptide is more likely to interact by means of electrostatic forces than by hydrophobic interactions.

5.1.1 Amyloid cascade

To describe the amyloid cascade hypothesis, we have to consider all the actors which play a role in the degradation pathway of the amyloid precursor proteins. Within the disease symptoms, there is the misfolding of endocellular τ protein. The critical step is considered to be the formation of the insoluble aggregates5.2.

The proteolysis of APP releases the β peptide in monomeric random coil conformation. In

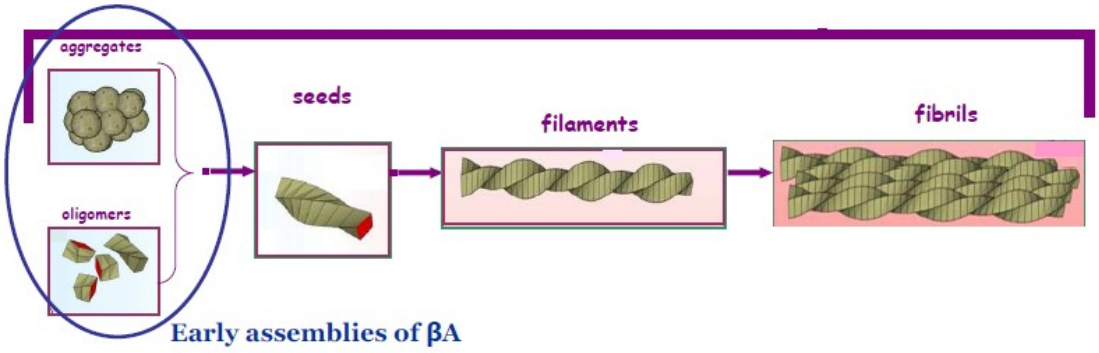

Figure 5.2: Pictorial scheme of the amyloid cascade, from amyloid to fibrils. For efficient diagnosis, effort should focus on the study and detection of the early amyloid assemblies.

cerebrospinal fluid (CSF), the normal concentration of the peptide is in the nanomolar- picomolar range. At these concentrations the formation of amyloid β sheet structures is unlikely, unless in the presence of mediators (glycation, zinc, APOe4) which can promote aggregation aggregation. The critical step for Amyloidosys is considered to be the formation of the insoluble aggregates. Changes in the microenvironment are essentially related to sudden change of pH at the surface or interface. Aβ polymerization can be depleted by specific inhibitors in form of small molecules, which reduce the aggregation rate.

The monomeric form, whether as α-helix, β-strand, or composition of β turns, is non toxic as demonstrated also in vivo. The toxicity may be related to the interconversion of soluble α helical amyloid monomer to oligomeric β sheet structures. The concentration of β amyloid peptide 1-40 has been related to neurotoxicity in vitro. In animal models, Aβ oligomers seem to interact with the fundamental synaptic mechanism such as long term potentiation, which is evaluated as an early clinical response. Cytotoxicity studies have found that both the oligomeric soluble forms of Aβ peptide and the protofibrillary/fibrillary deposits are toxic and may be targets of cure. Fibrils and plaques enhance the oxidative stress mechanism, causing glial and immune response (inflammation). The amount of plaques has been correlated to severity of dementia.

As higher molecular weight aggregates and fibrils are resistant to proteolytic attack, pre-

vention and therapeutic strategies focus on the initial aggregates of β amyloid. Thus, monitoring the early stages of the amyloid cascade is crucial.

Although measurements lack in detail about the effective involvement of oligomeric forms, cognitive improvements reported by patients in Aβ immunization therapy trial, might be due to decrease in soluble oligomeric Aβ.[147] In humans, approximately equal rates of synthesis and turnover (8%) of Aβ per hour is observed in CSF. This rapid turnover indicates that Aβ levels are dynamics and that decreased clearance is probably a major contributor to Aβ buildup in brain with aging.

Specific inhibitors target Aβ production and act on the concentration of Aβ peptide within the brain. These concentration values can be evaluated by specific immunoassays. Results must be interpreted with criteria to discern the equilibrium between the soluble and the insoluble forms, and between the oligomeric assemblies and the total Aβ peptide content. The mechanism by which oligomers act on the membrane resemble the formation of non selective membrane pores (permeabilization) and the generation of receptor-dependent signaling cascades[148]

All these etiologic theories are confirmed from experiments performed on animal models repeatedly. Injection of autologous Aβ oligomers extracted and purified from mice brain, determine the insurgence of long-term memory impairment on healthy rats.

All the in-vitro aggregation experiments reported in literature have been run in bulk solution, or on surface. The confinement has not been addressed directly. Therefore we want to investigate what is the fate of monomers within microfluidic device, which resembles the crowded environment present in vivo.

5.2 Microfluidic experiment for aggregation

We have investigated the self-organization of β-amyloid peptides at solid-liquid interface in confined fluidic environments with mesoscopic length scale. We create a confined environment for the incubation of the peptide solution. The microfluidic device was made of a polydimethylsiloxane (PDMS) stamp attached to a freshly cleaved mica plate (see fig.5.3). The whole system is sealed with PDMS, leaving open outlets to sustain capillary flow. The geometry of the fluidic cell can be described as a main circular channel of 120 μm diameter intersecting perpendicularly an array of side channels whose characteristic section is: width 600 nm and height 180 nm. The volume of each side channel is 0.3 pl, and the total volume of the fluidic cell is 37 nL, to be compared to 1 μl in a drop cast on a mica plate as in standard deposition. The latter approach, albeit widely used, does not allow to control the effects of capillary flow on concentration and deposition rate of the different peptide forms. The Aβ1-40 solution is confined between the negatively charged hydrophilic mica surface and the neutral hydrophobic replica of PDMS.

The cell design has been prototyped with finite element modeling (COMSOL Multiphysics, ver. 3.3a Lund, SE), evaluating flow and concentration profiles in the channels. Navier Stokes equation, corrected with surface tension term to account for the differences between mica and PDMS, provide the local pressure acting in the channels. From the resulting hydrodynamic flow, we calculate the concentration of the solute (to which is assigned a net charge equal to -2 at pH=6.5) in the channels at stationary condition. The sequence in figure 5.3b, shows that the concentration of the peptide in the channel reaches a steady state at the same initial concentration of the infilling solution in about 1 ms, much earlier than the incubation time of our experiment. The model indicates that there is a homogeneous solution at the entrance of the meso channels, with comparable flow and simultaneous infilling time, thus a homogeneous deposition rate on the surface.

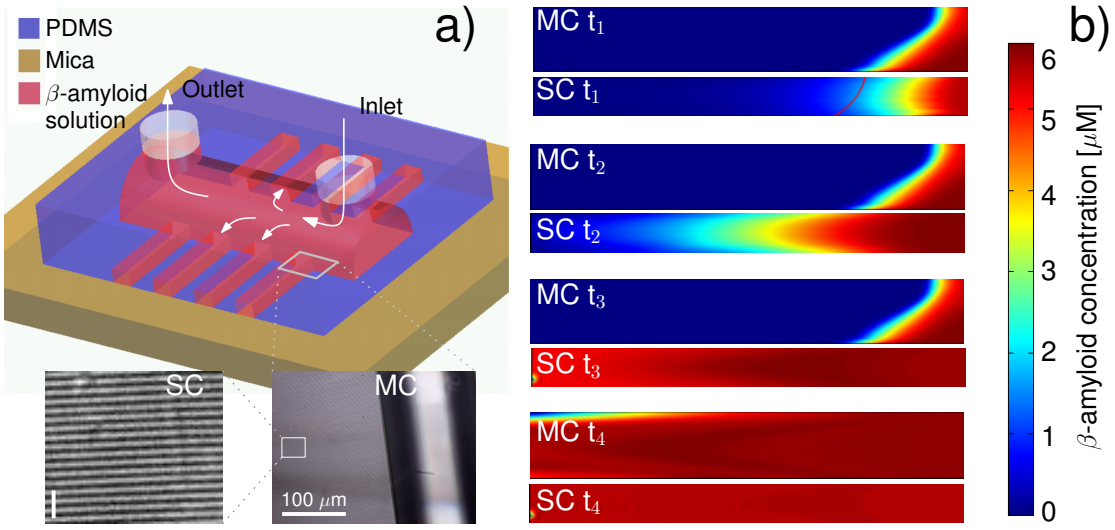

Figure 5.3: a) (top) Schematic drawing (not in scale) of the microfluidics; (bottom) optical micrograph of the the main channel (diameter = $125\mu m$) and mesoscopic channels ($600 \times 180 nm^2$) intersecting the main channel at 90°; vertical ruler is $5\mu m$. b) Sequence of concentration profiles along the channels (top: main channel; bottom: mesoscopic ones) at $t_1 = 6 \cdot 10^{-5}\, s$; $t_2 = 6.05 \cdot 10^{-5}\, s$; $t_3 = 6.1 \cdot 10^{-5}\, s$; $t_4 = 4 \cdot 10^{-4}\, s$

The AFM images in Fig.5.4 show the evolution of the morphology of the aggregates at different initial concentration. At 6 μM the dominant population consists of globular aggregates whose height is 7-9 nm and the projected area 0,04-0,06 μm^2. High Molecular Weight Oligomers (HMWO) with sizes of 3-5 nm height and 100 nm diameter are present as minority population at this concentration, possibly disappearing due to their coalescence into globular aggregates. The number density of HMWO is much lower with respect to the bulk solution. At 4,8 μM, the fraction of large aggregates is considerably smaller and is comparable to the one of HMWO. At concentrations below 4 μM , HMWOs are dominant and the large globular aggregates are absent. Conversely, HMWOs are formed even in very diluted microenvironments (3 and 1,2 μM). These oligomers emerge from, or are embedded in, a thin film of peptides. This suggest oligomers form and coexist with adsorbed peptides in a thin film. The film is discontinuous and exhibits voids, whose mean height is 1-2 nm. At 0,24 μM mostly small oligomers are present. This sequence shows that the larger aggregates are stabilized by

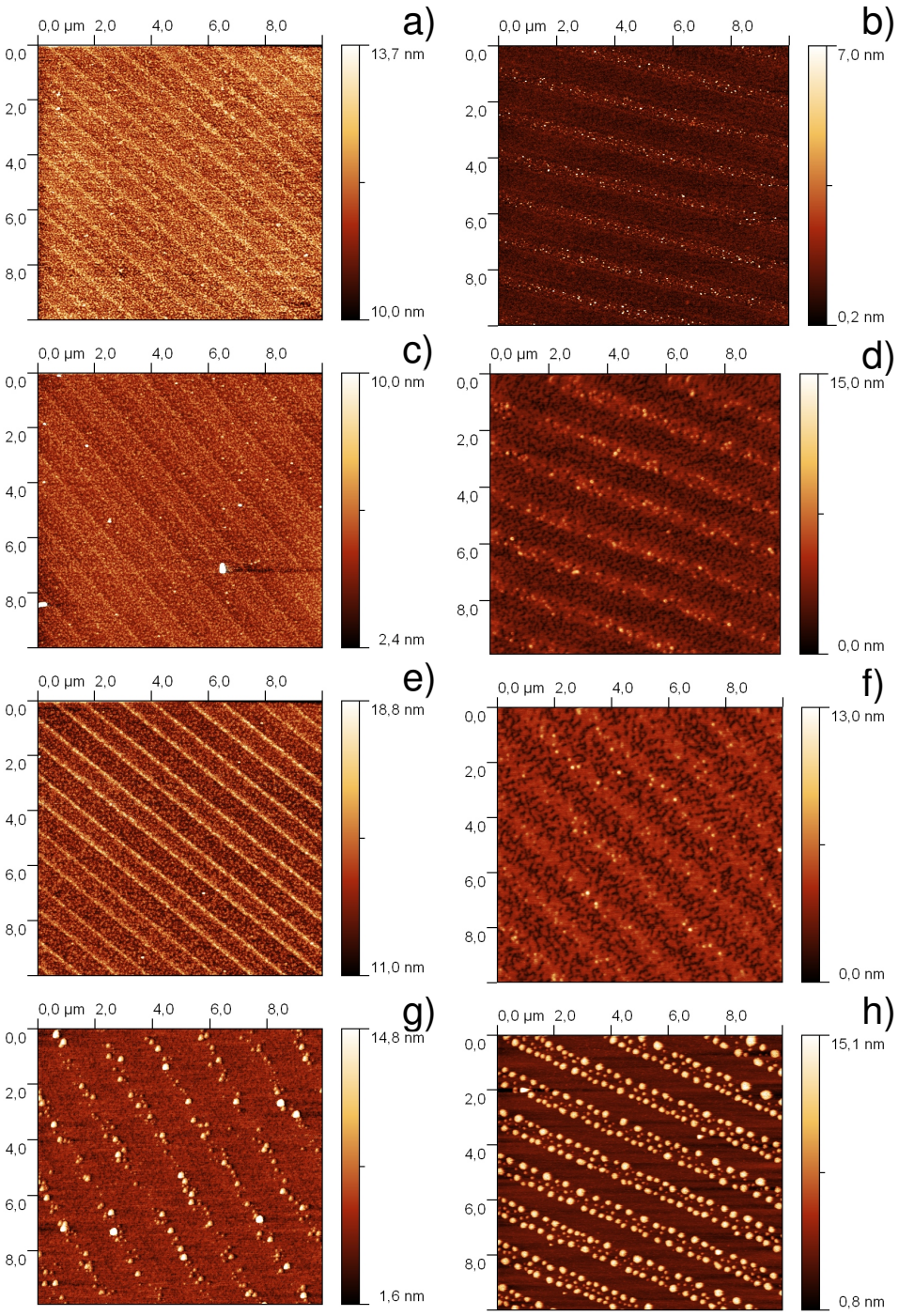

Figure 5.4: AFM images of the amyloid oligomers adsorbed within the mesoscopic channels SC at different initial concentration; a) $0.1\mu M$, b) $0.24\mu M$, c) $0.6\mu M$, d) $1\mu M$, e) $2\mu M$, f) $3\mu M$, g) $4.8\mu M$, h) $6\mu M$

confinement at higher concentration of the peptide, by the onset of a coalescence process at expenses of the small ones.

The evolution of the size distribution (height and lateral size) of the aggregates is quantitatively analyzed in Fig.5.5 and 5.6, to yield information about the populations of aggregates. There is a correlation between the features of the height and lateral size histograms. The decrease of oligomers population with concentration is obvious only at higher concentration. The class of oligomers formed at submicromolar concentration exhibits similar height with the oligomers formed at the concentrations close to $1\mu m$. Nevertheless, the histogram of the diameters shows the absence of globular aggregates at lower concentrations and the formation of small oligomers at submicromolar concentrations. The fact that the height of the oligomers seems to reach a stable value for lower concentrations, while the diameter continues to decrease suggests that the aggregation arises at the surface rather than in solution.

The histograms are fit with a linear combination of gamma distributions ($p[1]\cdot\text{dgamma}(x,k_1,\theta_1)+p[2]\cdot\text{dgamma}(x,k_2,\theta_2)+(1-p[1]-p[2])\cdot\text{dgamma}(x,k_3,\theta_3)$), where $\text{dgamma}(x,k_1,\theta_1)=x^{k-1}\frac{exp(-x/\theta)}{\Gamma(k)\theta^k}$ is the probability density function (pdf) of each gamma distribution. Fitting parameters are populations fractions $p[1,2]$ and some of the distribution parameters. For each fit, we use three functions of the basis set, with four independent parameters at the most. In order to limit the fitting parameters, we start from the lowest concentration, the best fit k,θ found are then fixed, and the fitting iterated to the histograms at higher concentrations adding one gamma pdf function at a time.

Figure 5.7 shows the variation of the four populations as a function of concentration. At submicromolar concentration the majority population is represented by LMWO that rapidly decrease with increasing concentration, disappearing for C0>5 μM. Small oligomers represent a minority population at submicromolar concentration, then they increase above micromolar concentration reaching a plateau and then disappearing at concentration higher than 4-5 μM. HMWO are formed above micromolar concentrations concurrently with the disap-

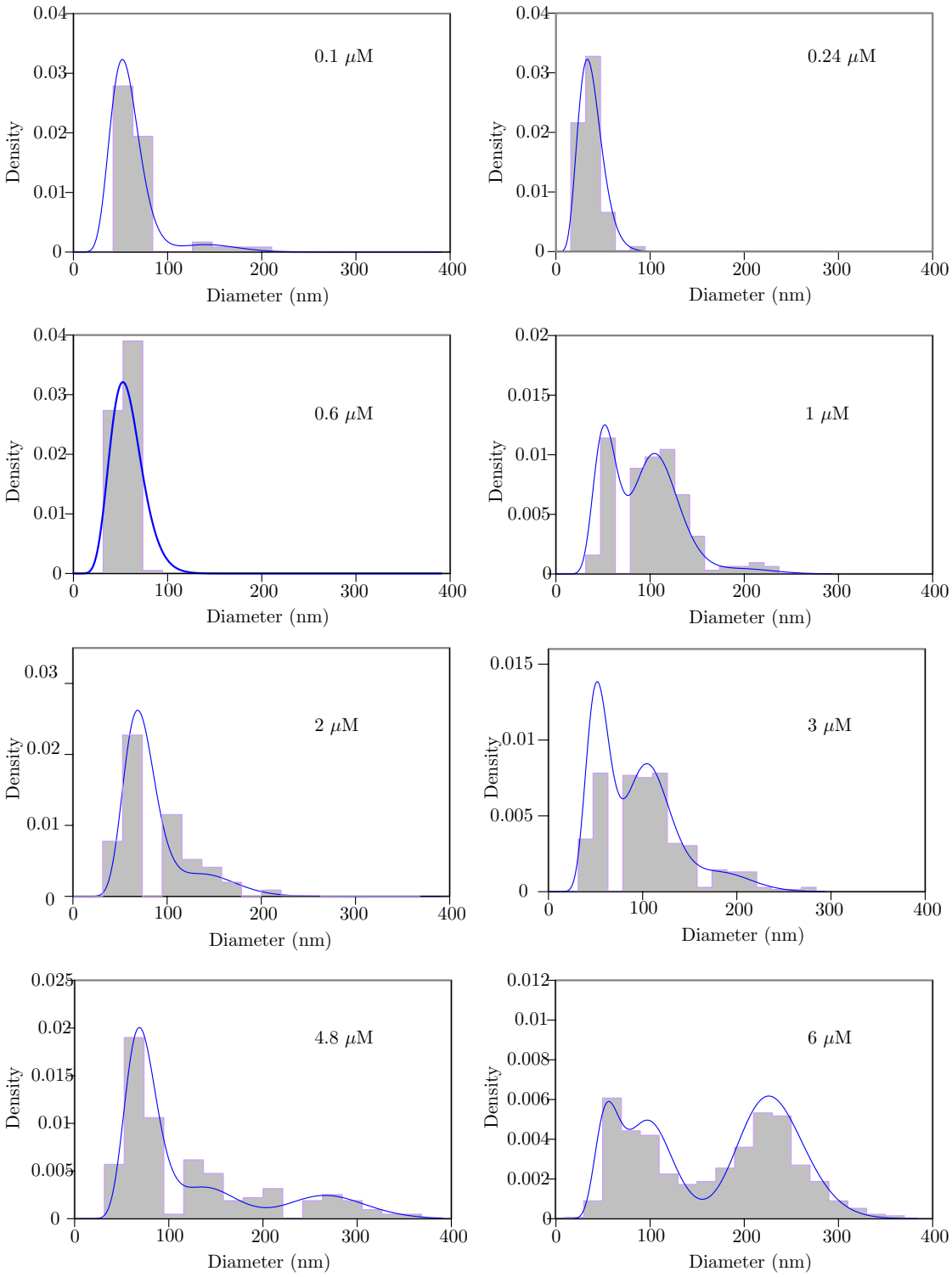

Figure 5.5: Histograms of the aggregates diameters as revealed by threshold and statistical analysis on the AFM images. The population fitting is provided with mixtures of gamma distributions.

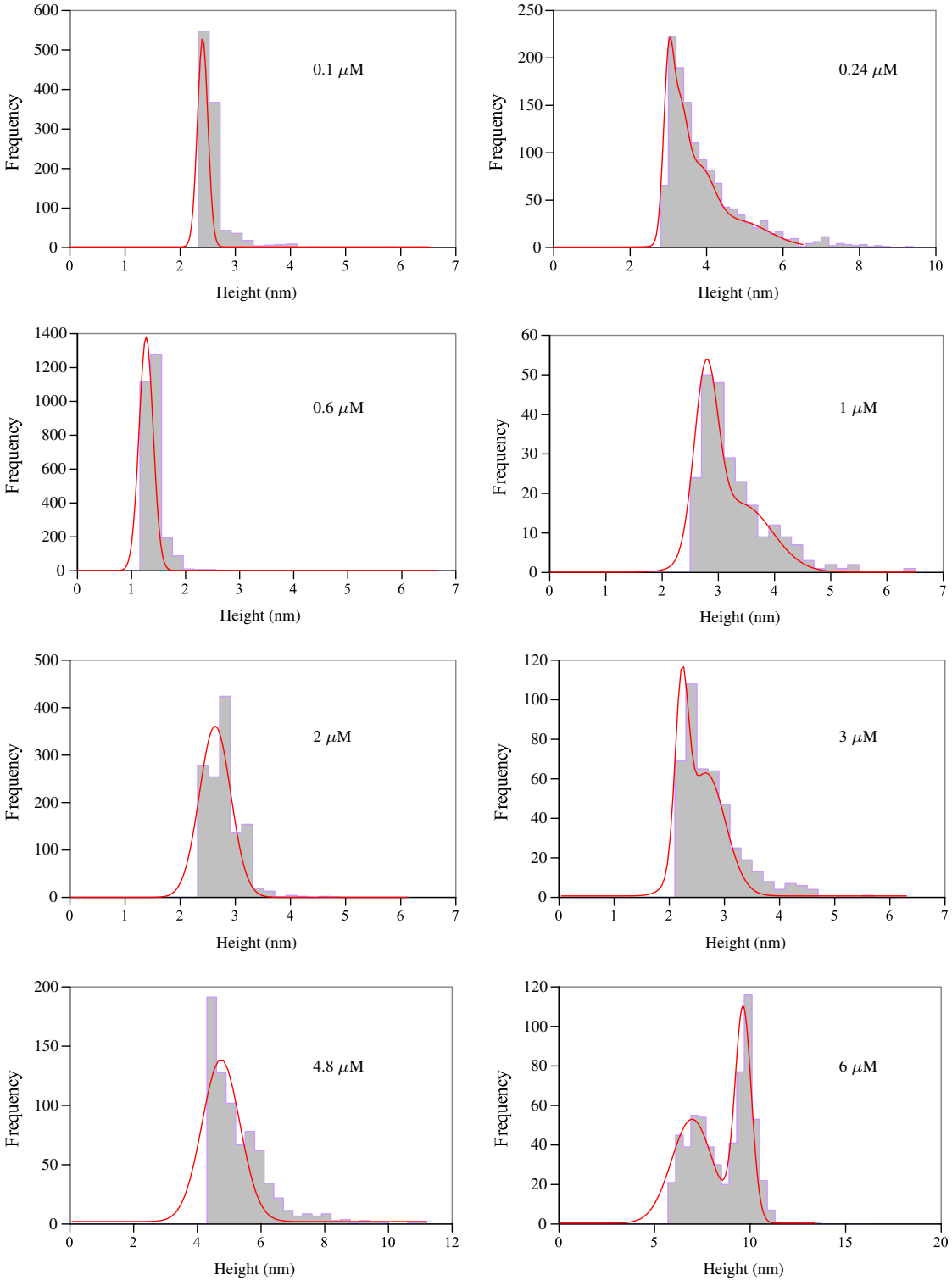

Figure 5.6: Histograms of the mean height of the aggregates' populations. The height is measured above the threshold level, and does not include the first monolayer of peptide.

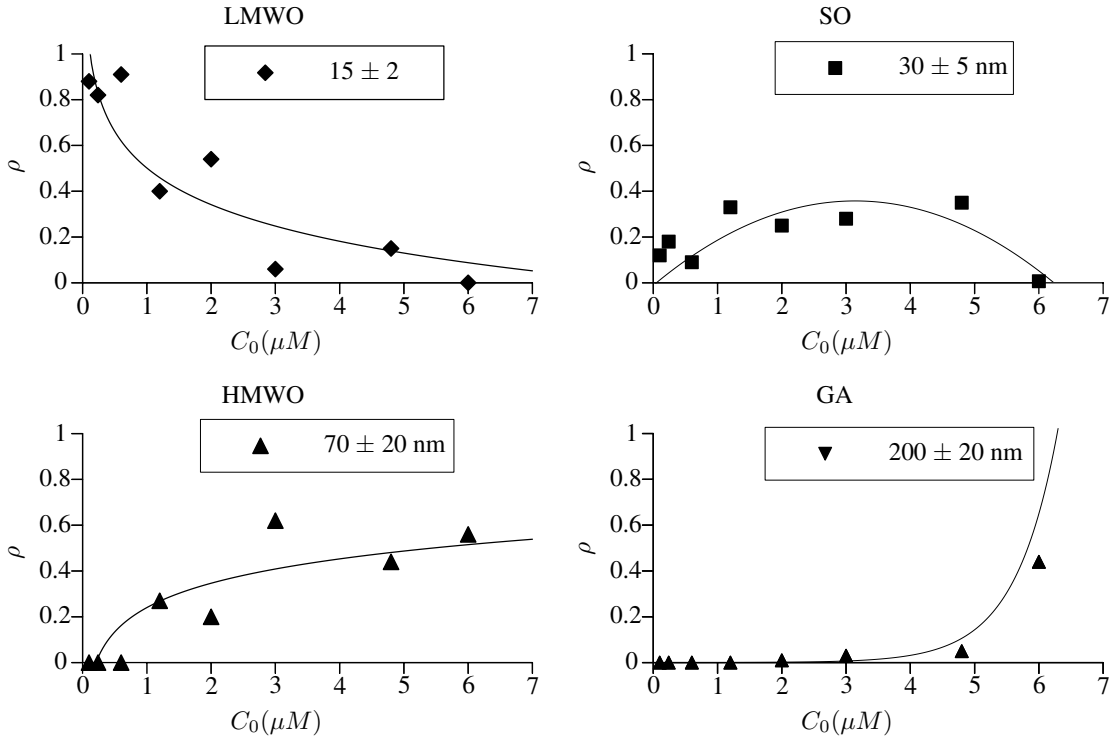

Figure 5.7: Trends of the population diameter with the initial concentration C_0 at the inlet of the microfluidic cell.

pearance of LMWO. At concentration between 2-3 μM a steady-state seems to be reached with LMWO and small oligomers coexisting in equilibrium with HMWO. Globular aggregates start to appear for a concentration above 3 μM which indeed seems to be critical for the onset of elongation. The increase of globular aggregates is correlated to the disappearance of the LMWO and small aggregate populations.

This process is governed by coalescence or other coarsening process as Ostwald ripening. This evolution demonstrates the coexistence of four populations. Nucleation of oligomers is an initial step, but it is the reservoir of smaller size oligomers that governs the growth of the larger aggregates towards proto-fibrils. Our experiment tells us that the concentration is a crucial experimental parameter. Microfluidics setup not only mimics the effect of crowding, but also guarantees a steady-state local concentration and a constant deposition rate, without which would not be possible to draw quantitative correlations a systematic variation of concentration.

5.3 Kinetic analysis of the smallest stable oligomer

We now adopt a kinetic model of nucleation for interpreting the experimental data in Section 5.2, with the aim to extract the critical size of the nucleus, viz. the size of the smallest stable oligomer starting the amyloid aggregation, and the diffusion coefficient of Aβ40. Here thermodynamic considerations do not apply as the nucleation is largely heterogeneous (occurring on the adsorbed first monolayer) and governed by the diffusion rate inside the channel and on the mica surface. The coarsening/coalescence event observed for highest concentrations is not kept into account, so only the nucleation and growth part of the amyloid cascade can be effectively described. In this regime, the growth rate of aggregates becomes [149]

$$dC_a/dt = k_{growth} C_n n_m \tag{5.1}$$

where C_a is the aggregate density at the surface, is k_{growth} the effective growth rate of a nucleus, C_n is the density of nuclei at the surface.

The rate at which the monomer density on the surface changes is:

$$dn_m(t)/dt = -k_{growth}C_n n_m - \sum_{n=2}^{\nu} k_{ass,n}C_{n-1}(t)C_m(t) + \sum_{n=2}^{n-1} k_{diss,n}C_n(t) + J_{diff}C_0 t^{1/2} \qquad (5.2)$$

where n_m is the density of monomer at the surface, C_m the concentration in the solution, J the rate of growth of the aggregates, k_{ass}, k_{diss} are the rates of association/dissociation of nuclei with size smaller or equal to the critical nucleus size $\nu - 1$. The last term to the right represents the deposition rate governed by the diffusion, as derived from the expression of Lang and Coates (1976)[150]

$$n_m(t) = C_0/MW \cdot (4Dt/p)^{1/2} = 2J_{diff}C_0 t^{1/2} \qquad (5.3)$$

C_0 is the concentration of the solution in the reservoir, that we assume to be kept constant also in the channel (viz. the local concentration in the channel $C_m(t) = C_0$) We assume a quasi-equilibrium in the nucleation/dissociation of unstable nuclei, such that the two central terms on the right hand side sum up to zero:

$$k_{ass,n}C_{n-1}C_m = k_{diss,n}C_n \qquad \text{for } n = 2...\nu \qquad (5.4)$$

By inserting eq.5.4 into eq. 5.2, we obtain:

$$dn_m(t)/dt = -k_{growth}C_n n_m(t) - k^{eff}_{nucl,\nu}C_n + \frac{1}{2}J_{diff} \cdot \frac{C_0}{t^{1/2}} \qquad (5.5)$$

where $k^{eff}_{nucl,\nu}$ represents the effective rate for nucleation. Upon integration, the time evolution

of n_m becomes:

$$n_m(t) = -[1 - \exp(-k_{growth} C_n t)] \frac{k^{eff}_{nucl,\nu}}{k_{growth}} + \frac{J_{diff}}{2} C_0 \int_0^t \frac{\exp(-k_{growth} C_n t)}{t^{1/2}} dt \qquad (5.6)$$

which can be written as:

$$n_m(t) = -[1 - \exp(-k_{growth} C_n t)] \frac{k^{eff}_{nucl,\nu}}{k_{growth}} + \frac{1}{2} (\frac{\pi}{k_{growth} C_n})^{1/2} J_{diff} C_0 \mathrm{erf}(-k_{growth} C_n t)^{1/2} \qquad (5.7)$$

where erf(x) is the Error function [151]

Conserving the first term of the Taylor expansion, $(\mathrm{erf}(k_{growth} C_n t)^{1/2} = \frac{2}{\sqrt{\pi}} (k_{growth} C_n t)^{1/2})$, i.e. at short times with respect to $1/(k_{growth} C_n)$, eq. 5.7 becomes:

$$n_m(t) = -k^{eff}_{nucl,\nu} K_{eq} C_0^{\nu} t + J_{diff} C_0 t^{1/2} \qquad (5.8)$$

We have assumed in eq.5.8 that the nuclei are at equilibrium with the monomer in the solution:

$$C_n = K_{eq} C_0^{\nu} \qquad (5.9)$$

Eq. 5.8 represents well the conditions is the concentration of the monomer pool that is our experimental variable in Sect. 5.3. The total volume V_m of Aβ40 adsorbed on the surface turns out to be proportional to

$$V_m(t, C_0) \propto n_m + C_a + C_n \qquad (5.10)$$

$$V_m(t, C_0) \propto k^{eff}_{nucl,\nu} K_{eq} C_0^{\nu} t + J_{diff} C_0 t^{1/2} + K_{eq} C_0^{\nu} \qquad (5.11)$$

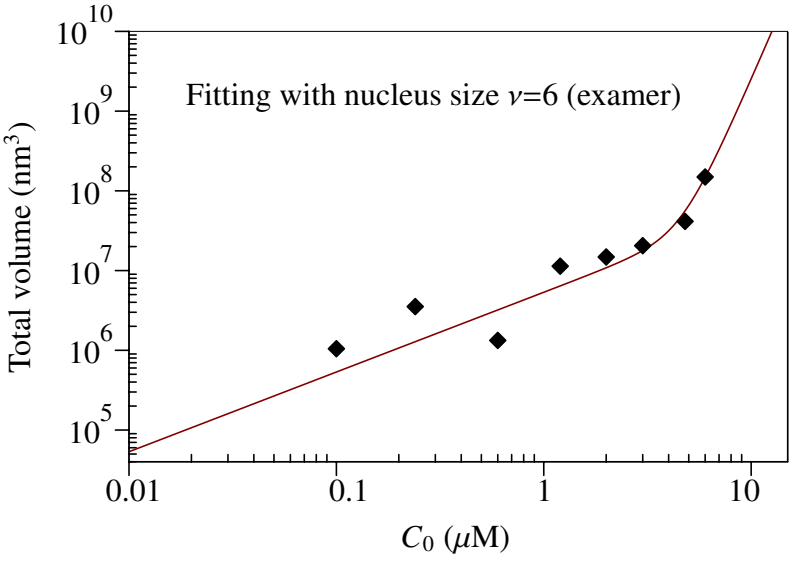

Figure 5.8: Total volume of aggregates deposited on the mica wall of the microfluidic device, after 24 hours. See Sect.5.2. The fitting was done with eq.**??**. The best fit suggests a nucleus size comprised between 2 and 5 peptide units.

The right hand side of eq.5.11 is proportional to the volume adsorbed on the surface that we measure from the AFM images, and plot in Fig.5.8. .

It is now possible to extract the value of the stable nucleus size ν fitting the concentration-dependence of the mass/volume of adsorbed peptide vs C_0 with eq.5.11, expressed as $V_{tot}(C_0) \propto AC_0^{\nu} + BC_0$. At low concentration, the diffusive term eq.**??** is dominant. In fig.5.8 we show the deposited volume vs C_0 after 24 hrs. We disregarded from the histograms in Sect. 5.3 the largest size populations, as influenced by coalescence.

Best fit parameters are $A_{24h} \simeq 5.3 \cdot 10^6$, $B_{24h} \simeq 2.5 \times 10^3$,$\nu = 6$. Thus, we infer that within the approximation of our model the smallest stable Aβ40 oligomer is the hexamer.

5.4 Microconfined adsorption experiment to obtain diffusion coefficient

The rate of adsorption in the case of low-concentration solutions, when the steady-state concentration profile $C(x,z)$ has been established, can be written as:[152]

$$\partial\Gamma/\partial t = D \cdot \partial C/\partial y|_{z=0} = k(x)C_b \tag{5.12}$$

where Γ is the interfacial concentration, D is the diffusion coefficient, C_b is the concentration in the bulk solution and $k(x)$ is the kinetic constant of the overall process (including adsorption) at coordinate x. The extensive process is expressed in terms of the concentration of solution at distance x from the microchannel inlet ($C(x,0)$), by means of the adsorption kinetic constant at the interface k_A

$$k(x)C_b(x,y) = k_A C(x,0) \tag{5.13}$$

In case of the fully transport-controlled process ($C(x,0) = 0$), the kinetic constant k at distance x from the entrance of the channel depends only on diffusion D and convection, expressed by the wall shear rate γ. According to Léveque (1928) its expression is $k_{\mathrm{Lev}}(x) = 0.538(D^2\gamma/x)^{1/3}$.[153] When adsorption is controlled only by the interfacial reaction, the kinetic constant k is equal to k_A and practically does not depend on x. For a given solute diffusion coefficient, the higher the adsorption kinetic constant, k_A, the larger the interfacial depletion. The depletion d(x) of solute at the interface is defined as:

$$d(x) = 1 - C(x,0)/C_b \tag{5.14}$$

The steady-state adsorption rate is related to the slope of C(x, z) at the wall, therefore we

obtain:

$$\partial\Gamma(x,t)/\partial t = D \cdot (C_b - C(x,0))/\delta(x) = k(x)C_b \tag{5.15}$$

where $\delta(x)$ is the thickness of the depletion layer in function of the coordinate x. When approaching the Léveque limit ($d \to 1$), $k(x) \ll k_A$, while for the opposite case of negligible depletion $k(x) \to k_A$. The Damkohler number, $\mathrm{Da} = k_A / \langle v \rangle$, where $\langle v \rangle$ is the average velocity of the fluid, is used as a criterion to separate the domains of control by the interfacial reaction (Da << 1) and by transport (Da >> 1), especially in studies concerning porous media.

The experimental determination of the adsorption kinetic constant k_A has three major sources of difficulties: (1) mass transport, to take into account with simple geometries of rectangular channels or circular tubes, (2) steric hindrance at the interface, which can be limited by using low-concentration solutions, and (3) determination of low interfacial concentration, which requires very sensitive techniques, usually using radioactive or fluorescently labeled molecules like in the total internal reflection fluorescence (TIRF) technique. Optical techniques such as surface plasmon resonance and optical waveguide lightmode spectroscopy (OWLS) provide the means to measure low interfacial concentrations without labeled molecules. Atomic force microscopy gives the necessary microscopic detail to discern between similar aggregate conformations, which are relevant from biologic point of view, but which are indistinguishable with other intensity based measurement.

The general expression to derive the constant $k(x)$ in function of k_A is not easily accessible and depends on hydrodynamic calculations [154] , it appears preferable to have k_A obtained experimentally from measurement of $k(x)$. Good approximations of the theoretical description can be obtained at the two limits (transport controlled or interfacial reaction). the total resistance (time) of the adsorption process is the sum of one resistance due to the transport and the other resistance due to the interfacial reaction. The following approximations are reported [154]

$$k^{-1} = k_{\mathrm{Lev}}^{-1} + 0.684 k_A^{-1} \qquad \text{transport controlled} \tag{5.16}$$

$$k^{-1} = 0.827 k_{\mathrm{Lev}}^{-1} + k_A^{-1} \qquad \text{interfacial reaction} \tag{5.17}$$

If no coupling between transport and the interfacial reaction is considered, both the previous equalities can be comprised into: $k^{-1} = k_A^{-1} + k_{\mathrm{Lev}}^{-1}$

Although employing a strong assumption on the uniformity of the depletion layer, it is admitted to deduce k_A from calculated k_{Lev} and experimental $k(x)$, by means of a two parameter fit, in D and k_A:

$$k = k_A / D^{2/3} \cdot [(u' - D^{2/3})(0.451u' - D^{2/3})/(-0.625u' + D^{2/3})] \tag{5.18}$$

with $u' = k(x/\gamma)^{1/2}/0.538 = uD^{2/3}$. The application of the fit to the adsorption data of the Aβ40 on mica in microconfined channels, provides two parameters: the diffusion coefficient D and the adsorption kinetic constant k_A, with given buffer and pH of the solution.

The adsorption of monomers and aggregates of different dimensions was recorded by AFM images on the mica side of the microfluidic device, in correspondence of the main $125\,\mu m$ channel and the lateral 600 nm mesoscopic channels. See fig. (5.9,5.10,5.11,5.12). The time at which AFM image was taken, was set at 1, 5, 10, 30 minutes, to obtain a snapshot of the initial stages of peptide adsorption. The time resolution achievable with this method is not comparable with the standard fluorescence techniques, however the quantification of mass and the characterization of the oligomer morphologies is taking a considerable advantage from the nanometric resolution provided by scanning probe microscopy.

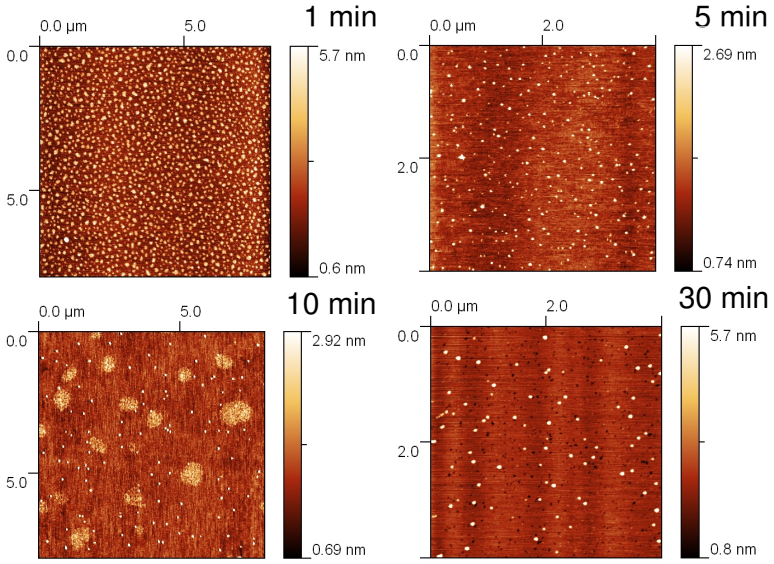

Figure 5.9: AFM time shots of amyloid oligomers adsorbed in the main channel (diameter 125 μm), initial concentration $C_0 = 1\mu M$

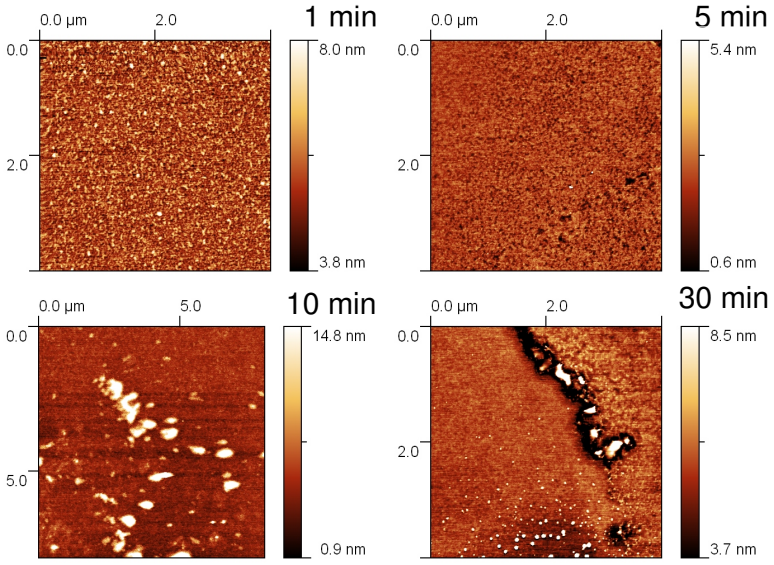

Figure 5.10: AFM time shots of amyloid oligomers adsorbed in the main channel (diameter 125 μm), initial concentration $C_0 = 5\mu M$

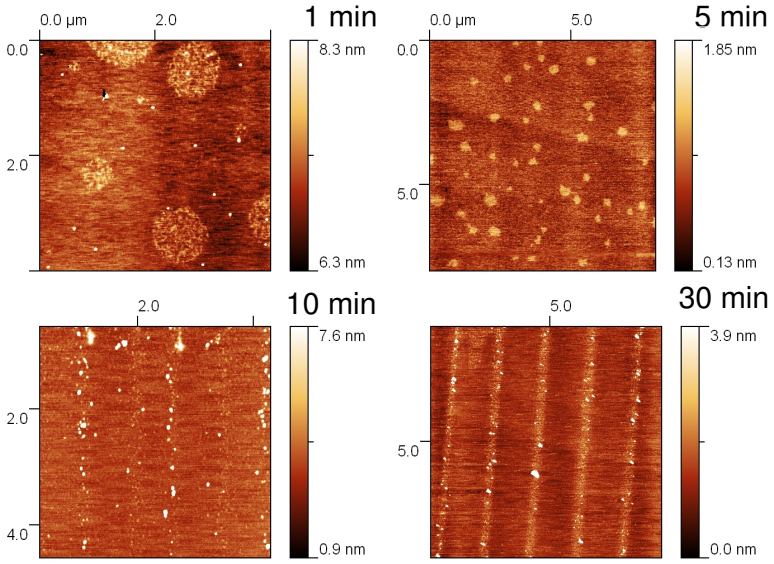

Figure 5.11: AFM time shots of amyloid oligomers adsorbed in the lateral mesoscopic channel (width 600 nm), initial concentration $C_0 = 1\mu M$

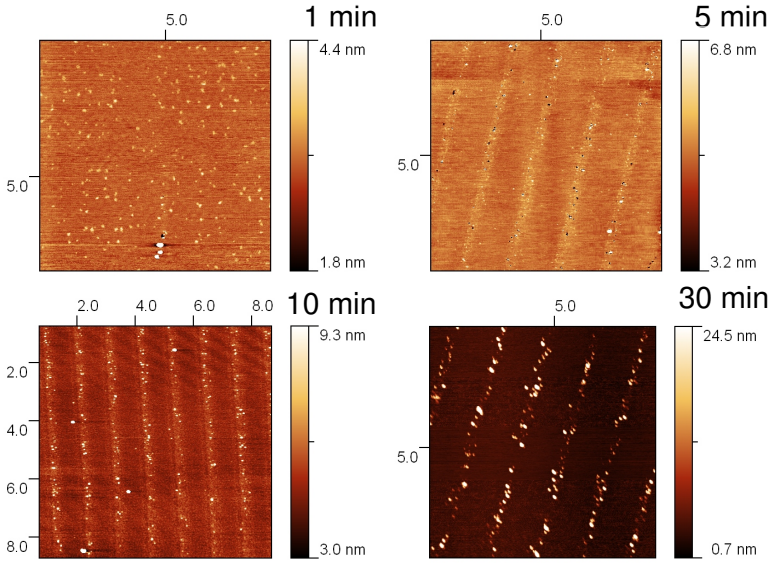

Figure 5.12: AFM time shots of amyloid oligomers adsorbed in the lateral mesoscopic channel (width 600 nm), initial concentration $C_0 = 5\mu M$

The adsorption kinetic data, expressed in terms of volume of the peptide on the mica surfaces is summarized in fig , where I reported the results obtained in the main channel

(MC) and in the side channels (SC) after incubation with two different initial concentrations at the inlet ($1\,\mu M$ and $5\,\mu M$).

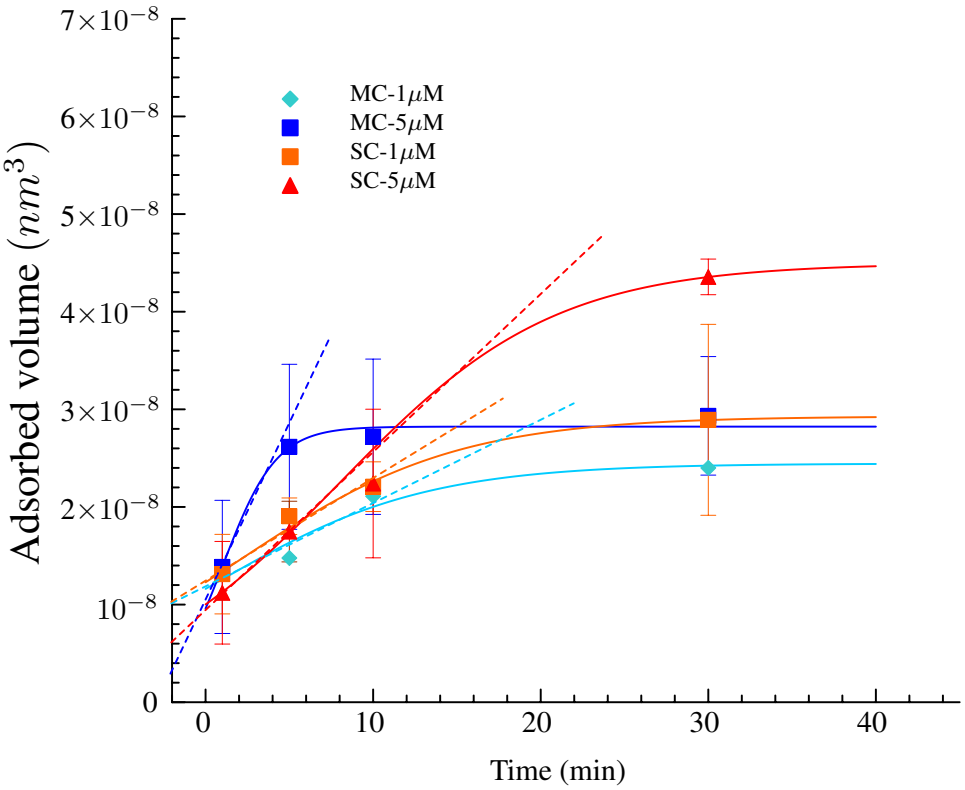

Figure 5.13: Adsorption of β amyloid peptide on the mica wall of the microfluidic cell. The diffusion coefficient can be determined taking into account the concentration profiles induced at the main (MC) and mesoscopic (SC) channels, during the initial stages of adsorption (see text). The linear fit between the measured adsorption and the shear characteristic of the flow, allow us to calculate diffusivity of 1.57×10^{-7}cm s^{-1}

Within the microfluidic environment, the presence of buffer, employed to reach equilibrium of the pH in bulk solution, does influence the adsorption rate and the morphology of the aggregate discovered on the surface as it is possible to evince from the adsorption curves obtained for the side channels in experiment performed with phosphate buffer concentration raised to 1x, instead of 0.1x generally adopted in the other run.

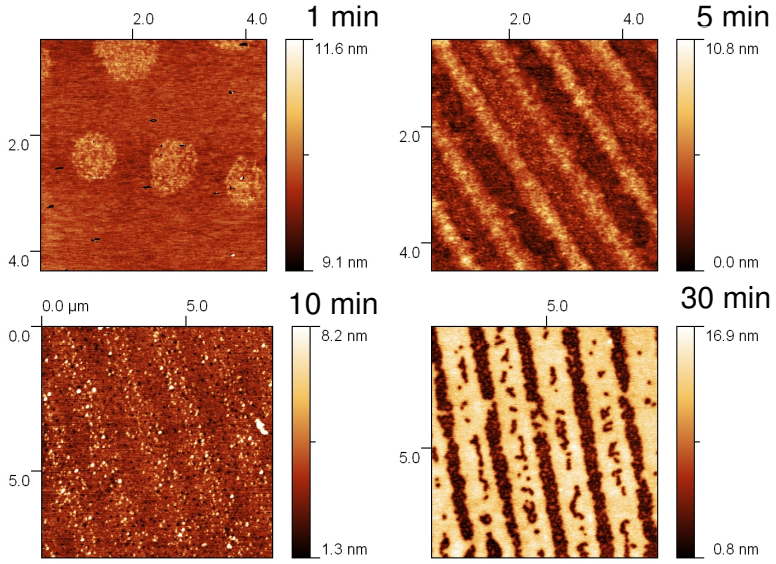

Figure 5.14: AFM time shots of amyloid oligomers adsorbed in the lateral mesoscopic channel (width 600 nm), initial concentration $C_0 = 1\mu M$, in PBS buffer solution with dilution 1x.

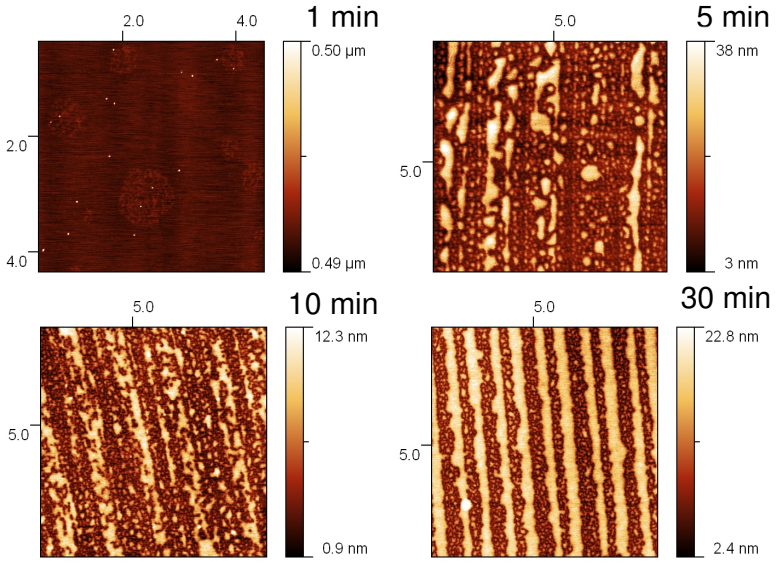

Figure 5.15: AFM time shots of amyloid oligomers adsorbed in the lateral mesoscopic channel (width 600 nm), initial concentration $C_0 = 5\mu M$, in PBS buffer solution with dilution 1x.

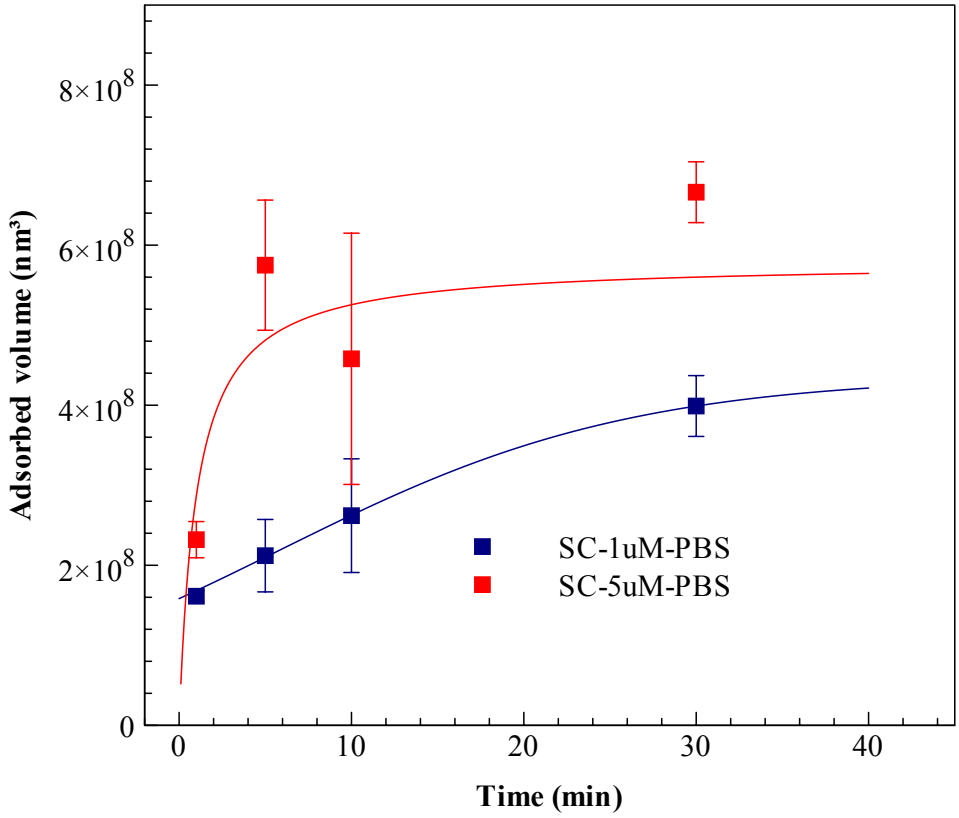

Figure 5.16: Adsorption of β amyloid peptide on the mica wall of the microfluidic cell. in presence of PBS buffer solution, diluted 1x. The total volume adsorbed is sensibly higher, due to the presence of saline buffer.

Bibliography

(1) Harris, T. D. et al. *SCIENCE* **2008**, *320*, 106–109.

(2) Bornhop, D. J.; Latham, J. C.; Kussrow, A.; Markov, D. A.; Jones, R. D.; Sorensen, H. S. *SCIENCE* **2007**, *317*, 1732–1736.

(3) Ottesen, E. A.; Hong, J. W.; Quake, S. R.; Leadbetter, J. R. *SCIENCE* **2006**, *314*, 1464–1467.

(4) Femoni, C.; Kaswalder, F.; Iapalucci, M. C.; Longoni, G.; Mehlstäubl, M.; Zacchini, S.; Ceriotti, A. *Angew. Chem. Int. Ed.* **2006**, *45*, 2060.

(5) Femoni, C.; Kaswalder, F.; Iapalucci, M.; Longoni, G.; Mehlstaubl, M.; Zacchini, S.; Ceriotti, A. *Angew. Chem.-Int. Ed.* **2006**, *45*, 2060–2062.

(6) Femoni, C.; Kaswalder, F.; Iapalucci, M.; Longoni, G.; Mehlstaubl, M.; Zacchini, S. *Chem. Commun. (Cambridge, U. K.)* **2005**, 5769–5771.

(7) Engel, M.; Small, J. P.; Steiner, M.; Freitag, M.; Green, A. A.; Hersam, M. C.; Avouris, P. *ACS NANO* **2008**, *2*, 2445–2452.

(8) Xie, X.; Mai, Y.; Zhou, X. *MATERIALS SCIENCE & ENGINEERING R-REPORTS* **2005**, *49*, 89–112.

(9) Kedem, S.; Schmidt, J.; Paz, Y.; Cohen, Y. *Langmuir* **2005**, *21*, 5600–5604.

(10) Xin, H.; Woolley, A. *Nano Lett.* **2004**, *4*, 1481–1484.

(11) Fan, Z.; Advani, S. *Polymer* **2005**, *46*, 5232–5240.

(12) Thathiah, A.; Spittaels, K.; Hoffmann, M.; Staes, M.; Cohen, A.; Horre, K.; Vanbrabant, M.; Coun, F.; Baekelandt, V.; Delacourte, A.; Fischer, D. F.; Pollet, D.; De Strooper, B.; Merchiers, P. *SCIENCE* **2009**, *323*, 946–951.

(13) Brody, D. L.; Magnoni, S.; Schwetye, K. E.; Spinner, M. L.; Esparza, T. J.; Stocchetti, N.; Zipfel, G. J.; Holtzman, D. M. *SCIENCE* **2008**, *321*, 1221–1224.

(14) Petkova, A.; Leapman, R.; Guo, Z.; Yau, W.; Mattson, M.; Tycko, R. *SCIENCE* **2005**, *307*, 262–265.

(15) Wasmer, C.; Lange, A.; Van Melckebeke, H.; Siemer, A. B.; Riek, R.; Meier, B. H. *SCIENCE* **2008**, *319*, 1523–1526.

(16) Walsh, D.; Tseng, B.; Rydel, R.; Podlisny, M.; Selkoe, D. *Biochemistry* **2000**, *39*, 10831–10839.

(17) Mastrangelo, I.; Hearing, J.; Liu, W.; Ahmed, M.; Wang, C.; Hough, P.; Smith, S. *Biophys. J.* **2005**, *88*, 155A.

(18) Anderson, M.; Bocharova, O.; Makarava, N.; Breydo, L.; Salnikov, V.; Baskakov, I. *J. Mol. Biol.* **2006**, *358*, 580–596.

(19) Walsh, D.; Klyubin, I.; Fadeeva, J.; Cullen, W.; Anwyl, R.; Wolfe, M.; Rowan, M.; Selkoe, D. *NATURE* **2002**, *416*, 535–539.

(20) Yaar, M.; Zhai, S.; Fine, R.; Eisenhauer, P.; Arble, B.; Stewart, K.; Gilchrest, B. *J. Biol. Chem.* **2002**, *277*, 7720–7725.

(21) Xia, Y.; Whitesides, G. *Angew. Chem.-Int. Ed.* **1998**, *37*, 551–575.

(22) Cavallini, M.; Biscarini, F. *Nano Lett.* **2003**, *3*, 1269–1271.

(23) Thorsen, T.; Maerkl, S.; Quake, S. *Science* **2002**, *298*, 580–584.

(24) Sui, G.; Wang, J.; Lee, C.-C.; Lu, W.; Lee, S. P.; Leyton, J. V.; Wu, A. M.; Tseng, H.-R. *ANALYTICAL CHEMISTRY* **2006**, *78*, 5543–5551.

(25) Israelachvili, J. N.; Berman, A. D. *Surface Forces and Microrheology of Molecularly Thin Liquid Films in Handbook of Micro/Nanotribology*; CRC Press, 1999.

(26) Ando, Y. *Geometry and Chemical Effects on Friction and Adhesion under Negligible Loads*; Taylor & Francis, 2008.

(27) Cavallini, M.; Stoliar, P.; Moulin, J.; Surin, M.; Leclere, P.; Lazzaroni, R.; Breiby, D.; Andreasen, J.; Nielsen, M.; Sonar, P.; Grimsdale, A.; Mullen, K.; Biscarini, F. *Nano Lett.* **2005**, *5*, 2422–2425.

(28) Rotkina, L.; Lin, J.; Bird, J. *Appl. Phys. Lett.* **2003**, *83*, 4426–4428.

(29) Rao, C.; Deepak, F.; Gundiah, G.; Govindaraj, A. *Prog. Solid State Chem.* **2003**, *31*, 5–147.

(30) Gunawidjaja, R.; Jiang, C.; Ko, H.; Tsukruk, V. V. *Adv. Mater.* **2006**, *18*, 2895+.

(31) Hong, B.; Bae, S.; Lee, C.; Jeong, S.; Kim, K. *Science* **2001**, *294*, 348–351.

(32) Zhang, S.; Jiang, Z.; Xie, Z.; Xu, X.; Huang, R.; Zheng, L. *J. Phys. Chem. B* **2005**, *109*, 9416–9421.

(33) Mieszawska, A.; Slawinski, G.; Zamborini, F. *J. Am. Chem. Soc.* **2006**, *128*, 5622–5623.

(34) Judai, K.; Nishijo, J.; Nishi, N. *Adv. Mater.* **2006**, *18*, 2842+.

(35) Wang, W.; Wang, S.-Y.; Wang, K.-Y.; Gao, Y.-L.; Liu, M. *Solid State Commun.* **2006**, *140*, 325–328.

(36) Su, C.; Goforth, A.; Smith, M.; Pellechia, P.; zur Loye, H. *J. Am. Chem. Soc.* **2004**, *126*, 3576–3586.

(37) Remita, H.; Keita, B.; Torigoe, K.; Belloni, J.; Nadjo, L. *Surf. Sci.* **2004**, *572*, 301–308.

(38) Cavallini, M.; Murgia, M.; Biscarini, F. *Nano Lett.* **2001**, *1*, 193–195.

(39) KIM, E.; XIA, Y.; WHITESIDES, G. *Nature* **1995**, *376*, 581–584.

(40) Messer, B.; Song, J.; Yang, P. *J. Am. Chem. Soc.* **2000**, *122*, 10232–10233.

(41) Leclere, P.; Surin, M.; Brocorens, P.; Cavallini, M.; Biscarini, F.; Lazzaroni, R. *Material Science & Engineering R, Reports* **2006**, *55*, 1–56.

(42) Menozzi, C.; Corradini, V.; Cavallini, M.; Biscarini, F.; Betti, M.; Mariani, C. *Thin Solid Films* **2003**, *428*, 227–231.

(43) Innocenti, M.; Cattarin, S.; Cavallini, M.; Loglio, F.; Foresti, M. *J. Electroanal. Chem.* **2002**, *532*, 219–225.

(44) Dimitrakopoulos, C. D.; Malenfant, P. R. L.; Mater, A. *Adv. Mater.* **2002**, *14*, 99.

(45) Katz, H. E.; Bao, Z. N.; Gilat, S. L.; Res, A. C. *Acc. Chem. Res.* **2001**, *34*, 359.

(46) Barbarella, G.; Melucci, M.; Sotgiu, G. *Adv. Mater.* **2005**, *17*, 1581.

(47) *Organic Electronics: Materials, Manufacturing and Applications*; Klauk, E. H., Ed.; Wiley-VCH: Weinheim, 2007.

(48) Melucci, M.; Barbarella, G.; Zambianchi, M.; Biscarini, F.; Cavallini, M.; Bongini, A.; Mazzeo, M.; Gigli, G. *Macromolecules* **2004**, *37*, 5692.

(49) Leclère, P.; Surin, M.; Cavallini, M.; Biscarini, F.; Lazzaroni, R. *Mater. Sci. Eng., R* **2006**, *2006*, year.

(50) Leclère, P.; Surin, M.; Henze, O.; Jonkheijm, P.; Biscarini, F.; Cavallini, M.; Feast, W. J.; Kilbinger, A. F. M.; Lazzaroni, R.; Meijer, E. W.; Schenning, A. P. H. J. *J. Mater. Chem.* **2004**, *14*, 1959.

(51) Menozzi, C.; Corradini, V.; Cavallini, M.; Biscarini, F.; Betti, M.; Mariani, C. *Thin Solid Films* **2003**, *428*, 227.

(52) Corradini, V.; Menozzi, C.; Cavallini, M.; Biscarini, F.; Betti, M. G.; Mariani, C. *Surf. Sci.* **2003**, *532*, 249.

(53) Briseno, A. L.; Mannsfeld, S. C. B.; Jenekhe, S. A.; Bao, Z.; Xia, Y. *Mater. Today* **2008**.

(54) Cavallini, M.; Facchini, M.; Albonetti, C.; Biscarini, F. *Phys. Chem. Chem. Phys.* **2007**, *10*, 20.

(55) Bao, Z.; Rogers, J. A.; Katz, H. E.; J, *J. Mater. Chem.* **1999**, *9*, 1895.

(56) Wu, Y.; Li, Y.; Ong, B. S.; Liu, P.; Gardner, S.; Chiang, B. *Adv. Mater.* **2005**, *17*, 184.

(57) Sirringhaus, H.; Kawase, T.; Friend, R. H.; Shimoda, T.; Inbasekaran, M.; Wu, W.; Woo, E. P. *Science* **2000**, *290*, 2123.

(58) Gamerith, S.; Klug, A.; Scheiber, H.; Scherf, U.; Moderegger, E.; List, E. J. W. *Adv. Funct. Mater.* **2007**, *17*, 3111.

(59) Sekitani, T.; Noguchi, Y.; Zschieschang, U.; Klauk, H.; Someya, T. *Proc. Natl. Acad. Sci. USA* **2008**, *105*, 4976.

(60) Kim, D.; Jeong, S.; Moon, J.; Han, S.; Chung, J. *Appl. Phys. Lett.* **2007**, *91*, 071114.

(61) Tate, J.; Rogers, J. A.; Jones, C. D. W.; Vyas, B.; Murphy, D. W.; Li, W.; Bao, Z.; Slusher, R. E.; Dodabalapur, A.; Katz, H. E. *Langmuir* **2000**, *16*, 6054.

(62) Loo, Y. L.; Someya, T.; Baldwin, K. W.; Bao, Z.; Ho, P.; Dodabalapur, A.; Katz, H. E.; Rogers, J. A. *Proc. Natl. Acad. Sci. USA* **2002**, *99*, 10252.

(63) Wang, Z.; Yuan, J. F.; Zhang, J.; Xing, R. B.; Yan, D. H.; Han, Y. C. *Adv. Mater.* **2003**, *15*, 1009.

(64) Hu, J.; Beck, R. G.; Deng, T.; Westervelt, R. M.; Maranowski, K. D.; Gossard, A. C.; Whitesides, G. M. *Appl. Phys. Lett.* **1997**, *71*, 2020.

(65) Menard, E.; Meitl, M. A.; Sun, Y.; Park, J.-U.; Shir, D. J. L.; Nam, Y.-S.; Jeon, S.; Rogers, J. A. *Chem. Rev.* **2007**, *107*, 117.

(66) Greco, P.; Cavallini, M.; Stoliar, P.; Quiroga, S. D.; Dutta, S.; Zachini, S.; Lapalucci, M. C.; Morandi, V.; Milita, S.; Merli, P. G.; Biscarini, F. *J. Am. Chem. Soc.* **2008**, *130*, 1177–1182.

(67) Longoni, G.; Chini, P. J. *J. Am. Chem. Soc.* **1976**, *98*, 7225.

(68) Femoni, C.; Kaswalder, F.; Iapalucci, M. C.; Longoni, G.; Mehlstäubl, M.; Zacchini, S. *Chem. Commun.* **2005**, *2005*, year.

(69) Heaney, B. M. *Electrical Conductivity, Resistivity, in Electrical Measurement, Signal Processing, and Displays,*; CRC Press,: Boca Raton, FL, 2003.

(70) Akkerman, H. B.; Blom, P. W. M.; de Leeuw, D. M.; de Boer, B. *Nature* **2006**, *441*, 69.

(71) Serban, D. A.; Kilchytska, V.; Vlad, A.; Martin-Hoyas, A.; Nysten, B.; Jonas, A. M.; Geerts, Y. H.; Lazzaroni, R.; Bayot, V.; Flandre, D.; Melinte, S. *Appl. Phys. Lett.* **2008**, *92*, 143503.

(72) Katz, H. E.; Lovinger, A. J.; Laquindanum, J. G. *Chem. Mater.* **1998**, *10*, 457.

(73) Leroy, J.; Boucher, N.; Sergeyev, S.; Sferrazza, M.; Geerts, Y. H. *J. Org. Chem.* **2007**, *8*, 1256.

(74) Facchetti, A. *Mater. Today* **2007**, *10*, 28.

(75) Surin, M.; Leclère, P.; Lazzaroni, R.; Yuen, J. D.; Wang, G.; Moses, D.; Heeger, A. J.; Cho, S.; Lee, K. J. *J. Appl. Phys.* **2006**, *100*, 033712.

(76) Tans, S.; Devoret, M.; Groeneveld, R.; Dekker, C. *Nature* **1998**, *394*, 761–764.

(77) Joachim, C.; Gimzewski, J.; Aviram, A. *Nature* **2000**, *408*, 541–548.

(78) Seidel, R.; Graham, A.; Unger, E.; Duesberg, G.; Liebau, M.; Steinhoegl, W.; Kreupl, F.; Hoenlein, W. *Nano Lett.* **2004**, *4*, 831–834.

(79) Snow, E.; Novak, J.; Campbell, P.; Park, D. *Appl. Phys. Lett.* **2003**, *82*, 2145–2147.

(80) Chen, J.; Perebeinos, V.; Freitag, M.; Tsang, J.; Fu, Q.; Liu, J.; Avouris, P. *Science* **2005**, *310*, 1171–1174.

(81) Guo, X.; Myers, M.; Xiao, S.; Lefenfeld, M.; Steiner, R.; Tulevski, G. S.; Tang, J.; Baumert, J.; Leibfarth, F.; Yardley, J. T.; Steigerwald, M. L.; Kim, P.; Nuckolls, C. *Proc. Natl. Acad. Sci. U. S. A.* **2006**, *103*, 11452–11456.

(82) Star, A.; Bradley, K.; Gabriel, J.; Gruner, G. *Abstracts of Papers of The American Chemical Society* **2003**, *226*, 140–PMSE.

(83) Zhang, L.; Li, Z.; Tan, Y.; Lolli, G.; Sakulchaicharoen, N.; Requejo, F. G.; Mun, B. S.; Resasco, D. E. *Chem. Mater.* **2006**, *18*, 5624–5629.

(84) Huang, S.; Cai, X.; Du, C.; Liu, J. *J. Phys. Chem. B* **2003**, *107*, 13251–13254.

(85) Yu, G.; Li, X.; Lieber, C. M.; Cao, A. *J. Mater. Chem.* **2008**, *18*, 728–734.

(86) Zhang, Y.; Chang, A.; Cao, J.; Wang, Q.; Kim, W.; Li, Y.; Morris, N.; Yenilmez, E.; Kong, J.; Dai, H. *Appl. Phys. Lett.* **2001**, *79*, 3155–3157.

(87) Zhang, M.; Fang, S.; Zakhidov, A.; Lee, S.; Aliev, A.; Williams, C.; Atkinson, K.; Baughman, R. *Science* **2005**, *309*, 1215–1219.

(88) Kocabas, C.; Meitl, M.; Gaur, A.; Shim, M.; Rogers, J. *Nano Lett.* **2004**, *4*, 2421–2426.

(89) Golovko, V.; Li, H.; Kleinsorge, B.; Hofmann, S.; Geng, J.; Cantoro, M.; Yang, Z.; Jefferson, D.; Johnson, B.; Huck, W.; Robertson, J. *Nature Nanotechnology* **2005**, *16*, 1636–1640.

(90) Burghard, M.; Duesberg, G.; Philipp, G.; Muster, J.; Roth, S. *Adv. Mater.* **1998**, *10*, 584+.

(91) Oh, S.; Cheng, Y.; Zhang, J.; Shimoda, H.; Zhou, O. *Appl. Phys. Lett.* **2003**, *82*, 2521–2523.

(92) Liu, J.; Casavant, M.; Cox, M.; Walters, D.; Boul, P.; Lu, W.; Rimberg, A.; Smith, K.; Colbert, D.; Smalley, R. *Chem. Phys. Lett.* **1999**, *303*, 125–129.

(93) Oh, S.; Zhang, J.; Cheng, Y.; Shimoda, H.; Zhou, O. *Appl. Phys. Lett.* **2004**, *84*, 3738–3740.

(94) Spotnitz, M.; Ryan, D.; Stone, H. *J. Mater. Chem.* **2004**, *14*, 1299–1302.

(95) Meitl, M.; Zhou, Y.; Gaur, A.; Jeon, S.; Usrey, M.; Strano, M.; Rogers, J. *Nano Lett.* **2004**, *4*, 1643–1647.

(96) Valentini, L.; Taticchi, A.; Marrocchi, A.; Kenny, J. M. *J. Mater. Chem.* **2008**, *18*, 484–488.

(97) Dionigi, C.; Stoliar, P.; Ruani, G.; Quiroga, S. D.; Facchini, M.; Biscarini, F. *J. Mater. Chem.* **2007**, *17*, 3681–3686.

(98) Dillon, A.; Yudasaka, M.; Dresselhaus, M. *J. Nanosci. Nanotechnol.* **2004**, *4*, 691–703.

(99) Sondergard, O.; Gravesen, P. *Journal of Micromechanics and Microengineering* **1996**, *6*, 105–107.

(100) Whitesides, G.; Stroock, A. *Physics Today* **2001**, *54*, 42–48.

(101) McDonald, J.; Duffy, D.; Anderson, J.; Chiu, D.; Wu, H.; Schueller, O.; Whitesides, G. *Electrophoresis* **2000**, *21*, 27–40.

(102) Viola, I.; Pisignano, D.; Cingolani, R.; Gigli, G. *Anal. Chem.* **2005**, *77*, 591–595.

(103) J.A, S. *Level set methods and fast marching methods*; 1999.

(104) Craster, R. V.; Matar, O. K. *Langmuir* **2007**, *23*, 2588–2601.

(105) Afsar-Siddiqui, A.; Luckham, P.; Matar, O. *Langmuir* **2004**, *20*, 7575–7582.

(106) R. B. Bird, W. E. S.; Lightfoot, E. N. *Transport Phenomena*; 1960.

(107) Katz, E.; Yarin, A. L.; Salalha, W.; Zussman, E. *J. Appl. Phys.* **2006**, *100*, year.

(108) Kay, E. R.; Leigh, D. A.; Zerbetto, F. *Angew. Chem.-Int. Ed.* **2007**, *46*, 72–191.

(109) Dror, Y.; Salalha, W.; Khalfin, R.; Cohen, Y.; Yarin, A.; Zussman, E. *Langmuir* **2003**, *19*, 7012–7020.

(110) Advani, S. G.; Tucker, C. L.

(111) S.F., D. M. E. *The theory of polymer dynamics*; 1986.

(112) Rogers, S.; Venema, P.; Sagis, L.; van der Linden, E.; Donald, A. *Macromolecules* **2005**, *38*, 2948–2958.

(113) Bockrath, M.; Cobden, D.; McEuen, P.; Chopra, N.; Zettl, A.; Thess, A.; Smalley, R. *Science* **1997**, *275*, 1922–1925.

(114) Skakalova, V.; Kaiser, A. B.; Woo, Y. S.; Roth, S. *Phys. Rev. B* **2006**, *74*, year.

(115) Bockrath, M.; Cobden, D.; Lu, J.; Rinzler, A.; Smalley, R.; Balents, T.; McEuen, P. *Nature* **1999**, *397*, 598–601.

(116) Hunger, T.; Lengeler, B.; Appenzeller, J. *Phys. Rev. B* **2004**, *69*, year.

(117) Thess, A.; Lee, R.; Nikolaev, P.; Dai, H.; Petit, P.; Robert, J.; Xu, C.; Lee, Y.; Kim, S.; Rinzler, A.; Colbert, D.; Scuseria, G.; Tomanek, D.; Fischer, J.; Smalley, R. *Science* **1996**, *273*, 483–487.

(118) Sakatani, Y.; Boissiere, C.; Grosso, D.; Nicole, L.; Soler-Illia, G. J. A. A.; Sanchez, C. *Chem. Mater.* **2008**, *20*, 1049–1056.

(119) Sanchez, C.; Boissiere, C.; Grosso, D.; Laberty, C.; Nicole, L. *Chem. Mater.* **2008**, *20*, 682–737.

(120) Wong, S.; Kitaev, V.; Ozin, G. *J. Am. Chem. Soc.* **2003**, *125*, 15589–15598.

(121) Stein, A.; Li, F.; Denny, N. R. *Chem. Mater.* **2008**, *20*, 649–666.

(122) Somani, P.; Dionigi, C.; Murgia, M.; Palles, D.; Nozar, P.; Ruani, G. *Solar Energy Materials and Solar Cells* **2005**, *87*, 513–519.

(123) Diguna, L. J.; Shen, Q.; Kobayashi, J.; Toyoda, T. *Appl. Phys. Lett.* **2007**, *91*, year.

(124) Zhang, Y.; Wang, J.; Zhao, Y.; Zhai, J.; Jiang, L.; Song, Y.; Zhu, D. *J. Mater. Chem.* **2008**, *18*, 2650–2652.

(125) Kuo, C.-Y.; Lu, S.-Y. *Nature Nanotechnology* **2008**, *19*, year.

(126) Gratzel, M. *Nature* **2001**, *414*, 338–344.

(127) Gates, B.; Park, S.; Xia, Y. *Adv. Mater.* **2000**, *12*, 653+.

(128) Halaoui, L.; Abrams, N.; Mallouk, T. *J. Phys. Chem. B* **2005**, *109*, 6334–6342.

(129) Diguna, L. J.; Murakami, M.; Sato, A.; Kumagai, Y.; Ishihara, T.; Kobayashi, N.; Shen, Q.; Toyoda, T. *Japanese Journal of Applied Physics, Part 1: Regular Papers, Short Notes & Review Papers* **2006**, *45*, 5563–5568.

(130) Ruani, G.; Ancora, C.; Corticelli, F.; Dionigi, C.; Rossi, C. *Solar Energy Materials and Solar Cells* **2008**, *92*, 537–542.

(131) Velikov, K.; Christova, C.; Dullens, R.; van Blaaderen, A. *Science* **2002**, *296*, 106–109.

(132) Dionigi, C.; Calestani, G.; Ferraroni, T.; Ruani, G.; Liotta, L.; Migliori, A.; Nozar, P.; Palles, D. *J. Colloid Interface Sci.* **2005**, *290*, 201–207.

(133) Wang, J.; Li, Q.; Knoll, W.; Jonas, U. *J. Am. Chem. Soc.* **2006**, *128*, 15606–15607.

(134) Meng, Q.; Fu, C.; Einaga, Y.; Gu, Z.; Fujishima, A.; Sato, O. *Chem. Mater.* **2002**, *14*, 83–88.

(135) Goh, C.; Coakley, K.; McGehee, M. *Nano Lett.* **2005**, *5*, 1545–1549.

(136) Tiemann, M. *Chem. Mater.* **2008**, *20*, 961–971.

(137) Kim, J.; Fujita, S.; Shiratori, S. *Thin Solid Films* **2006**, *499*, 83–89.

(138) DIMITROV, A.; NAGAYAMA, K. *Chem. Phys. Lett.* **1995**, *243*, 462–468.

(139) Goldenberg, L.; Wagner, J.; Stumpe, J.; Paulke, B.; Gornitz, E. *Mater. Sci. Eng., C* **2002**, *22*, 405–408.

(140) Dionigi, C.; Stoliar, P.; Porzio, W.; Destri, S.; Cavallini, M.; Bilotti, I.; Brillante, A.; Biscarini, F. *Langmuir* **2007**, *23*, 2030–2036.

(141) Kelly, S.; Pollak, F.; Tomkiewicz, M. *J. Phys. Chem. B* **1997**, *101*, 2730–2734.

(142) KRALCHEVSKY, P.; NAGAYAMA, K. *Langmuir* **1994**, *10*, 23–36.

(143) Sutti, A.; Baratto, C.; Calestani, G.; Dionigi, C.; Ferroni, M.; Faglia, G.; Sberveglieri, G. *Sens. Actuators, B* **2008**, *130*, 567–573.

(144) Chen, J. I. L.; von Freymann, G.; Kitaev, V.; Ozin, G. A. *J. Am. Chem. Soc.* **2007**, *129*, 1196–1202.

(145) Camera-Roda, G.; Santarelli, F.; Martin, C. *Solar Energy Materials and Solar Cells* **2005**, *79*, 343–352.

(146) Stefani, M. *"Protein Folding and Misfolding, Relevance to Disease, and Biological Function" in Protein Misfolding in Neurodegenerative Diseases*; CRC Press - Taylor & Francis, 2007.

(147) Ma, Q.; Lim, G.; Harris-White, M.; Yang, F.; Ambegaokar, S.; Glabe, C.; Teter, B.; Frautschy, S.; Cole, G. *J. Neurosci. Res.* **2006**, *83*, 374–384.

(148) Deshpande, A.; Mina, E.; Glabe, C.; Busciglio, J. *J. Neurosci.* **2006**, *26*, 6011–6018.

(149) Cellmer, T.; Douma, R.; Huebner, A.; Prausnitz, J.; Blanch, H. *BIOPHYSICAL CHEMISTRY* **2007**, *125*, 350–359.

(150) Lang D, C. P. *J Mol Biol.* **1968**, 137–51.

(151) Abramowitz, M.; Stegun, I. A. *Handbook of Mathematical Functions with Formulas, Graphs, and Mathematical Tables*, ninth Dover printing, tenth GPO printing ed.; Dover: New York, 1964.

(152) Déjardin, P.; Vasina, E. N. *"Initial Adsorption Kinetics in a Rectangular Thin Channel, and Coverage-Dependent Structural Transition Observed by Streaming Potential" in Proteins at Solid-Liquid Interfaces*; Springer-Verlag Berline, 2006.

(153) Levich, V. *Physical Hydrodynamics.*; Prentice-Hall, Englewood Cliffs, NJ, USA, 1962.

(154) DEJARDIN, P.; LE, M.; WITTMER, J.; JOHNER, A. *Langmuir* **1994**, *10*, 3898–3901.

Appendix A

Photolithography

Optical photolithography may be modeled taking into account the following points:

Aerial image

Predicts the image of partially coherent diffraction limited projection (possibly distorted due to aberration). Careful consideration must be given to image defocusing throughout the resist film. Phase-shifting masks vary the phase of incident waves.

Prebake. Thermal decomposition of photoresist reactive compound during prebake can be described by 1st order kinetic model (change in the optical properties of the photoresist)

Exposure kinetics and post exposure bake.

Concentration of photo active compound. Diffusion of photoactive compound have effect on the solubility of the polymer resin in the positive resist. In chemically amplified resist deblocking chemistry affect polymer matrix, after generation of the acid catalytic compound.

Development and photoresist kinetics

Rate of dissolution of photoresist relative to chemical composition of developer. Generally an empirical data file is provided for development rate.

A.1 Aerial image formation

Diffraction theory apply to image formation. Fig. A.1 and Fig. A.2 show a scheme of light path and numerical apertures.

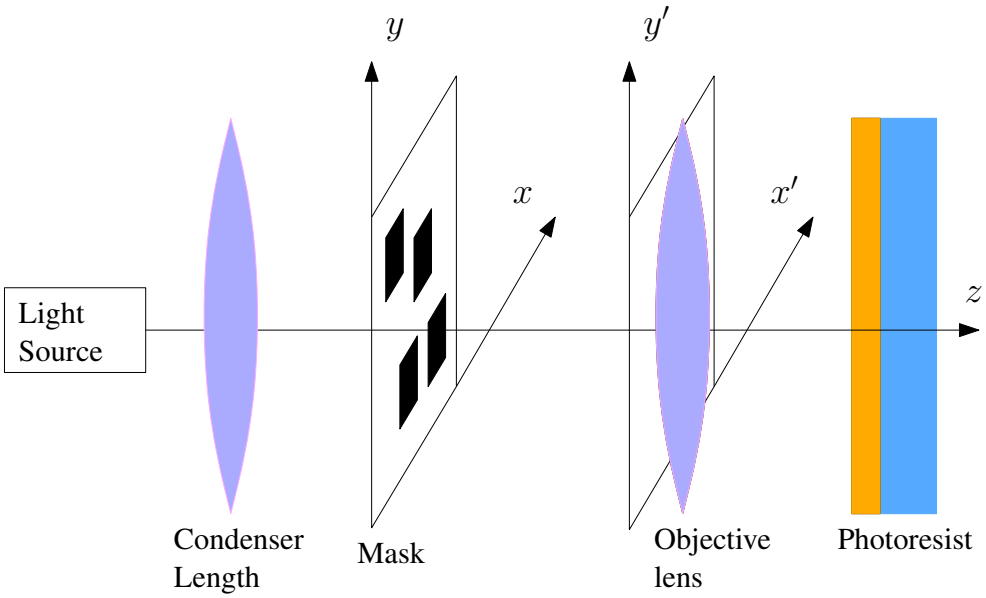

Figure A.1: Light path for projection photolithography

Scalar diffraction theory was used in 1882 by Kirchoff. Considering a reference coordinate system in the plane of the mask (x,y), the electric field transmitted across the mask is defined as $m(x,y)$. The electric field at the entry of the objective lens is the Fourier transform of the $m(x,y)$.

$$E(x',y') = \int\int m(x,y)e^{-2\pi i(f_x x + f_y y)}dxdy \tag{A.1}$$

, where x', y' are the coordinate in a plane just before the objective lens, $f_x = x'/\lambda z$ and $f_y = y'/\lambda z$ are spatial frequencies and z is the distance from the mask to the objective lens.

The numerical aperture NA equals the size of the maximum angle for diffracted ray, admitted by the lens.

At the end of the objective lens path, we have a transmittance field anti-transformed by the lens, of the intensity entering the numerical aperture. The pupil function $P$is defined to

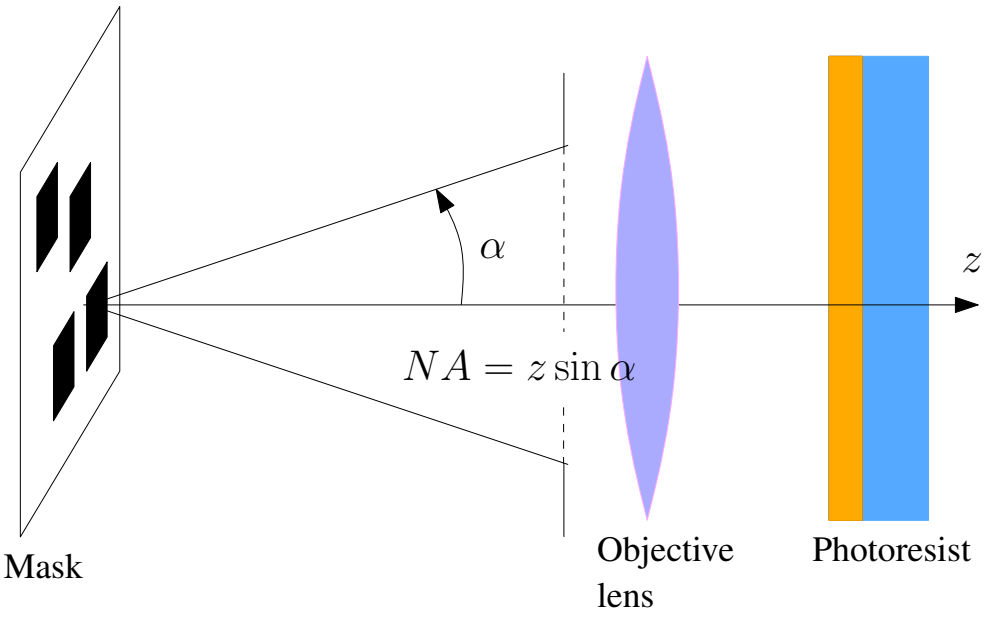

Figure A.2: Numerical aperture definition

calculate this intensity, and we have $P = 1$ inside the NA, and $P = 0$ everywhere else. The aerial image is the intensity distribution at the wafer top.

A.1.1 Aberrations

Aberrations can be defined as deviation of the real behavior of an optical system from the ideal one. Lens are designed according to linearized Snell's approximation law of small angles; therefore they introduce a systematic aberration in the aerial image.

Mathematically, aberrations are described as the difference in phase (or path difference) of the actual light wavefront compared to ideal wavefront predicted by Fourier equation (eq.A.1). Phase errors are calculated according to the Zernike polynomial (36 terms) formula, as a function of the radial position R and the angle θ.

A.2 Scalar model to calculate aerial image

In lithography, the mask image is projected on the photoresist. The propagation of the image into the resist can be modeled using different approximations. For reasonably thin photoresist film ($< 1\mu m$), the intensity within the film is described as $I(x,z) = I_i(x)I_S(z)$, where $I_i(x)$ is the aerial image (depending on the x,y coordinate) and $I_S(z)$ is the standing wave normal to the film (which depends on the coordinate z perpendicular to the film).

The image propagating through the film changes focus continuously. First-order scalar model to account for defocus is written as a function of the real part of the refraction index of the photoresist. $\delta(z) = \delta_0 + z/n$, where δ is defocus and n is the real part of the refraction index of the photoresist. The intensity field becomes $I(x,z) = I_i(x,\delta(z))I_S(z)$, with the assumption of normally incident plane waves.

In the high numerical aperture scalar model, light propagating into the resist can be described as superposition of plane waves traveling through the resist in different directions. Supposing to expose the photoresist directly (without the mask), the standing wave intensity can be determined with the formula:

$$E(z) = \frac{\tau_{ap}E_a(e^{-i2\pi n_p^r z/\lambda} + \rho_{ps}\tau^2 e^{-i2\pi n_p^r z/\lambda})}{1 + \rho_{ap}\rho_{ps}\tau_D^2} \tag{A.2}$$

where subscripts refer to the three phases respectively: air (a), photoresist (p) and substrate (s).

n_j (complex index of refraction) $n_j = n_j^r - ik_j$

τ_{ij} (transmission coefficients from component i to j) $\tau_{ij} = 2n_i/(n_i + n_j)$

ρ_{ij} (reflection coefficients from component i to j) $\rho_{ij} = (n_i - n_j)/(n_i + n_j)$

τ_D (internal transmittance) $\tau_D = e^{-i2\pi n_p D/\lambda}$

D (photoresist thickness)

Absorption is taken into account through the imaginary part of the index of refraction

since $a = 4\pi k/\lambda$.

A.2.1 Photoresist exposure kinetics

The kinetic of photoresist modification is specifically dependent on light absorption phenomena. Description of absorption may be given in macroscopic or microscopic detail.

On the macroscopic level, absorption is described by Lambert Beer laws, linear relationship between absorbance and the concentration (times the path length) of the absorbing species.

$$\frac{dI}{dz} = -\alpha I$$

where I is the intensity of light in the z direction, and α the absorption coefficient. In homogeneous media $I(z) = I_o \exp(-Abs(z))$. Lambert - Beer validity should be verified over range of interest of concentration, since the real part of absorption coefficient changes partially with concentration.

On microscopic level, absorption process may be thought of as photons causing electrons to be promoted to high energy states, leading eventually to chemical reactions. For the photoactive compound, absorption of UV light leads to chemical conversion of photoactive compound M to product P, through the active state $M*$. For example, the chemistry of diazonaftoquinone which at the base of the positive photoresist AR P 3210 adopted for process leading to microchannels reported in fig.2.3)

$M \xrightarrow{UV} P$ $\qquad\qquad$ $M \underset{k_2}{\overset{k_1}{\rightleftarrows}} M* \xrightarrow{k_3} P$

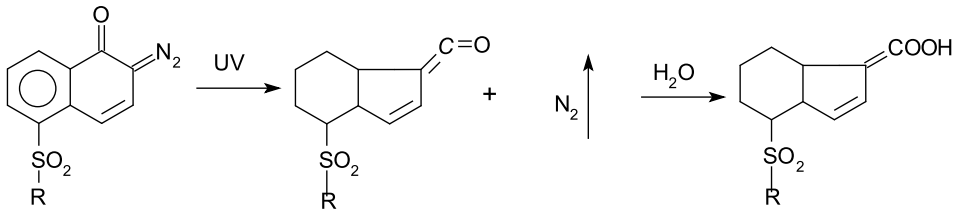

Figure A.3: Mechanism for diazonaftoquinone

First order reaction mechanism apply:

$$dM/dt = k_2 M^* - k_1 M \tag{A.3}$$

$$dM^*/dt = k_1 M - (k_2 + k_3) M^* \tag{A.4}$$

$$dP/dt = k_3 M^* \tag{A.5}$$

Stationary condition ($M^*(t = 0) = 0 = P(t = 0)$; $M(t = 0) = M_0$) imply that M^* transforms into P at the same rate as M undergoes transformation into M^*(i.e. $dM/dt = 0$). Then:

$$dM/dt = -((k_1 k_3)/(k_1 + k_3)) \cdot M \Rightarrow M = M_0 \exp(-Kt) \tag{A.6}$$

Constant K is found experimentally to be proportional to the intensity of the exposure radiation.

The coupled equations of first-order kinetics of the photoactive compound M and the propagation of light through the absorbing media are:

$$\frac{dm}{dt} = CIm \qquad \frac{dI}{dz} = -\alpha I \tag{A.7}$$

The solution of this system consists in obtaining I and m in recursive times steps, up to the

exposure time, assuming intensity constant within the time step.

Acknowledgment

I wish to acknowledge all the staff of the CNR - ISMN NMM Lab for the support and help they have given in these three years. They are a group of very stimulating persons. My research work and curiosity have been amplified by the collaborative work.

I thank all the researchers without whom the accomplishment of this thesis would have been impossible: Dr. Fabio Biscarini, Dr. Massimiliano Cavallini, Dr.ssa Chiara Dionigi, Dr. Francesco Valle, Dr. Francesco Cino Matacotta, Dr.ssa Eva Bystrenova, Dr.ssa Annalisa Calò, Dr. Pablo Stoliar, Dr. Jean Crispin Kengne, Dr. Massimo Facchini, Dr.ssa Silvia Milita.

In particular I am very grateful to two young researchers who have worked in the CNR - ISMN, and now collaborate from France and Belgium laboratories: Dr. Adina Lazar and Dr. Dana Serban. They are very motivated. It has been a pleasure to collaborate with them and share some scientific intuitions.

I wish also to thank a lot:

- my wife Costanza, she has supported all my work with humanity, and given a lot of good twilight advices,
- my family, the suggestions an the incitements on the impact of innovation on society, in particular my sister. I thank a lot my uncle Orlando, and my cousins Natascia and Annapina, for their good humour, also in difficult times.
- all my best friends, Manfredi, Maria Chiara, Michele, Rosanna, Giorgio, Adele, Raffaele, Donatella, Silvio, Enzo, Olga ... for the good time and the thoughtful time spent together

A particular acknowledgment to:

- Fabio Biscarini for providing the financial support, for giving me the opportunity of working in such stimulating, macro, environment. I thank him also for the care full analysis of all the work done in nanoscience.
- Francesco Cino Matacotta for the financial support of the present year, including thesis, and giving me the opportunity to work in Scriba Nanotecnologie srl.
- Prof. Francesco Zerbetto for help and theoretical explanations about molecular dynamics and peptide aggregation.